

PREDICTION OF HEAT TRANSFER AND MICROSTRUCTURE
IN HIGH-PRESSURE DIE-CAST
A383 ALUMINUM ALLOY

by

MIKKO KARKKAINEN

LAURENTIU NASTAC, COMMITTEE CHAIR

LUKE BREWER

RUIGANG WANG

SAMEER MULANI

CHARLES A. MONROE

A DISSERTATION

Submitted in partial fulfillment of the requirements
for the degree of Doctor of Philosophy
in the Department of Metallurgical
and Materials Engineering
in the Graduate School of
The University of Alabama

TUSCALOOSA, ALABAMA

2019

Copyright Mikko Karkkainen 2019
ALL RIGHTS RESERVE

ABSTRACT

Predicting the microstructure of the as-cast HPDC (high-pressure die cast) product is valuable, because micro-scale features often determine its mechanical properties. To predict the microstructure, the effect of processing parameters such as pressure and cooling rates must be known. The object of this study is to create state-of-the-art models for predicting heat transfer in the HPDC process and apply those models to predict the evolution of one feature of the microstructure: the size of polyhedral α -Fe intermetallic phase.

In the study, we develop a new empirical correlation for the Nusselt number in water cooling channels. This can be used to validate heat transfer coefficients for water cooling channels in commercial software to assist in modelling heat transfer in the HPDC process.

Additionally, we develop a model for impact pressure in HPDC, which augments the state-of-the-art Hamasaiid model for peak IHTC (interfacial heat transfer coefficient) in HPDC, and relaxes some of their empirical assumptions. We integrate the IHTC model as a custom boundary condition in FLUENT 18.1 using SCM and UDF-files.

Finally, we predict the size of polyhedral Fe-rich intermetallics using commercial casting simulation NOVAFLOW&SOLID for cooling rates and classical solidification theory for intermetallic size, and validate the results using optical micrograph size measurements.

DEDICATION

This thesis is dedicated to my host family. Thank you, Virpi and Charlie, for giving me so much, and expecting nothing in return. Without you this journey would not have been nearly as enjoyable, let alone possible.

LIST OF ABBREVIATIONS AND SYMBOLS

ρ	Density, kg/m ³
v, u	Velocity, m/s
L_H	Hydrodynamic length, m
D_H	Hydraulic diameter, m
μ	Dynamic viscosity, kg/(m·s)
L_M	Modulus of solidification, m
q_w	Wall heat flux, W/m ²
ΔT	Temperature difference, K
t	Time, s
k	Fluid thermal conductivity, W/(m·K)
c_p	Specific heat
β	Volumetric coefficient of thermal expansion
g	Standard gravity, m ² /s
F_{ann}	Geometric fitting parameter for Gnielinski correlation for annular ducts
f_{ann}	Darcy friction factor for annular ducts
a	Ratio between inner and outer tube diameters

ΔQ	Quantity of heat transferred, J
h	Heat transfer coefficient, W/(m ² ·K)
K	Fitting parameter dependent on bulk and wall Pr-numbers
ΔT_{LMTD}	Logarithmic mean temperature difference, K
r_c	Heat flux tube resistance, (m ² ·K)/W
a_s	Microcontact spot radius, m
b_s	Heat flux tube radius, m
n_s	Area density of microcontact spots, 1/m ²
R_c	Thermal contact resistance between two surfaces, (m ² ·K)/W
λ	Harmonic mean thermal conductivity, W/(m·K)
σ	Mean asperity peak height, m
R_{SM}	Mean asperity peak spacing, m
ϵ	Numeric parameter determined from statistical image analysis for average density of random circles in an area.
Y	Air gap width, m
γ_l	Surface tension, N/m
ϕ	Angle between asperity and mean plain
θ	Contact angle
P_γ	Capillary pressure, Pa
T_0	Temperature at NTP-conditions, K
T_1	Temperature during melt impact on die, K
P_0	Pressure at NTP-conditions, Pa
P_1	Impact pressure of melt on die surface, Pa

ΔP_s	Stagnation pressure, Pa
ΔP_{whp}	Water hammer pressure, Pa
c	Fluid sonic velocity, m/s
E	Bulk modulus of fluid, GPa
c_0	Fitting parameter for air gap growth model
f_s	Solid fraction
C_l	Liquid concentration, wt%
C_0	Initial bulk liquid concentration, wt%
k_p	Solidification partition coefficient
v_α	Diffusion-limited growth velocity of α -Fe intermetallic, m/s
D_L	Liquid diffusivity
Ω_c	Solutal supersaturation
C_l^*	Concentration liquid solid-liquid interface, wt%
C_α^*	Concentration of solid α -Fe intermetallic at solid-liquid interface, wt%
V_L	Volume of liquid in solidification envelope, m ³
N_α	Number of $\alpha - Fe$ nuclei in solidification envelope
erfc	Complementary error function
IHTC	Interfacial heat transfer coefficient, W/(m ² ·K)
ANOVA	Analysis of variance
CFD	Computational fluid dynamics
VOF	Volume of fluid
UDF	User defined function
SCM	Scheme script file

ACKNOWLEDGMENTS

I would like to express my sincere gratitude to all the colleagues, friends, and faculty members who have helped me throughout this research project.

I am grateful for my advisor Dr. Laurentiu Nastac for his patience, guidance, and help in navigating my Ph.D. journey. I would also like to thank my committee members, Dr. Luke Brewer, Dr. Sameer Mulani, Dr. Charles A. Monroe and Dr. Ruigang Wang, for their constructive feedback and patience.

Moreover, I would like to give special thanks to my colleagues Qing Cao, Liping Guo, Yang Xuan, Aqi Dong for their friendship, encouragement and inspiration throughout my Ph.D. study.

CONTENTS

ABSTRACT	ii
DEDICATION	iii
LIST OF ABBREVIATIONS AND SYMBOLS	iv
ACKNOWLEDGMENTS	vii
LIST OF TABLES	xii
LIST OF FIGURES	xiv
CHAPTER 1 – INTRODUCTION	1
1.1 The high-pressure die-casting process	1
1.2 Motivation and goals.....	4
1.3 Physical phenomena.....	7
1.3.1 Reynolds number	10
1.3.2 Prandtl number.....	10
1.3.3 Nusselt number	11
1.3.4 Biot number	11
1.3.5 Richardson number	12

CHAPTER 2 – LITERATURE REVIEW	13
2.1 Effect of process parameters in HPDC	13
2.2 Properties of A383 alloy	16
2.3 Models for interfacial heat transfer coefficient in HPDC	17
2.4 Numerical turbulence models	18
CHAPTER 3 – HEAT TRANSFER MODEL FOR WATER COOLING CHANNELS.....	20
3.1 Introduction.....	20
3.2 FLUENT model description	22
3.3 Parametric study.....	28
3.3.1 Nusselt number	28
3.3.2 Darcy friction factor.....	31
3.4 Bubbler simulations	34
3.5 Conclusions.....	42
CHAPTER 4 – HEAT TRANSFER MODEL FOR THE DIE-CASTING INTERFACE	43
4.1 Introduction.....	43
4.2 Mathematical models	43
4.2.1 Interfacial heat transfer coefficient	43
4.2.2 Air gap thickness.....	47
4.2.4 Capillary pressure	50
4.2.5 Impact pressure	54

4.3 Die-filling simulation.....	55
4.3.1 Goals	55
4.3.2 Mesh independence study	58
4.3.3 Velocity at the gate and rib locations.....	63
4.3.3 Impact pressure and IHTC	66
4.4 Evolution of IHTC with time.....	69
4.5 Conclusions.....	73
CHAPTER 5 – SOLIDIFICATION KINETICS OF FE-RICH INTERMETALLICS	74
5.1 Introduction.....	74
5.2 Mathematical models	77
5.3 Predicting cooling rate in HPDC A383	79
5.4 Methods.....	91
5.4.1 Experimental methods	91
5.4.2 Growth model parameters.....	93
5.5 Results and discussion	94
5.5.1 Samples 1 and 3	94
5.5.2 Sample 4.....	99
5.5.2 Sample 5.....	102
5.6 Conclusions.....	106
CHAPTER 6 – CONCLUSIONS AND FUTURE WORK.....	107

6.1 Conclusions.....	107
6.1.2 Die-casting interfacial heat transfer coefficient.....	107
6.1.3 Kinetics of α -Fe intermetallic growth in HPDC A383.....	108
6.2 Main contributions of this study	109
6.3 Recommendations for future work	109
REFERENCES	111
APPENDIX A.....	118
APPENDIX B	120
APPENDIX C	122
APPENDIX D.....	125
APPENDIX E	126
APPENDIX F.....	129

LIST OF TABLES

Table 1.1 Non-dimensional groups for conduction-convection heat transfer.....	7
Table 1.2 Typical system parameters for HPDC Al-alloys during die-filling.....	8
Table 1.3 Typical system parameters for water cooling channels during operation	9
Table 2.1 A383 melt composition (wt%).....	17
Table 2.2 Composition of polyhedral α -Fe intermetallic in HPDC A383 (“sludge”) (wt%).....	17
Table 2.3 Composition of intergranular α -Fe intermetallic in HPDC A383 (“Chinese script”) (wt%).....	17
Table 3.1 Thermo-physical properties of water [54]	26
Table 3.2 Heat-exchanger simulation parameters.....	26
Table 3.3 Simulation parameters for determination of bubbler F_{ann}	37
Table 3.4 Selected bubbler simulation parameters	38
Table 4.1 Parameter values for capillary pressure study	53
Table 4.2 Material parameters for die-filling simulation.....	56
Table 4.3 Simulation parameters for die-filling simulation.....	56
Table 4.4 IHTC for Al-alloy, present study	67
Table 4.5 IHTC for Mg-alloy, present study	68
Table 4.6 IHTC for Al-alloy, Hamasaiid	68
Table 4.7 IHTC for Mg-alloy, Hamasaiid	68
Table 5.1 FLIR temperature measurements.....	81
Table 5.2 Values of optimization parameters	82

Table 5.3 Input parameters for α -Fe growth model..... 94

LIST OF FIGURES

Figure 1.1 Typical HPDC casting cycle	2
Figure 1.2 Typical shot curve in HPDC.....	2
Figure 1.3 Casting and cooling channel geometry in Nematik Alabama HPDC system.....	4
Figure 1.4 HPDC geometry used in NOVAFLOW&SOLID simulation.	5
Figure 1.5 Strategy for experiments and simulations in the present study	6
Figure 3.1 Cross-section schematic of bubbler cooling channel	21
Figure 3.2 Strategy for cooling channel heat transfer model development	21
Figure 3.3 FLUENT model of 2D axisymmetric double pipe heat exchanger. Color indicates temperature (K).....	24
Figure 3.4 (a-d) Comparison between FLUENT heat-exchanger simulations and (Equation 3-2).	30
Figure 3.5 (a-d) Comparison between FLUENT simulations and (Equation 3-4) for Darcy Friction factor.	33
Figure 3.6 Comparison of geometric parameter F_{ann} for heat-exchangers (Gnielinski, green) and Bubblers (present study, red-blue).....	36
Figure 3.7 (a) G1 geometry flow streamlines. (b) Predicted Nusselt number using new correlation and FLUENT simulation. Reynolds number is $6.3e3$	39
Figure 3.8 (a) G2 geometry flow streamlines. (b) Predicted Nusselt number using new correlation and FLUENT simulation. Reynolds number is $6.7e3$	40
Figure 3.9 (a) G3 geometry flow streamlines. (b) Predicted Nusselt number using new correlation and FLUENT simulation. Reynolds number is $9.3e3$	41
Figure 4.1 Strategy for developing IHTC model	44
Figure 4.2 Surface profile description by Hamasaiid et al. [18].....	46

Figure 4.3 Casting geometry and sensor locations [12].....	48
Figure 4.4 Temperature and pressure evolution in HPDC [12].....	49
Figure 4.5 Comparison of experimental IHTC and model by Hamasaiid when neglecting the effect capillary pressure.....	50
Figure 4.6 Conical air gap model [62].....	51
Figure 4.7 Absolute value of capillary pressure using (Equation 4-10) and values from Table 4.1.....	53
Figure 4.8 FLUENT simulation geometry.....	57
Figure 4.9 Wall y^+ value at $t=0.075$ s for coarse mesh (left), fine mesh (right), and difference between two models (bottom).....	59
Figure 4.10 Melt volume fraction for coarse mesh (left), fine mesh (right) and difference (bottom) at $t=0.09$ s.....	60
Figure 4.11 Melt volume fraction for coarse mesh (left), fine mesh (right) and difference (bottom) at $t=0.12$ s.....	61
Figure 4.12 Melt volume fraction for coarse mesh (left), fine mesh (right) and difference (bottom) at $t=0.14$ s.....	62
Figure 4.13 Velocity vectors for filling, time-step at 0.09 s.....	62
Figure 4.14 Velocity vectors for filling at time-step 0.14 s.....	63
Figure 4.15 Locations for determining velocity profile.....	64
Figure 4.16 Gate velocity profile for Al-9Si-3Cu.....	65
Figure 4.17 Rib velocity profile for Al-9Si-3Cu.....	65
Figure 4.18 IHTC comparison between experiment, Hamasaiid model and present study.....	69
Figure 4.19 Geometry for IHTC evolution simulation. The casting half-thickness mesh is shown in teal and die mesh in grey.....	70
Figure 4.20 Flowchart for time-evolution simulation of IHTC.....	71
Figure 4.21 time evolution of modelled IHTC (red) vs experiment (blue) for Mg-alloy.....	72
Figure 4.22 time evolution of modelled IHTC (red) vs experiment (blue) for Al-alloy.....	72

Figure 5.1 Polyhedral α -Fe intermetallic (“sludge”) [36]	75
Figure 5.2 Strategy for α -Fe intermetallic growth study.	76
Figure 5.3 Comparison between statistical distribution of cross-sections of diameters for spheres and rhombic dodecahedrons.	79
Figure 5.4 FLIR temperature measurement of Die-surface after casting	80
Figure 5.5 Relative effect of varying fitting parameters to temperatures at locations 1-6 before water spray.	83
Figure 5.6 Relative effect of varying fitting parameters to temperatures at locations 1-6 after water spray.	83
Figure 5.7 Trial 9 temperature evolution at location 1 compared with experimental measurements.	85
Figure 5.8 Trial 9 temperature evolution at location 2 compared with experimental measurements.	86
Figure 5.9 Trial 9 temperature evolution at location 3 compared with experimental measurements.	87
Figure 5.10 Trial 9 temperature evolution at location 4 compared with experimental measurements.	88
Figure 5.11 Trial 9 temperature evolution at location 5 compared with experimental measurements.	89
Figure 5.12 Trial 9 temperature evolution at location 6 compared with experimental measurements.	90
Figure 5.13 Location of samples for sludge size measurements	91
Figure 5.14 Optical micrograph taken from sample 1.	92
Figure 5.15 Optical micrograph taken from sample 5.	93
Figure 5.16 NOVAFLOW&SOLID simulation of Samples 1,3.	95
Figure 5.17 Measured α -Fe diameter distribution and Saltykov-method estimate for 3D diameter distribution for sample 1.	96
Figure 5.18 Measured α -Fe diameter distribution and Saltykov-method estimate for 3D diameter distribution for sample 3.	97

Figure 5.19 α -Fe growth model predicted diameter at samples 1,3	98
Figure 5.20 NOVAFLOW&SOLID simulation of Sample 4	99
Figure 5.21 Measured α -Fe diameter distribution and Saltykov-method estimate for 3D diameter distribution for sample 4.....	100
Figure 5.22 α -Fe growth model predicted diameter at sample 4.....	101
Figure 5.23 NOVAFLOW&SOLID simulation of Sample 5	103
Figure 5.24 Measured α -Fe diameter distribution and Saltykov-method estimate for 3D diameter distribution for sample 5.....	104
Figure 5.25 α -Fe growth model predicted diameter at sample 5.....	105

CHAPTER 1 – INTRODUCTION

1.1 The high-pressure die-casting process

High-Pressure Die-Casting (HPDC) is a casting method that is primarily used for light-weight magnesium and aluminum-based alloys. It is especially popular in the automotive industry for the casting of non-ferrous parts like cylinder heads and engine blocks. The advantages of the process are the low cycle time, high cooling rates, good surface quality, complex near-net shape with tight tolerances, and ability to cast thin-walled structures. [1] [2] [3] In 2015, it was estimated that 60% of all light-weight alloy metal castings in the automotive industry were made using HPDC. [4]

The process of injection and removal of the casting is carried out in cycles. Typically, over 10 casting cycles are carried out in rapid succession. The first 3-4 cycles of a run are not intended for production. Instead, they are used to heat the die to a desired stable temperature. The castings from these initial cycles are recycled into raw material. A typical casting cycle is pictured in Figure 1.1. The cycle starts with the plunger injecting the alloy into the die. A vacuum might be applied to the die cavity to reduce air entrapment. Once the part is solidified, the die is opened and the part is removed. A water/air spray is used to cool the inner die surface. Finally, the die is closed in preparation for a new cycle

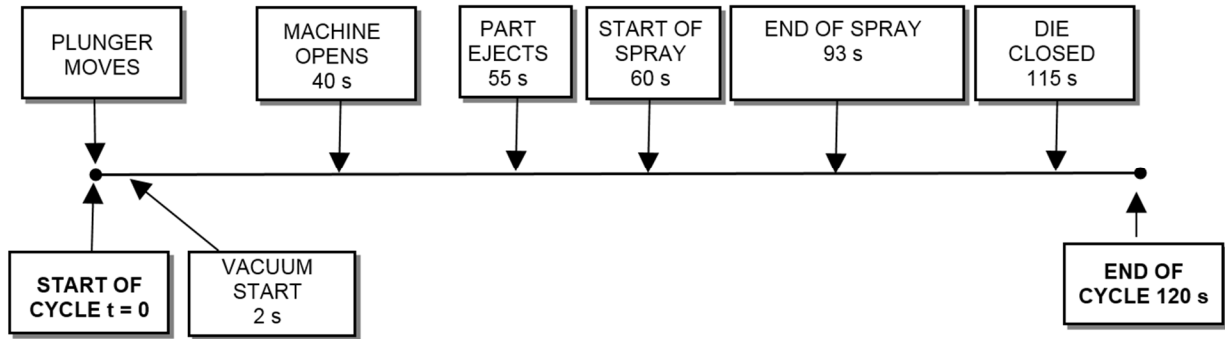


Figure 1.1 Typical HPDC casting cycle

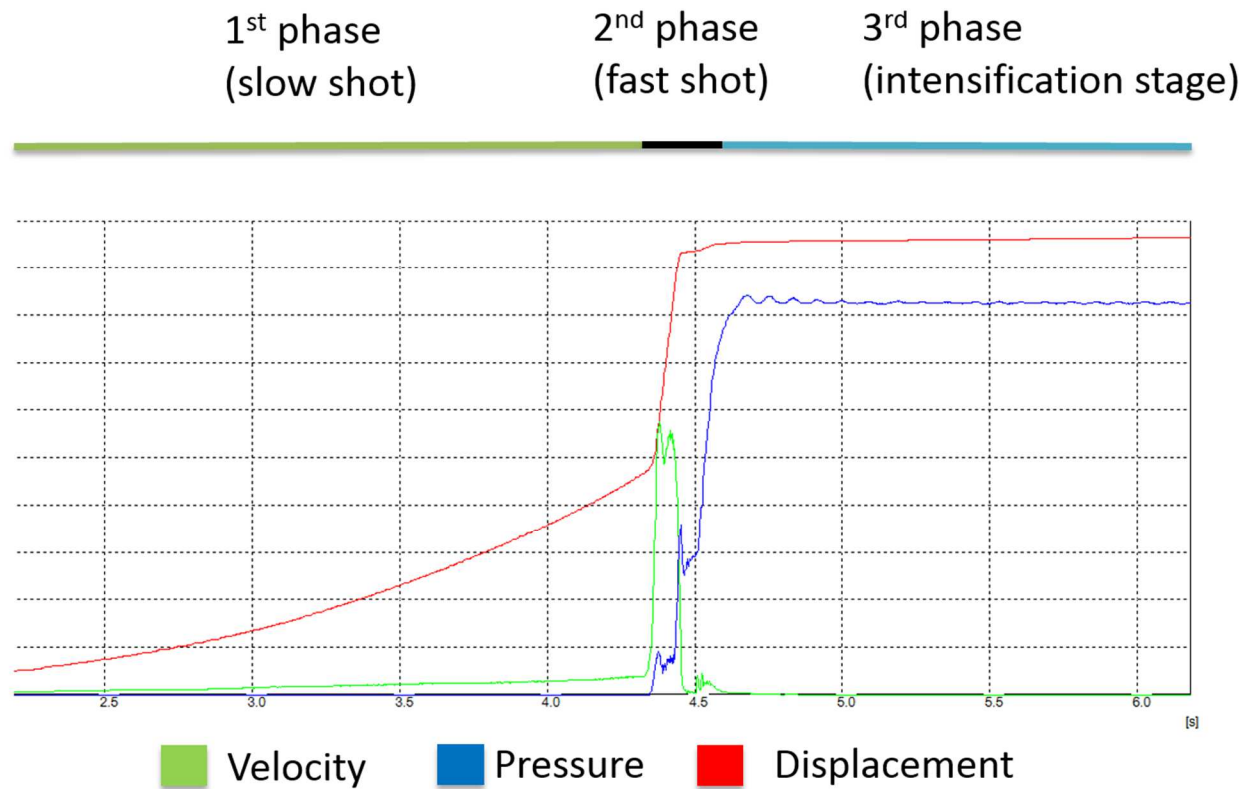


Figure 1.2 Typical shot curve in HPDC

In HPDC, the metal is poured into a shot sleeve prior to injection into the die. Injection takes place by a hydraulic piston, which pushes the metal into the die cavity through a gating system. A sample shot curve depicting the movement of the piston is shown in Figure 1.2.

Initially, the piston moves slow until the metal fills the entire shot sleeve volume. This is called the 1st phase or slow shot. Next, the metal is rapidly injected into the die in the 2nd phase or fast shot. Finally, an intensification pressure is applied in the 3rd phase or intensification stage until the end of solidification.

The die itself consists of two parts, a fixed half and a moving half. The moving half is separated from the fixed half to remove the solidified casting. In addition to water sprays, the die is continuously cooled by “cooling channels”, water cooled copper tubes installed into the die. Figure 1.3 shows the geometry of the engine block casting and the location of cooling channels inside the die for the HPDC machine at Nematik Alabama. Figure 1.4 shows the casting geometry used for solidification simulation in the commercial casting simulation software NOVAFLOW&SOLID.

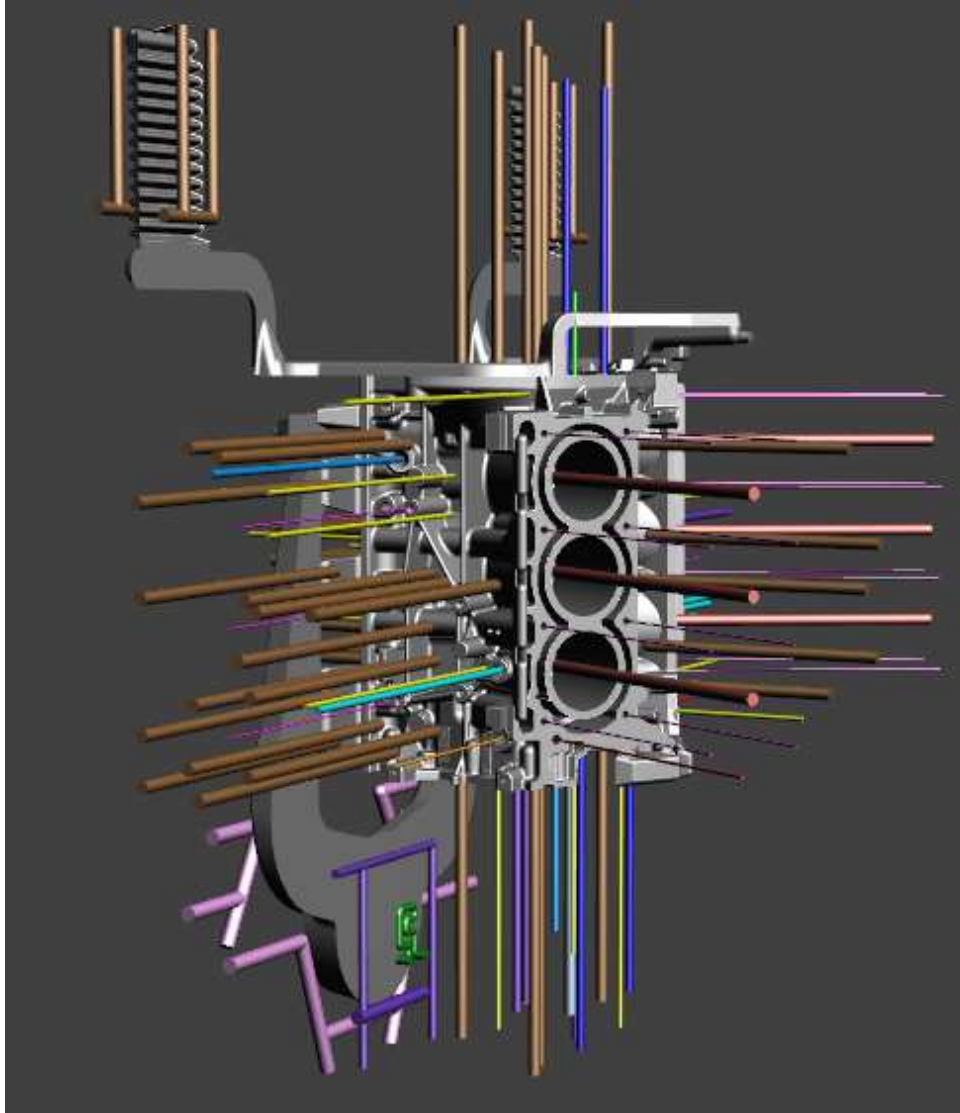


Figure 1.3 Casting and cooling channel geometry in Nemak Alabama HPDC system.

1.2 Motivation and goals

Predicting the microstructure of the as-cast product is valuable, because micro-scale features often determine the mechanism of mechanical failure. The primary phase grain-size affects the strength and ductility of the product through grain-boundary strengthening. [5] Secondary phase precipitates increase yield strength by impeding dislocation motion, but

simultaneously reduce ductility by acting as stress concentrators for crack nucleation. Micro-porosity reduces the load-bearing area of the casting, and therefore facilitates crack propagation.

[6] [7] [8]

The purpose of this study is to determine a causal link between macroscopic processing parameters and the microstructure in high-pressure die-cast A383 alloy using simulations and experimental data. More specifically, we develop heat transfer models for water cooling channels (Chapter 3) and the die-casting interface (Chapter 4). We use predicted cooling rates to model the size distribution of the polyhedral Fe-rich intermetallic phase in the A383 casting (Chapter 5).

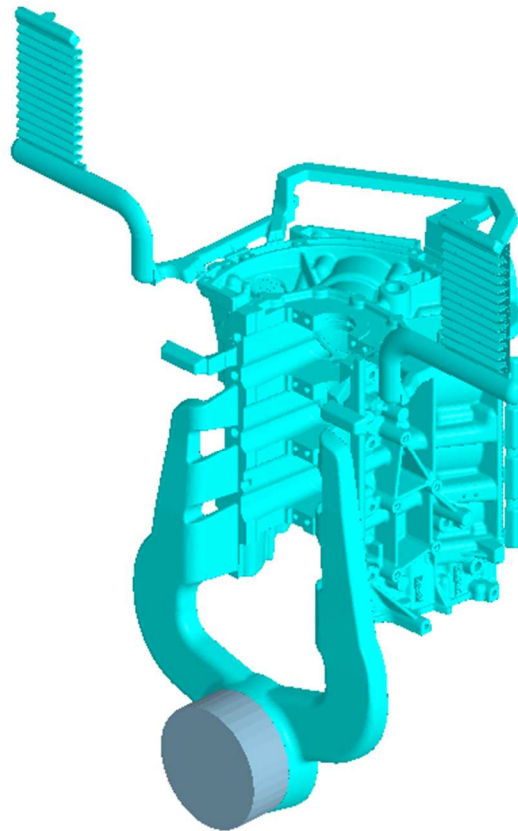


Figure 1.4 HPDC geometry used in NOVAFLOW&SOLID simulation.

Many physical phenomena need to be addressed: turbulent fluid flow, convective and conductive heat transfer and solidification. The importance of accurate models for heat transfer and microstructure evolution in HPDC is not just academic. Heat transfer is notoriously hard to measure in HPDC. When designing HPDC systems for new geometries, no such measurements are available, and engineers have to determine the locations and flow rates for water cooling channels and water sprays through trial and error. Accurate heat transfer models can facilitate this process. The strategy for the present study is visualized in Figure 1.5.

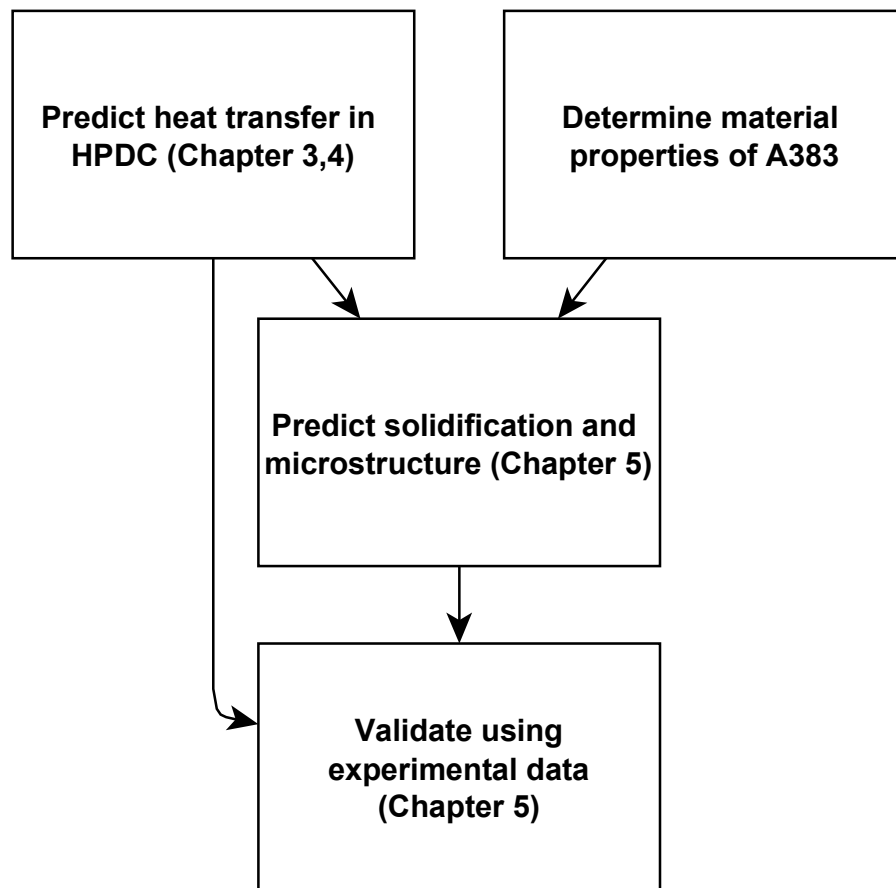


Figure 1.5 Strategy for experiments and simulations in the present study

1.3 Physical phenomena

Before any model of the HPDC process can be constructed, it is important to identify the relevant physical phenomena, and estimate their relative importance. A common and valid strategy is to use dimensional analysis: identify the physical parameters affecting the quantities we wish to predict, and construct non-dimensional groups from these parameters to facilitate analysis. [9] Table 1.1 depicts the system parameters and derived non-dimensional groups relevant for conduction-convection heat transfer in castings.

Table 1.1 Non-dimensional groups for conduction-convection heat transfer

System parameters	Non-dimensional groups
u_m (mean velocity)	$Re = \frac{\rho u_m L_H}{\mu}$
L_H (hydrodynamic length)	$Pr = \frac{\mu c_p}{k}$
L_M (modulus of solidification)	$Nu = \frac{q_w L_H}{k \Delta T}$
ρ (density)	$Bi = \frac{q_w L_M}{k \Delta T}$
μ (dynamic viscosity)	$Ri = \frac{\rho g \beta \Delta T L_H}{u_m^2}$
q_w (wall heat flux)	
ΔT (temperature difference)	
k (fluid thermal conductivity)	
c_p (specific heat)	
β (volumetric coefficient of thermal expansion)	

Table 1.2 depicts typical system parameter values for a HPDC Aluminum alloy during fast shot. Table 1.3 depicts typical system parameter values for water cooling channels. We examine the validity of the assumptions made in our models with the help of these dimensionless numbers. In this chapter, we will go through the various dimensionless numbers using the system parameter values in Table 1.2 and Table 1.3, and explain their significance.

Table 1.2 Typical system parameters for HPDC Al-alloys during die-filling

System parameters	Value
u_m (mean velocity)	3 m/s
L_H (hydrodynamic length)	5e-3 m
L_M (modulus of solidification)	2.5e-3 m
ρ_M (density)	2800 kg/m ³
μ (dynamic viscosity)	0.001 Pa s
q_w (wall heat flux)	10e6 W/m ²
ΔT (temperature difference)	420 K
k (fluid thermal conductivity)	100 W/(K m)
c_p (specific heat)	1050 J/(kg K)
β (volumetric coefficient of thermal expansion)	1.03e-4 1/K

Table 1.3 Typical system parameters for water cooling channels during operation

System parameters	Value
u_m (mean velocity)	5 m/s
L_H (hydrodynamic length)	2e-3 m
L_M (modulus of solidification)	-
ρ (density)	998 kg/m ³
μ (dynamic viscosity)	0.001 Pa s
q_w (wall heat flux)	1e6 W/m ²
ΔT (temperature difference)	50 K
k (fluid thermal conductivity)	0.6 W/(K m)
c_p (specific heat)	4182 J/(kg K)
β (volumetric coefficient of thermal expansion)	2.04e-4 1/K

1.3.1 Reynolds number

Reynolds number is usually described by the relation:

$$\text{Re} = \frac{\rho u_m L_H}{\mu} = \frac{\text{Inertial forces}}{\text{Viscous forces}} \quad (\text{Equation 1-1})$$

Experimental observations show that laminar flow occurs when $\text{Re} < 2300$ and fully turbulent flow occurs, when $\text{Re} > 2900$. [9] For the case of die-filling of al-alloy, the Reynolds number estimated from values in Table 1.2 becomes 42000, well into the turbulent regime. For the water cooling channels, the estimated Reynolds number is 25000, making the flow likewise fully turbulent. Therefore we need to account for turbulent flow in both the die-filling and water cooling channel model.

1.3.2 Prandtl number

The Prandtl number is a material property, which describes the ratio between momentum diffusivity and thermal diffusivity in the material:

$$\text{Pr} = \frac{\mu c_p}{k} = \frac{\text{momentum diffusivity}}{\text{thermal diffusivity}} \quad (\text{Equation 1-2})$$

For a high Pr-number material, flow velocity close to the boundary is strong compared to heat transfer in the boundary layer. Therefore convection is relatively more important than conduction in a high Pr-number material, and vice versa for a low Pr-number material. For an

Al-alloy, the Prandtl number is 0.01. For water, the Pr-number is 6.97. Therefore, for Al-alloys, the role of convection is significantly weaker than conduction in comparison to water.

1.3.3 Nusselt number

The Nusselt number is a property describing heat transfer for a fluid flowing along a boundary. It is given by:

$$\text{Nu} = \frac{q_w L_H}{k \Delta T} = \frac{\text{Convective heat transfer}}{\text{Conductive heat transfer}} \quad (\text{Equation 1-3})$$

The Nusselt number can be understood as a dimensionless heat transfer coefficient. It is used to describe heat transfer between a solid and a fluid independent of length scale and material properties. [10] For the die-filling process, Nu is approximately 1, which implies that conduction and convection are equally significant. It should be noted, however, that the die-filling only lasts for 0.1 seconds in the HPDC process, after which fluid flow is minimal. For water cooling channels, Nu is approximately 60, so convective cooling is dominant.

1.3.4 Biot number

The biot-number is the ratio of heat transfer over a boundary and heat transfer inside a body:

$$\text{Bi} = \frac{q_w L_M}{k \Delta T} = \frac{\text{Boundary heat transfer}}{\text{Internal heat transfer}} \quad (\text{Equation 1-4})$$

A low Biot number <0.1 implies that thermal gradients inside the body can be ignored, i.e. the whole domain can be considered to be at an equal temperature. For the HPDC process, the Biot number is 0.6. For the water cooling channel, the Biot number is 4000. For both cases, we need to consider thermal gradients in the fluid domain.

1.3.5 Richardson number

The Richardson number gives the significance of natural convection, i.e. buoyancy induced flow, compared to forced convection:

$$Ri = \frac{\rho g \beta \Delta T L_H}{u_m^2} \quad (\text{Equation 1-5})$$

For a Richardson number below 0.1, buoyancy effects can be ignored. [11] For the die-filling process, the Richardson number is 0.6. For the water cooling channels, the Richardson number is $8e-3$. For the die-filling process, the effect of buoyancy on fluid flow is low. For the water cooling channel, it is negligible

CHAPTER 2 – LITERATURE REVIEW

2.1 Effect of process parameters in HPDC

The pressure in the HPDC is provided by a hydraulic piston. The filling process can be divided into three parts. During the slow shot phase (first stage), the piston slowly moves until the metal occupies the whole shot sleeve volume. After this, the fast shot phase (second stage) begins, and the metal is rapidly injected into the die. Finally, an intensification pressure (IP) is applied to maintain a high pressure in the casting.

Second stage velocity has been universally found to have a large effect on IHTC (interfacial heat transfer coefficient). [12] [13] [14] [15] [13] [16] [12] The second stage velocity affects the impact pressure of the metal jet on the die. The impact pressure has been hypothesized to determine the quality of thermal contact between the die and the casting. [17] [18]

The effect of initial die temperature is also significant. Several studies have found a strong [13] [14] or even dominant [19] inverse correlation between die temperature and peak IHTC. The nature of this effect is unclear, but it might be due to the effect of the die surface temperature on the surface tension of the cast metal. [13]

Intensification pressure has been found to have a very low effect on heat transfer in the pressure range commonly used in HPDC (30-80 MPa). [16] [12] [20] A study conducted with lower pressure (<100 kPa) showed that IHTC increases with pressure up to 80 kPa, after which the effect was small. [21] Some researchers have found that pressure has a significant effect on porosity [2, 22] and mechanical properties [22] of HPDC Al-Si-alloys. High pressure reduces solidification shrinkage induced porosity. [14] [22] However, after the liquid feeding is cut off by solidification, the IP will no longer have an effect, and shrinkage porosity can form. [2] [23] This is especially problematic if the gating system for the casting is thin. After the gates solidify, no pressure is applied to the remaining liquid in the casting, and shrinkage cavities cannot be filled by fluid flow. On the other hand, thick gates can cause shear-band induced cracking. [2]

Casting thickness has been found to be inversely proportional to peak IHTC. [24] [14] [19] In sections with high thickness, IHTC decreases slower as a function of time. [14] [19] The increased peak IHTC in thin cross-sections is likely due to increased filling velocity. The slower decrease in thick cross-sections is likely due to slower solidification in higher thickness.

The only studies to address the effect of the die surface roughness in HPDC to date have been conducted by Hamasaiid et al. [25] [18] They managed to create a surface roughness profile description that adequately matches the measured contact area of the die and alloy. They used 2 measured roughness parameters in their profile description: the mean peak height deviation σ and the mean peak spacing R_{sm} . In their mathematical model, the value of peak spacing has an especially strong effect on IHTC.

The most recent development in the field of HPDC is the introduction of a new process called rheo-HPDC, where the metal is injected into the die as a semi-solid slurry. The advantages are in reduced solidification shrinkage and fully laminar filling, as opposed to the high-speed turbulent filling in traditional HPDC. These changes have resulted in a significant decrease in porosity and size of Fe-rich intermetallics [26], resulting in improved mechanical properties [27] [26] This suggests that solidification shrinkage and possibly air entrapment due to the turbulent flow are the main causes for porosity in the HPDC process.

The effects of pressure and temperature on the phase diagram of A383 can be estimated using the CALPHAD (calculated phase diagram) method, where the free energies of different phases are calculated using known EOS (equations of state). [28] Calculations for binary Al-Si phase diagrams using the ThermoCalc software have shown that the effect of 100, 200 and 300 MPa pressure on the solidus-temperature is approximately 3, 5 and 8 °C respectively [29]. The changes to the liquidus-temperature are the same order of magnitude. These changes have a negligible effect on the undercooling that acts as the driving force for nucleation and growth during the solidification of the alloy.

Pressure also has a minor effect on the eutectic composition of the alloy. Since eutectic Si, contrary to Al, has a higher molar volume than the liquid alloy, its formation is inhibited at high pressures. For a pressure of 100 MPa, this phenomenon changes the eutectic composition of binary Al-Si from 0.121 mole fraction silicon to 0.125 mole fraction silicon. [29] This effect is also small enough to ignore in the HPDC model.

2.2 Properties of A383 alloy

The material we are modeling is A383 aluminum, which is a hypoeutectic Al-Si-Cu alloy designed specifically for HPDC. Iron, which is typically an impurity in Al-alloys, is added to avoid die-soldering. [30, 31] The advantages of Al-Si alloys are light weight and satisfactory ductility [32], high thermal conductivity [33], corrosion-resistance [34], and wear-resistance [35]. The melt composition of A383 is shown in Table 2.1.

Casting HPDC A383 also comes with some challenges. Like in other Al-Si alloys, eutectic Silicon may adopt a brittle acicular (needle-like) morphology prone to fracture. [7] The silicon particles are faceted, and usually nucleate on impurities like AlP. Additives such as Sr or Na can be used to modify the Si-growth mechanism to make it more isotropic. Higher cooling rates can also result in more circular and fine Si-particles. [36]

Another challenge in A383 is the formation of brittle iron-rich intermetallic precipitates. [37] These can be classified into two categories based on formation temperature. The Fe-rich intermetallic phase formed above the alloy liquidus-temperature is called sludge. [38] It has the nominal composition of $Al_{15}(Fe,Mn,Cr)_3Si_2$ [39] or $Al_{12}(Fe,Mn,Cr)_3Si_2$. [40] Below the liquidus-temperature, Fe-rich intermetallics are formed with the nominal composition of $Al_{15}(Fe,Mn)_3Si_2$ or $Al_{15}(Fe,Mn,Cr)_3Si_2$. [38] [41] This phase has the nickname “Chinese script” due to its intricate shape along grain boundaries. The composition of these two morphologies has been measured in A383 engine block castings using EDS in the soon-to-be published work by Tao Liu. The measured composition of sludge α -Fe intermetallic is given in Table 2.2. The measured composition of Chinese script α -Fe intermetallic is given in Table 2.3.

Table 2.1 A383 melt composition (wt%)

Al	Si	Cu	Zn	Mn	Ni	Sn	Mg	Fe
Balance	10.5	2.5	1.5	0.5	0.3	0.15	0.1	1.0

Table 2.2 Composition of polyhedral α -Fe intermetallic in HPDC A383 (“sludge”) (wt%)

Al	Si	Cu	Mn	Cr	Fe
Balance	9.3	1.0	7.9	2.5	19.0

Table 2.3 Composition of intergranular α -Fe intermetallic in HPDC A383

(“Chinese script”) (wt%)

Al	Si	Cu	Mn	Cr	Fe
Balance	7.7	9.2	1.7	0.1	18.9

2.3 Models for interfacial heat transfer coefficient in HPDC

While there are several factors (water cooling channels, water sprays) that influence heat transfer in HPDC, the interfacial heat transfer between the casting and die has been found to be dominant. [42]

The most widely-used method to determine the interfacial heat transfer coefficient (IHTC) is the so-called inverse heat conduction method. [43] This method uses temperature measurements (via thermocouples or IR) to determine the temperature at specific points, and uses a heat transfer model to deduce the heat flow between the die and the casting. In practice, this is an iterative model where several parameters of the heat transfer model are modified extensively until parity with measurements is reached. [44] This method is ubiquitously used in academia and industry for modelling the high-pressure die-casting process. [3] [14] [42] [44]

[15] [45] [46] [47] However, installing thermocouples into the steel die is challenging, requiring drilling multiple inserts into the die very close to the die-casting interface. The considerations necessary for successfully measuring IHTC in HPDC are best summarized in [13].

Some researchers have found the IHTC to depend primarily on initial die temperature. [13] [14] [19]. This has prompted the development of an empirical model for the peak IHTC as a function of initial die temperature and several fitting constants. [19] These findings are summarized in [48].

The most fundamental model for HPDC IHTC has been developed by Hamasaiid et al. [25] [18]. Their modeling approach is based on heat transfer over a rough contact surface. The effect of surface roughness is often neglected in experimental work on heat transfer. There are few studies that acknowledge this effect: Xue et al. modeled heat transfer in molten metal droplet impact on a rough steel substrate [49]. Yuan et al. modeled the effect of surface roughness on heat transfer in thermal interface materials (TIM). [50]. Somé et al. modeled the effect of surface roughness and surface chemistry on heat transfer in bitumen. [51] In the chapter 4 we examine the Hamasaiid model in detail.

2.4 Numerical turbulence models

In turbulent flows, the near-wall flow is usually divided into three zones. Starting from closest to the wall to the farthest these are: the viscous sublayer, the buffer zone and log-law layer. [52]

The distance from the wall to is usually measured using the dimensionless distance y^+ . Usually, the viscous sublayer is stated to correspond to the values $y^+ < 5$, the buffer layer to $5 < y^+ < 30$, and the log-law layer to $30 < y^+ < 300$. When building a mesh for numerical turbulence models, the wall y^+ value, the dimensionless distance to the near-wall calculation

cell, has great importance. However, it usually cannot be determined before running the simulation itself.

To accurately resolve the fluid flow in the viscous sublayer, a wall y^+ value of 1 or less is recommended. This is a requirement for the $k - \omega$ turbulence model and highly recommended for the $k - \omega SST$ model. [53] However, trying to satisfy this condition often overwhelms the physical memory and CPU power limitations available to the researcher. When a wall y^+ value of 1 is not feasible, wall functions may be used.

The $k - \epsilon$ turbulence model does not attempt to resolve the flow in the viscous sublayer directly. Instead, it uses empirical wall functions to match near-wall behavior to experiments. [52] The wall functions work best if the near-wall cell is in the log-law layer, $30 < y^+ < 300$. If the mesh resolution is too fine or too large, as in $y^+ < 11.5$ or $y^+ > 300$ [54], the $k - \epsilon$ model introduces large errors.

The buffer layer is a challenge for numerical turbulence models. Neither the $k - \omega$ model or the $k - \epsilon$ model work well in this regime. However, a hybrid model named $k - \omega SST$ has been developed, which linearly interpolates between the $k - \omega$ model and $k - \epsilon$ models when wall y^+ is in the buffer zone. [54] Practical experience has shown that that $k - \omega$ and $k - \omega SST$ are better modelling flow separation and adverse pressure gradients than the $k - \epsilon$, whereas the advantage of $k - \epsilon$ is better computational stability and faster calculation times. [52]

CHAPTER 3 – HEAT TRANSFER MODEL FOR WATER COOLING CHANNELS

3.1 Introduction

Simulating an industrial high pressure die casting (“HPDC”) process requires accurate modelling of heat extraction. The most significant sources of uncertainty in modelling heat transfer in HPDC are 1) the evolution of the heat transfer coefficient (HTC) between the casting and the die wall during solidification, 2) the HTC of water cooling channels. [42] The presence of up to 100 individual channels in the HPDC processed components makes a physical model of each individual cooling channel computationally prohibitive. Thus, developing an empirical expression for the HTC is highly desirable.

Recently, Gnielinski has had success in creating empirical relations for heat transfer in pipes and double-pipe heat exchangers over a wide range of Reynolds and Prandtl numbers. [55] The Gnielinski equation, based on an analytical solution by Petukhov [56], has been extensively validated. [55] Recently, it has been successfully extended to heat transfer in annular ducts. [57]

However, so far, the application of the Gnielinski correlation has been limited to only two geometries: pipe flow and annular ducts with one-sided heat transfer. Simulations offer the possibility of investigating its applicability to the straight portion of the “bubbler” geometry, shown in Figure 1. Bubbler cooling channels consist of a tubular inlet, a tip and an annular outlet. They are typically used in HPDC process to provide localized cooling as close to the casting as possible, since puncturing the die is not an option.

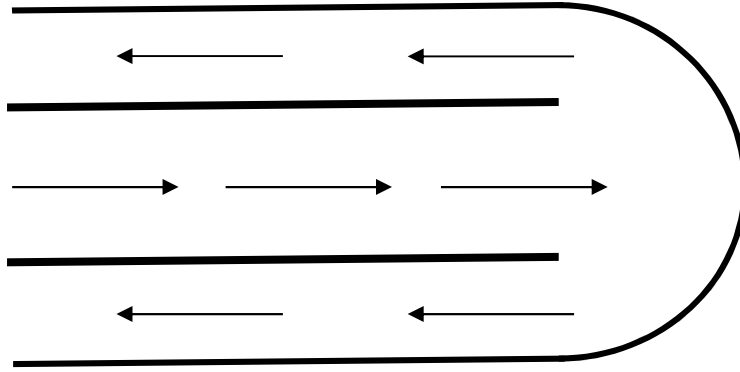


Figure 3.1 Cross-section schematic of bubbler cooling channel

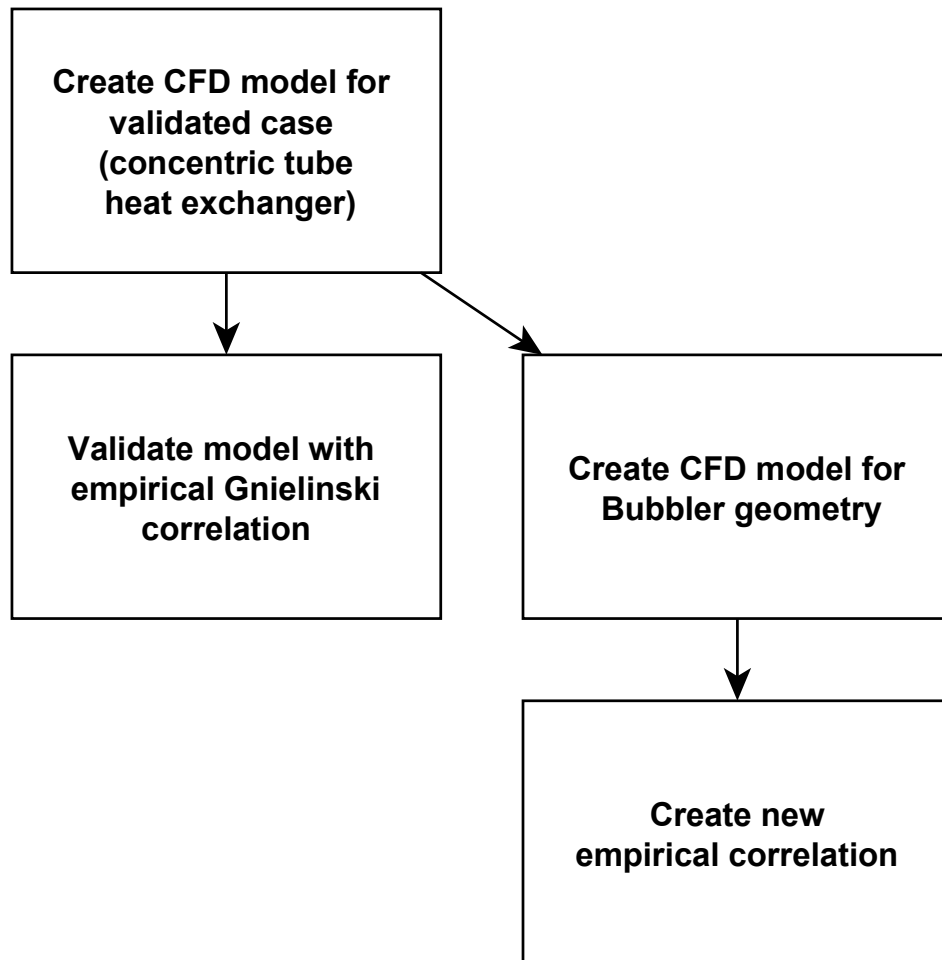


Figure 3.2 Strategy for cooling channel heat transfer model development

ANSYS FLUENT 17.1 was used to make an axisymmetric 2D model with k- ω turbulence model. k- ω model was chosen for its ability to accurately predict near-wall phenomena and flow separation as long as the near-wall mesh resolution is fine. [53]

Simulations were carried out on a quadratic mesh with edge sizing varying from 7e-5 m to 4e-5 m to establish mesh independence. Two different cooling channel types were investigated. A double-pipe heat exchanger was simulated to ensure that the simulation parameters used give matching results with the Gnielinski equation. Then these parameters were applied to modelling the bubbler geometry. The simulation strategy is shown in figure 3.2.

3.2 FLUENT model description

The aim of the model is to accurately predict heat transfer in long narrow horizontal smooth concentric tubes. The Reynolds number range of interest is between 4000 and 100000. The model assumes constant material properties and fully developed single-phase flow, and ignores natural convection. Figure 3.3 shows a cross-section of the top half of the inner and outer tube. The arrows indicate the direction of flow, and the colors indicate temperature (K). Heat transfer at the thin wall separating the two flows is 2-way coupled on both sides. The outer wall is insulated.

The material and geometric parameters for the simulations are given in Table 3.1 and Table 3.2. The k- ω model has good accuracy for near-wall phenomena as long the mesh resolution satisfies $y^+ \leq 1$. [53] As can be seen from Table 3.2, this criterion is satisfied. [53] Turbulent flow can be considered fully developed when the length of geometry is 15 times the hydraulic diameter. Our geometry satisfies this criterion. Thus, any turbulence effects of the inlet may be ignored.

The material properties for water are constant default values used in FLUENT. Other researchers have found that the temperature dependence of the Prandtl number of the flow does have a significant effect on the Nusselt number [11] [58], which may cause some error in our model. This effect should be more pronounced in tubes with large diameter, where the temperature difference between the wall and bulk flow is large. Likewise, a larger temperature difference can be expected for high Reynolds number flows, where the bulk flow has less time to heat up.

The last major potential source of inaccuracy in our model is natural convection. To estimate the significance of natural convection in our case, the dimensionless Richardson number can be used:

$$Ri = \frac{\rho g \beta \Delta T D_H}{u_m^2} \quad (\text{Equation 3-1})$$

where g is acceleration due to gravity, ρ is density, β is the volumetric expansion coefficient, D_H is the hydraulic diameter, ΔT is the temperature difference between the wall and the fluid bulk, and u_m is the mean velocity.

According to [11], a Richardson number of 0.1 or below should correspond to purely forced convection. For the largest annulus in our investigation, we obtain a Richardson number of 3.5e-3, which justifies ignoring natural convection.

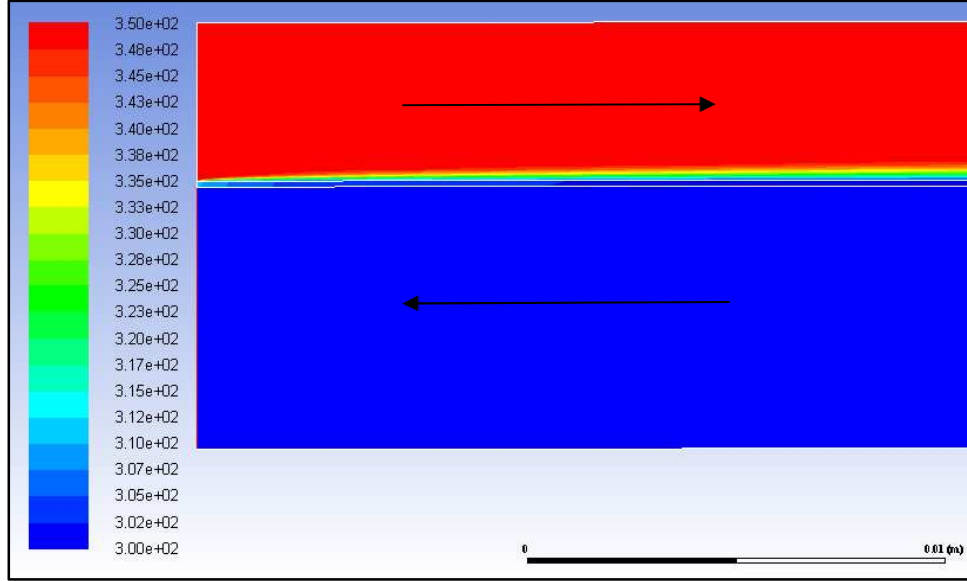


Figure 3.3 FLUENT model of 2D axisymmetric double pipe heat exchanger. Color indicates temperature (K).

For turbulent flow in annuli, Gnielinski gives the following equation for the Nusselt number in the range $Re > 4000$ [57]:

$$Nu = \frac{\frac{f_{ann}}{8} (Re - 1000) Pr}{1 + 12.7 \sqrt{\frac{f_{ann}}{8}} (Pr^{\frac{2}{3}} - 1)} \left(1 + \left(\frac{D_h}{L} \right)^{\frac{2}{3}} \right) F_{ann} \cdot K \quad (\text{Equation 3-2})$$

where F_{ann} is a scaling factor dependent on the heat transfer boundary condition. For the boundary condition of “heat transfer at the inner wall with the outer wall insulated” [57], F_{ann} is given by

$$F_{ann} = 0.75 a^{-0.17} \quad (\text{Equation 3-3})$$

f_{ann} is the friction factor for flow in annular tubes, given by

$$f_{ann} = (1.8 \log_{10} Re^* - 1.5)^{-2} \quad (\text{Equation 3-4})$$

where

$$Re^* = Re \frac{((1 + a^2) \ln a + (1 - a^2))}{(1 - a)^2 \ln a} \quad (\text{Equation 3-5})$$

a is the ratio between the internal pipe and outer annulus diameter:

$$a = \frac{D_1}{D_0} \quad (\text{Equation 3-6})$$

K is a parameter to take into account the temperature dependence of material properties:

$$K = \left(\frac{Pr_b}{Pr_w} \right)^n \quad (\text{Equation 3-7})$$

where Pr_b and Pr_w are the Prandtl numbers at the bulk and wall of the flow respectively. For the FLUENT model, material properties are considered constant, so $K=1$.

The current simulations assume constant material properties and ignore natural convection. This simplification is justifiably for narrow ducts and small temperature gradients were the relative influence of natural convection and temperature dependence of material

properties is minimal. The material and geometric parameters for the simulations are given in Table 3.1 and Table 3.2.

Table 3.1 Thermo-physical properties of water [54]

Heat conductivity, W/mK	Specific heat, J/KgK	Density, kg/m ³	Dynamic viscosity, kg/ms	Prandtl number
0.6	4182	998	1.003e-3	6.99

Table 3.2 Heat-exchanger simulation parameters

Geometry	Inner tube diameter, m	Outer annulus diameter, m	Length, m	y^+	Cool water temperature K	Hot water temperature, K	Inlet turbulence intensity
C1	2.09e-3	2.95e-3	0.1	0.07	300	350	0.6%
C2	3.9e-3	5.62e-3	0.1	0.019	300	350	0.6%
C3	1.27e-2	2.02e-2	0.5	0.018	300	350	0.6%
C4	6.49e-3	2.09e-2	0.5	0.019	300	350	0.6%

The Nusselt number was calculated from the simulation results using the mean logarithmic temperature difference [11] and heat flux from the annulus:

$$h = \frac{\Delta Q}{A_{ann} \cdot \Delta T_{LMTD}} \quad (\text{Equation 3-8})$$

where ΔQ is the heat extracted from the annular flow:

$$\Delta Q = Q_{ann,in} - Q_{ann,out} \quad (\text{Equation 3-9})$$

and h is the heat transfer coefficient:

$$h = \frac{\Delta Q}{A_{ann} \cdot \Delta T_{LMTD}} \quad (\text{Equation 3-10})$$

where ΔT_{LMTD} is the mean logarithmic temperature difference:

$$\Delta T_{LMTD} = \frac{(T_{out,pipe} - T_{in,ann}) - (T_{in,pipe} - T_{out,ann})}{\ln \left(\frac{T_{out,pipe} - T_{in,ann}}{T_{in,pipe} - T_{out,ann}} \right)} \quad (\text{Equation 3-11})$$

Finally, the Nusselt number was calculated from

$$Nu = \frac{hD_H}{k} \quad (\text{Equation 3-12})$$

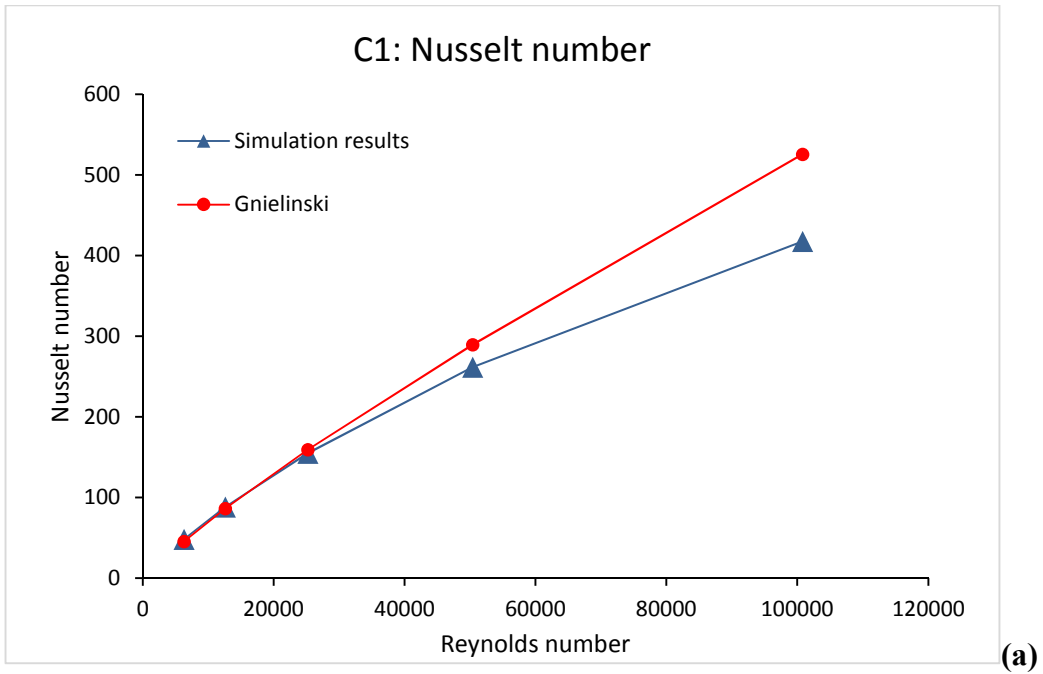
where D_H is the hydraulic diameter of the annulus, and k is the heat conductivity. The friction factor was calculated from the Darcy-Weisbach equation [59]:

$$\frac{\Delta P}{L} = f_{ann} \frac{\rho V_{ann}^2}{2 D_H} \quad (\text{Equation 3-13})$$

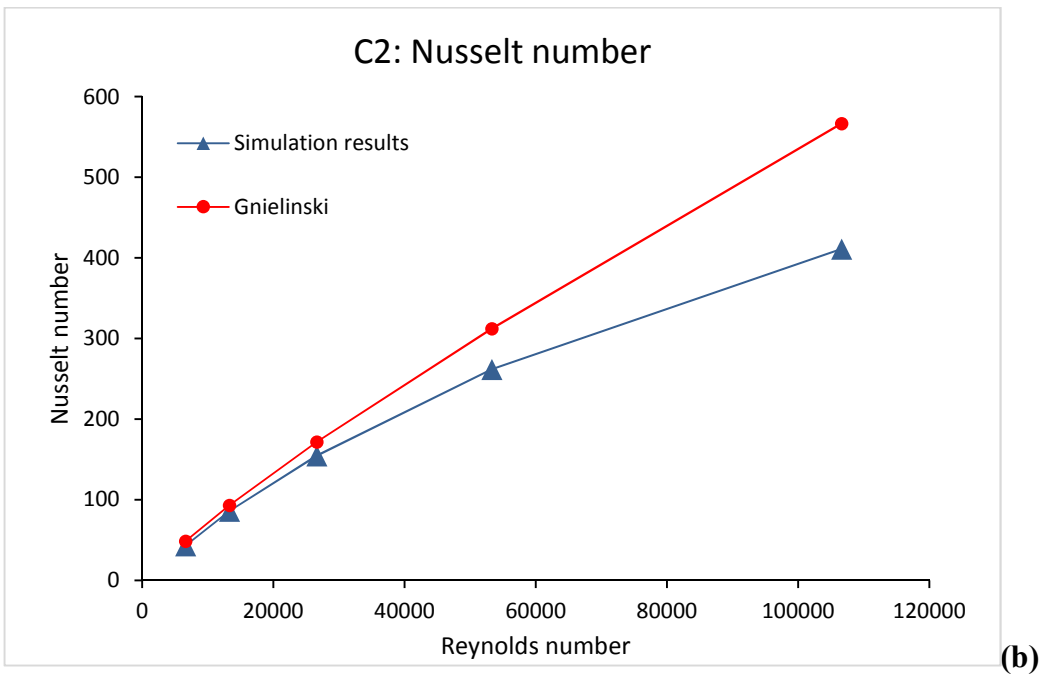
3.3 Parametric study

3.3.1 Nusselt number

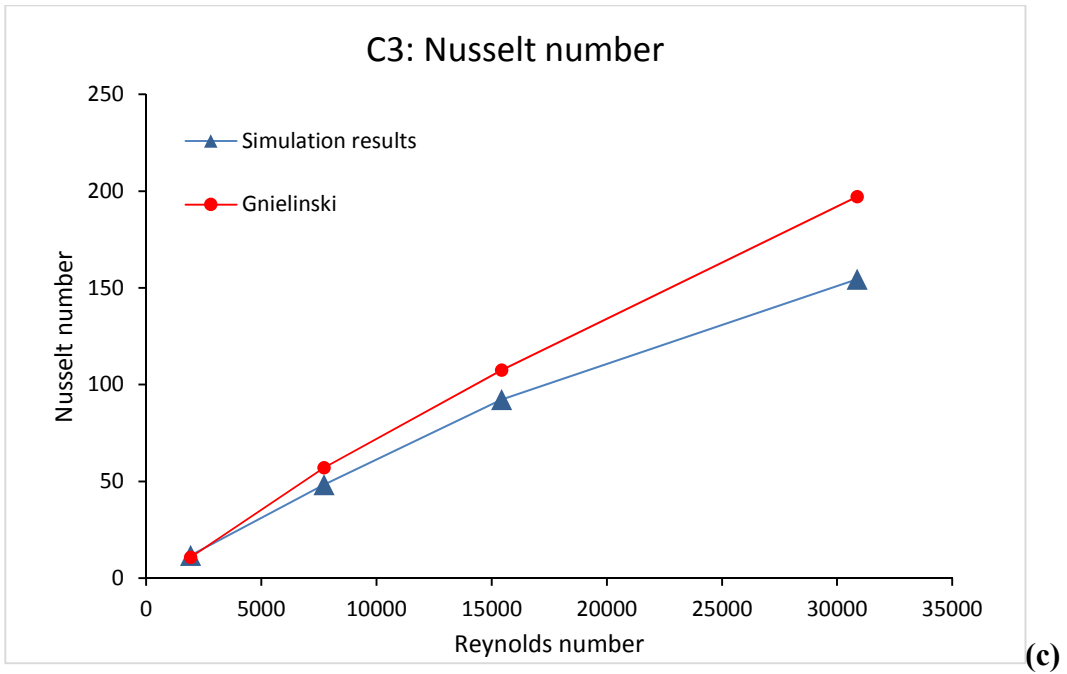
In the simulation parameter investigation, the friction drop measured via the Darcy friction factor and the Nusselt number were compared to (Equation 3-2). The results are shown in Figure 3.4 (**a-d**), showing excellent agreement in the Reynolds number range $6000 < Re < 25000$. At Reynolds numbers above 40000, the results start to diverge. For the larger diameters of geometries C3 and C4 the results diverge more strongly. This may be explained by the larger difference between the bulk and wall Prandtl-numbers in cases with larger hydraulic diameter and faster flow rates.



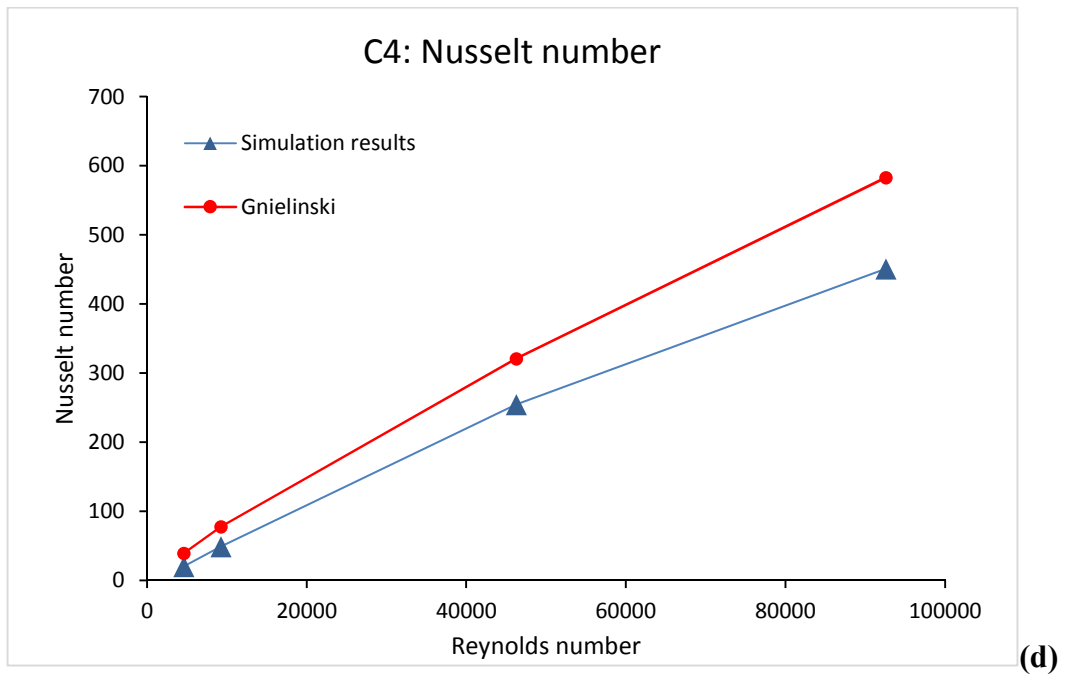
(a)



(b)



(c)

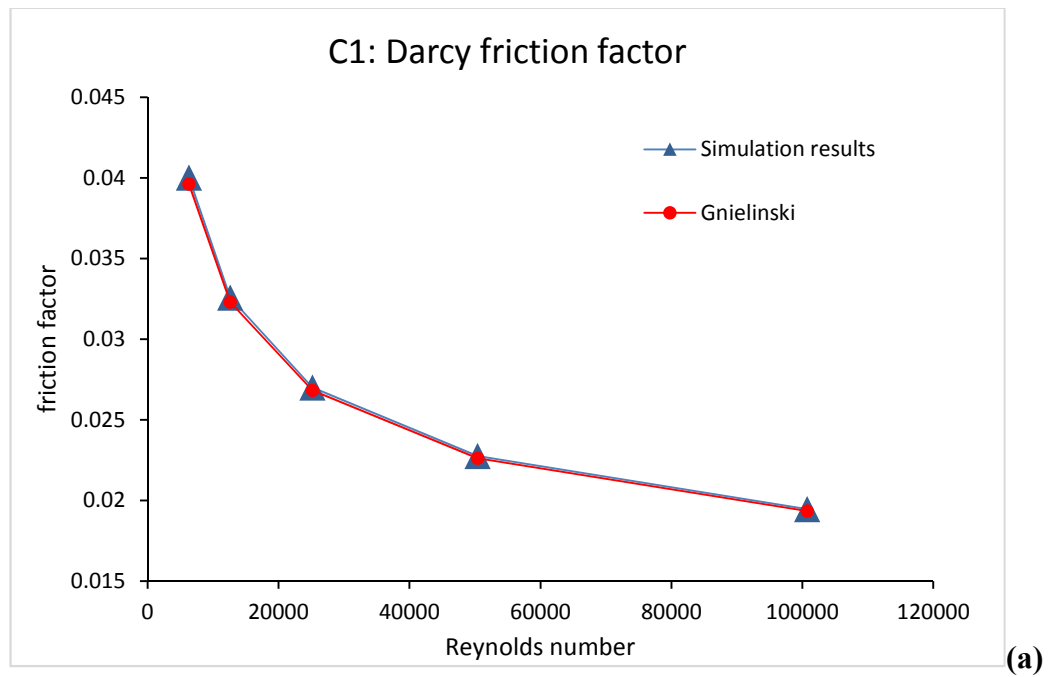


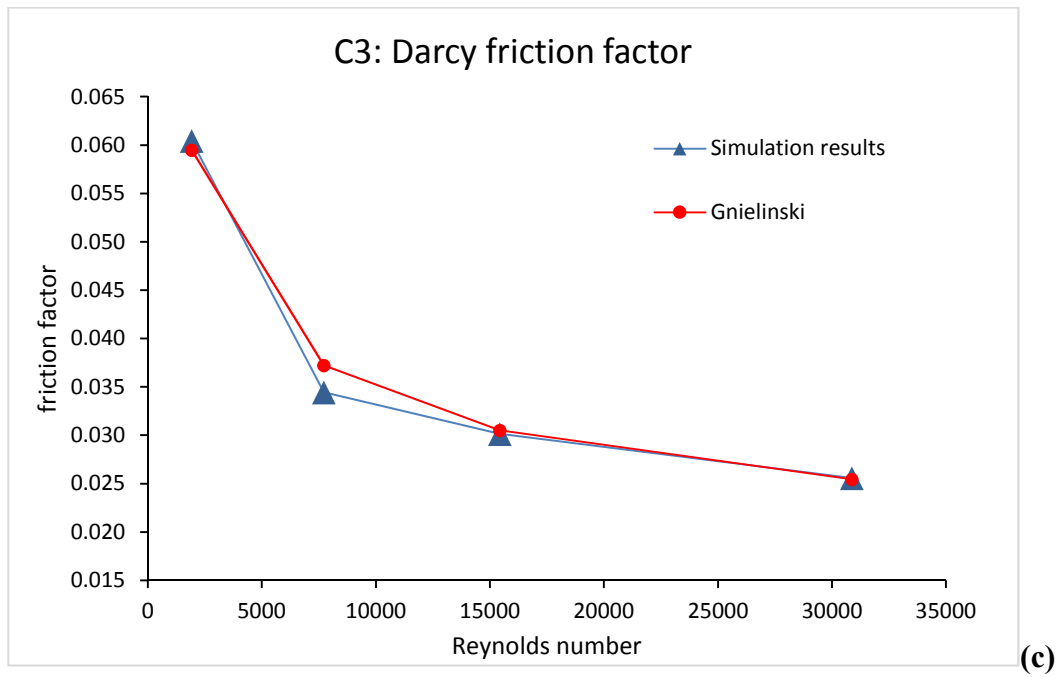
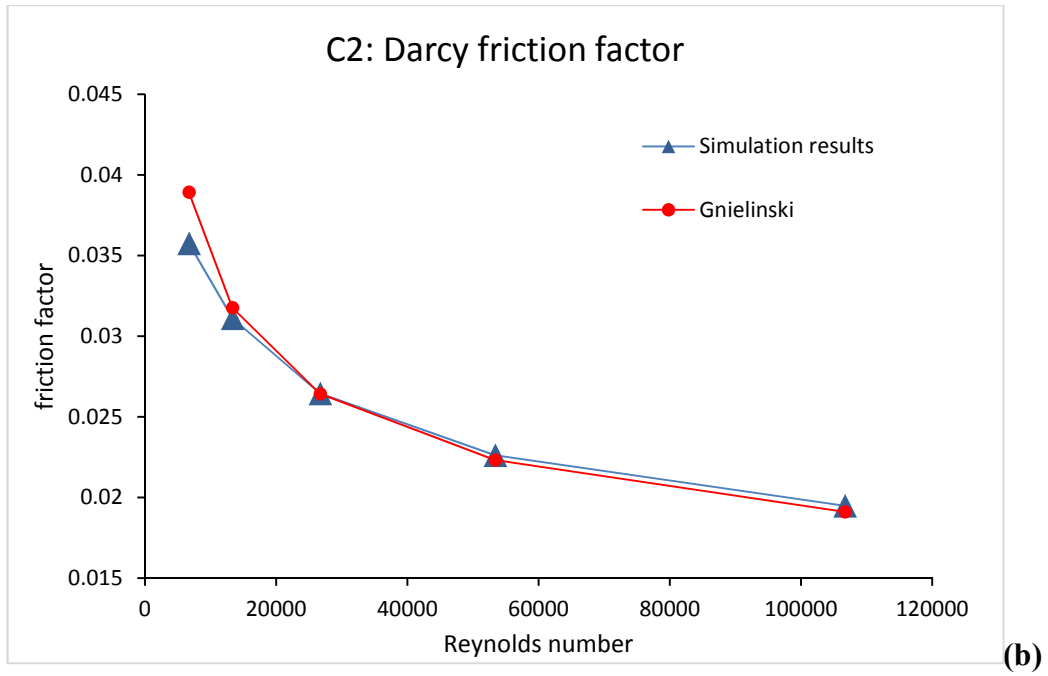
(d)

Figure 3.4 (a-d) Comparison between FLUENT heat-exchanger simulations and (Equation 3-2).

3.3.2 Darcy friction factor

The simulated Darcy friction factor were compared with (Equation 3-4), as shown in Figure 4. The results agree very well for the narrow channels C1, C2 and C3. For the largest channel C4, the simulation under-predicts the pressure drop given by (Equation 3-4).





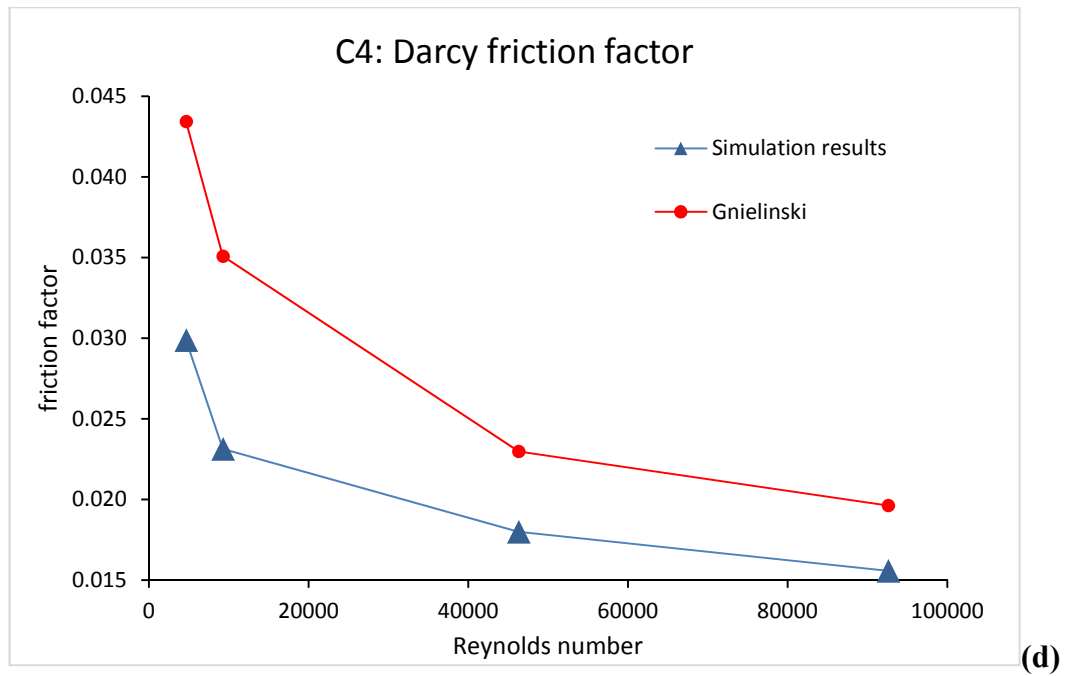


Figure 3.5 (a-d) Comparison between FLUENT simulations and (Equation 3-4) for Darcy Friction factor.

3.4 Bubbler simulations

Following the validation of the FLUENT model, the next step was to investigate heat transfer in various different bubbler geometries. The Gnielinski correlation uses a geometric parameter F_{ann} to fit experimental results to different heat transfer boundary conditions. (Equation 3-3) is used for the boundary condition of “heat transfer at the inner wall with the outer wall insulated”. [57]

Gnielinski remarks that no experimental data exists to fit an equation to the boundary condition “heat transfer at both the outer and inner wall of the annulus”. [57] For the current bubbler geometry, the flow far from the tip asymptotically approaches the aforementioned case, and the simulation results can be used to formulate an equation. The parametric study showed that the results of the FLUENT simulations can be considered accurate in the Reynolds number range $6000 < Re < 25000$ and for sufficiently thin annuli: $D_H < 5$ mm. To establish a value for F_{ann} for the bubbler case, a large quantity of bubbler simulations was carried out for geometries with varying D_i/D_o ratios. The results were used to establish an estimate for the parameter F_{ann} for the two-sided heat transfer boundary condition:

$$F_{ann} = 0.945\alpha^{0.047} \quad \text{(Equation 3-14)}$$

A comparison between (Equation 3-14) and (Equation 3-3) is shown in Figure 3.6. It is apparent that the value of (Equation 3-14) is very close to one, and its physical meaning is unclear [57], making its inclusion dubious in the model with two-sided heat transfer. The color of the data

points indicates the Reynolds number of the flow, with red points corresponding to higher Re-number flows, and blue points to lower Re-number flows. The variation in predicted heat transfer appears to correlate with the Reynolds number. This variation might be caused by the factor K in (Equation 3-7), which takes into account the temperature dependence of material properties. As mentioned earlier, the error caused by ignoring the temperature dependence might be magnified at high Reynolds-numbers flows, where the bulk fluid has less time to warm up, and temperature gradients are thus larger. The parameters for all the bubbler simulations are shown in Table 3.3.

The results for three simulated cases are shown in Figure 3.7, Figure 3.8 and Figure 3.9. The simulation parameters for these cases are presented in Table 3.4. The simulations predict a large increase in heat transfer close to the bend in the “impingement zone”, where the flow impinges on the outer wall and increases in velocity. On the other hand, a dead zone is observed at the hemispherical tip, where heat transfer and fluid flow are dampened. For the geometries with low diameter ratio value a , such as G3 (Figure 3.9), the flow separates and forms a vortex, causing a large pressure drop and concomitant increase in heat transfer.

(Equation 3-2) adjusted with the F_{ann} values from (Equation 3-14) is able to predict the simulated Nusselt number at the asymptote within a 15% margin of error.

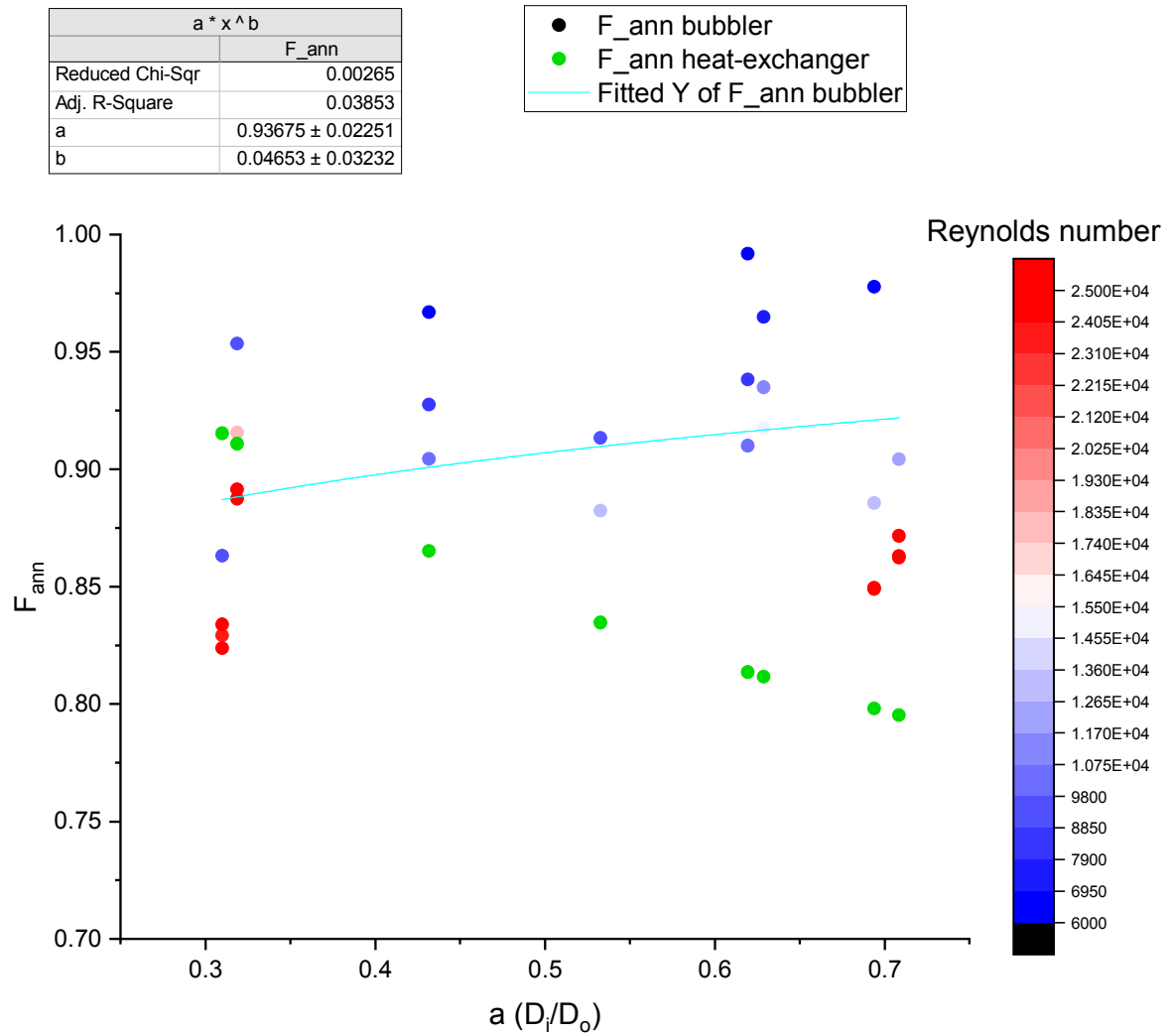


Figure 3.6 Comparison of geometric parameter F_{ann} for heat-exchangers (Gnielinski, green) and Bubblers (present study, red-blue).

Table 3.3 Simulation parameters for determination of bubbler F_{ann} .

Inner tube diameter, m	Outer annulus diameter, m	a (D_o/D_i)	Length (m)	Inner tube Reyn. number	Outer annulus Reyn. number	F_{ann} for heat-exch. (Gniel.)	F_{ann} for bubbler (pres. study)	Nu Number Simul.
2.95E-03	2.09E-03	7.08E-01	1.00E-01	1.75E+04	6.30E+03	7.95E-01	1.01E+00	5.70E+01
2.95E-03	2.09E-03	7.08E-01	1.00E-01	3.51E+04	1.26E+04	7.95E-01	9.04E-01	9.81E+01
2.95E-03	2.09E-03	7.08E-01	1.00E-01	7.01E+04	2.52E+04	7.95E-01	8.72E-01	1.74E+02
2.95E-03	2.09E-03	7.08E-01	1.00E-01	1.40E+05	5.04E+04	7.95E-01	8.63E-01	3.14E+02
2.95E-03	2.09E-03	7.08E-01	1.00E-01	2.10E+05	7.56E+04	7.95E-01	8.62E-01	4.45E+02
5.62E-03	3.90E-03	6.94E-01	1.00E-01	1.75E+04	6.67E+03	7.98E-01	9.78E-01	6.00E+01
5.62E-03	3.90E-03	6.94E-01	1.00E-01	3.51E+04	1.33E+04	7.98E-01	8.86E-01	1.04E+02
5.62E-03	3.90E-03	6.94E-01	1.00E-01	1.40E+05	5.33E+04	7.98E-01	8.50E-01	3.33E+02
5.62E-03	3.90E-03	6.94E-01	1.00E-01	2.45E+05	9.33E+04	7.98E-01	8.49E-01	5.38E+02
1.06E-02	3.38E-03	3.19E-01	2.00E-01	4.09E+04	9.08E+03	9.11E-01	9.53E-01	8.13E+01
1.06E-02	3.38E-03	3.19E-01	2.00E-01	8.19E+04	1.82E+04	9.11E-01	9.16E-01	1.46E+02
1.06E-02	3.38E-03	3.19E-01	2.00E-01	2.05E+05	4.54E+04	9.11E-01	8.87E-01	3.14E+02
1.06E-02	3.38E-03	3.19E-01	2.00E-01	1.43E+05	3.18E+04	9.11E-01	8.91E-01	2.31E+02
2.09E-02	6.49E-03	3.10E-01	2.00E-01	4.09E+04	9.26E+03	9.15E-01	8.63E-01	7.93E+01
2.09E-02	6.49E-03	3.10E-01	2.00E-01	1.02E+05	2.31E+04	9.15E-01	8.29E-01	1.73E+02
2.09E-02	6.49E-03	3.10E-01	2.00E-01	2.04E+05	4.63E+04	9.15E-01	8.24E-01	3.13E+02
2.09E-02	6.49E-03	3.10E-01	2.00E-01	4.09E+05	9.26E+04	9.15E-01	8.34E-01	5.75E+02
2.02E-02	1.27E-02	6.29E-01	2.00E-01	2.04E+04	7.72E+03	8.12E-01	9.65E-01	7.10E+01
2.02E-02	1.27E-02	6.29E-01	2.00E-01	3.07E+04	1.16E+04	8.12E-01	9.35E-01	1.00E+02
2.02E-02	1.27E-02	6.29E-01	2.00E-01	4.09E+04	1.54E+04	8.12E-01	9.18E-01	1.27E+02
4.28E-03	2.28E-03	5.33E-01	1.50E-01	1.90E+04	5.81E+03	8.35E-01	1.01E+00	5.32E+01

4.28E-03	2.28E-03	5.33E-01	1.50E-01	3.17E+04	9.68E+03	8.35E-01	9.13E-01	7.89E+01
4.28E-03	2.28E-03	5.33E-01	1.50E-01	4.44E+04	1.35E+04	8.35E-01	8.82E-01	1.03E+02
5.28E-03	2.28E-03	4.32E-01	2.00E-01	2.54E+04	6.72E+03	8.65E-01	9.67E-01	5.93E+01
5.28E-03	2.28E-03	4.32E-01	2.00E-01	3.17E+04	8.40E+03	8.65E-01	9.27E-01	7.04E+01
5.28E-03	2.28E-03	4.32E-01	2.00E-01	3.81E+04	1.01E+04	8.65E-01	9.04E-01	8.14E+01
3.68E-03	2.28E-03	6.20E-01	1.50E-01	1.90E+04	6.39E+03	8.14E-01	9.92E-01	5.71E+01
3.68E-03	2.28E-03	6.20E-01	1.50E-01	2.54E+04	8.52E+03	8.14E-01	9.38E-01	7.12E+01
3.68E-03	2.28E-03	6.20E-01	1.50E-01	3.17E+04	1.06E+04	8.14E-01	9.10E-01	8.49E+01

Table 3.4 Selected bubbler simulation parameters

Geometry	Inner tube diameter, m	Outer annulus diameter, m	Length, m	Water temperature K	Wall temperature, K	Reynolds number
G1	2.09e-3	2.95e-3	0.1	300	350	6300
G2	3.9e-3	5.62e-3	0.1	300	350	6700
G3	6.49e-3	2.09e-2	0.2	300	350	9300

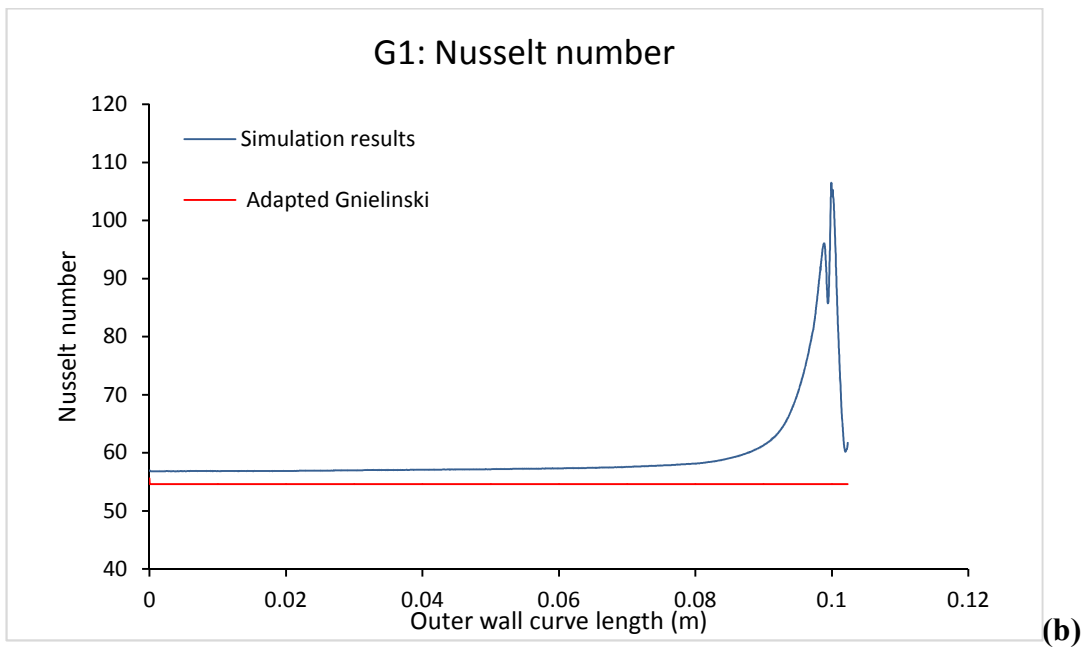
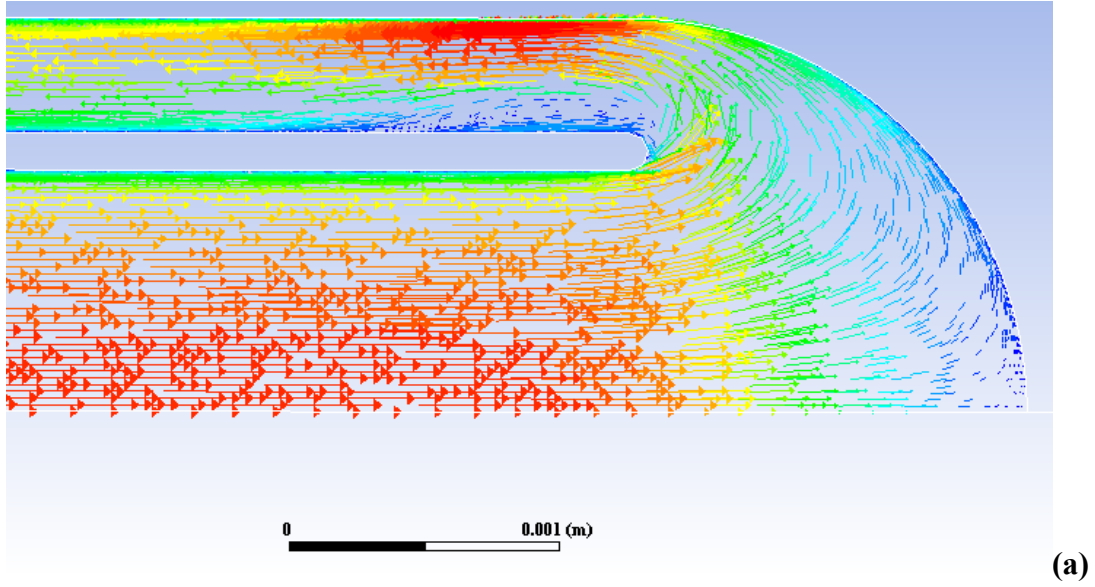


Figure 3.7 **(a)** G1 geometry flow streamlines. **(b)** Predicted Nusselt number using new correlation and FLUENT simulation. Reynolds number is 6.3×10^3 .

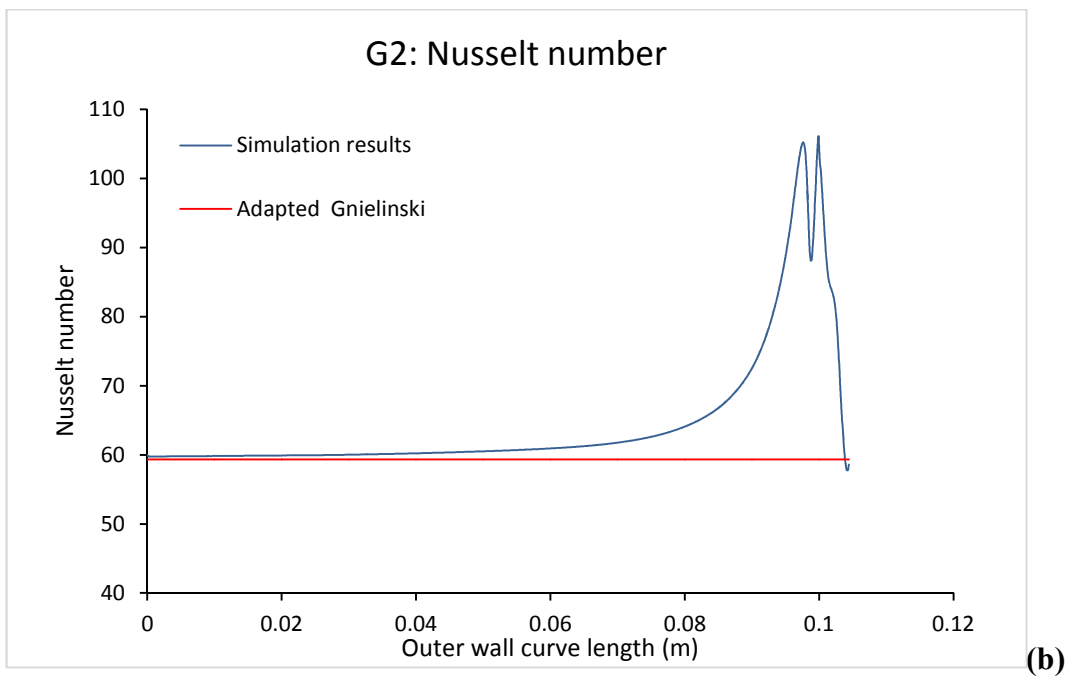
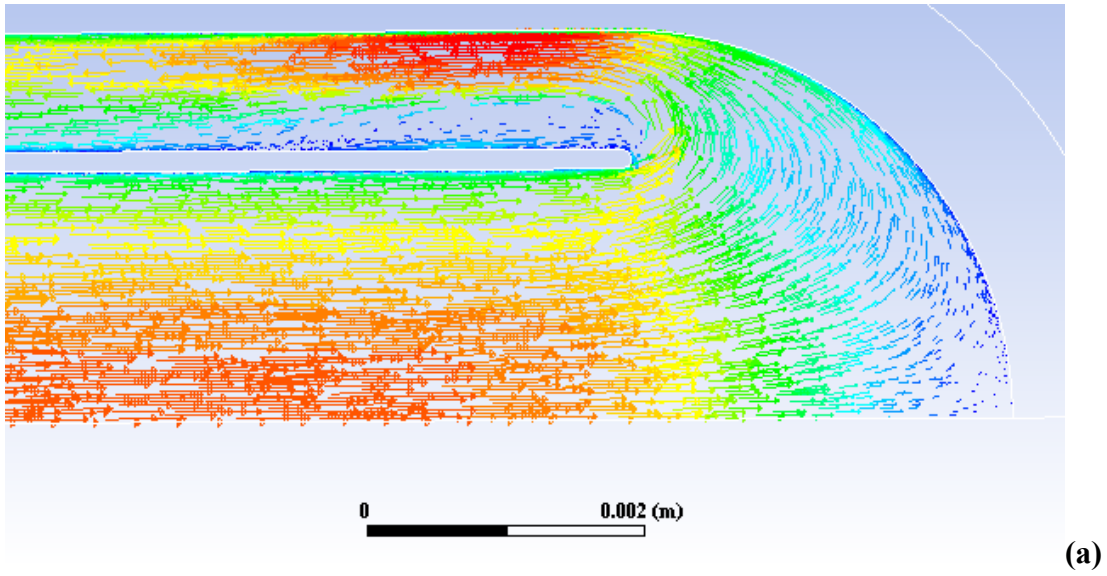


Figure 3.8 **(a)** G2 geometry flow streamlines. **(b)** Predicted Nusselt number using new correlation and FLUENT simulation. Reynolds number is $6.7e3$.

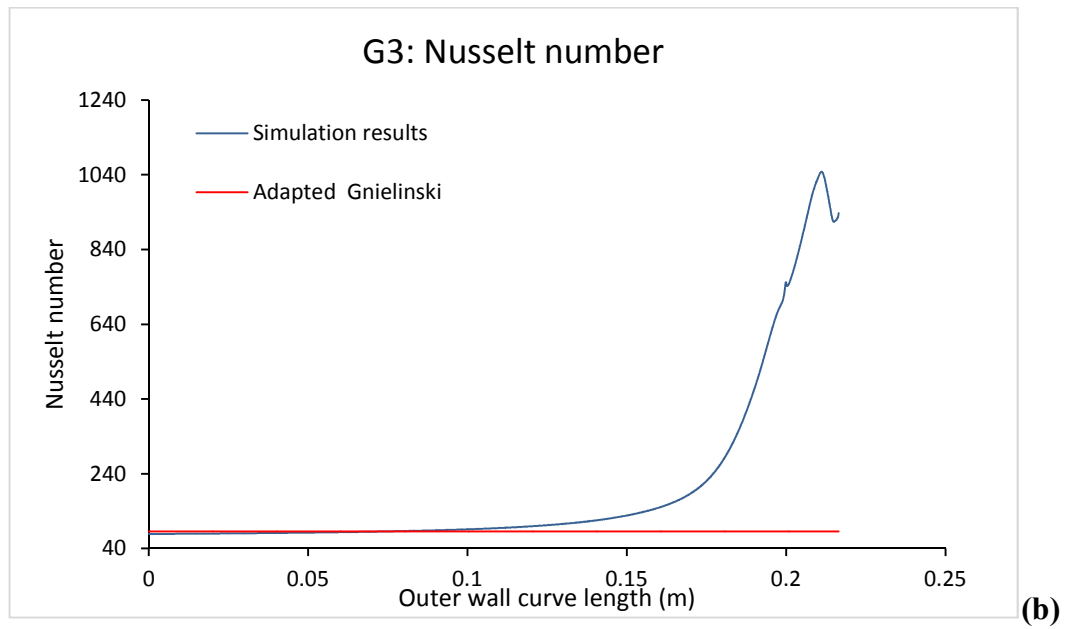
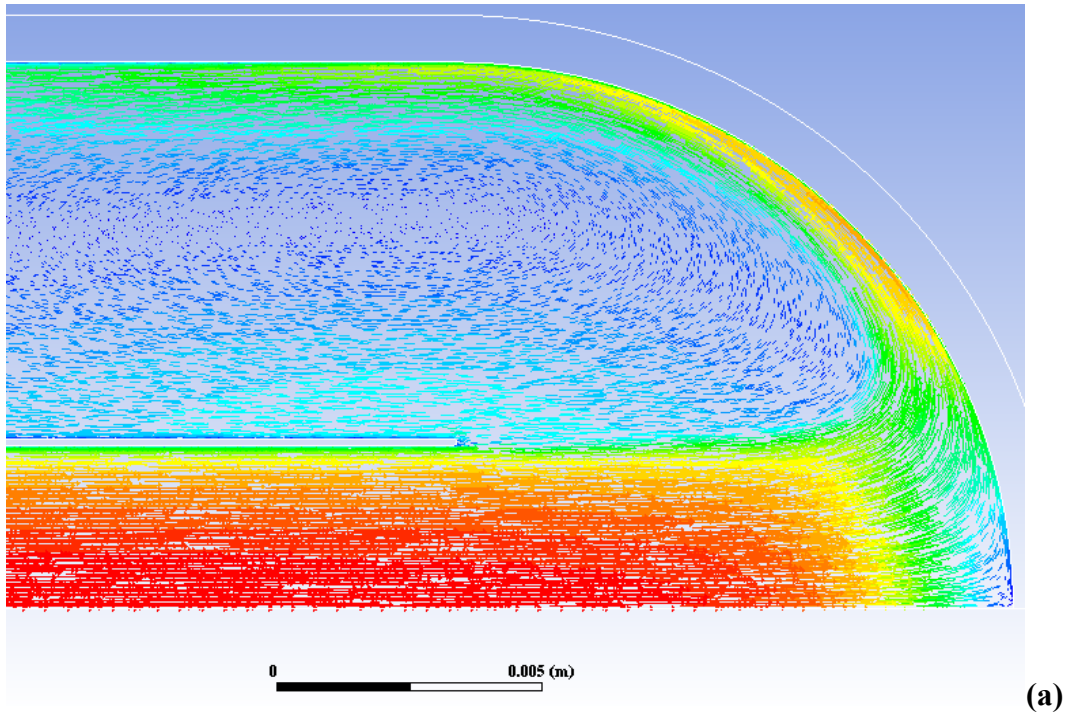


Figure 3.9 (a) G3 geometry flow streamlines. (b) Predicted Nusselt number using new correlation and FLUENT simulation. Reynolds number is $9.3e3$.

3.5 Conclusions

- 1) The 2D axisymmetric simulation of the double-pipe heat exchanger in section 4 was in very good agreement with the Gnielinski correlation in the Reynolds number range of $6000 < Re < 25000$ for straight concentric tubes with annular hydraulic diameter $D_H < 5$ mm, with the assumption of constant material properties and no influence of gravity. At higher Reynolds number and larger diameters, the temperature dependence of material properties may become non-negligible, causing the simulation to under-predict heat transfer.
- 2) A new equation for the geometric fitting parameter F_{ann} was found for two-sided heat-transfer in annular tubes. However, the value is so close to 1 as to call into question its necessity. (Equation 3-14) has good match with simulation results in the given range of conditions, and it is applicable for modelling the straight portion of “bubbler” cooling channels in the HPDC process.
- 3) At the side walls of the bubbler tip, impingement of the flow against the outer shell intensifies heat transfer. The intensification profile is dependent on the tip geometry and flow speed, and needs to be determined for each channel setup individually. In the future, experiments for bubbler cooling channels should be carried out to validate the Nusselt number profile at the tip and to establish an empirical equation for the tip.
- 4) For a hemispherical geometry, a dead zone at the tip was observed, significantly reducing heat transfer at the tip of the cooling channel.
- 5) Increasing the ratio between the annular diameter and the inner pipe diameter will cause the flow to separate, increasing pressure loss and intensifying heat transfer at the impingement zone greatly

CHAPTER 4 – HEAT TRANSFER MODEL FOR THE DIE-CASTING INTERFACE

4.1 Introduction

Several experimental studies have been made about IHTC in HPDC. However, only few studies explore the fundamental underlying physical phenomena of heat transfer between solidifying metal on a microscopically rough surface. Some work exists for heat transfer in droplet impacts [49] [60]. The only model for HPDC is by Hamasaiid et al. [25] [18]. They study the evolution of IHTC for both the Al-alloy A380 and the magnesium alloy AZ91D.

Hamasaiid modelled the surface roughness of the mould as conical asperities with a Gaussian height distribution. This model has been successfully applied to predict IHTC for bitumen [51] and thermal interface materials (TIM) [50]. However, the model's original goal of modelling IHTC in HPDC has remained problematic, due to the added complexity introduced by rapid melt solidification and high pressure. Our goal is to relax some of the empirical assumptions made by Hamasaiid based on a re-analysis of their data and simulations carried out in ANSYS FLUENT 18.1. The strategy of the present study is visualized in Figure 4.1

4.2 Mathematical models

4.2.1 Interfacial heat transfer coefficient

The model for IHTC is found on Cooper flux tube theory. [61] This model predicts the thermal resistance between two separate surfaces connected at one point by a contact spot.

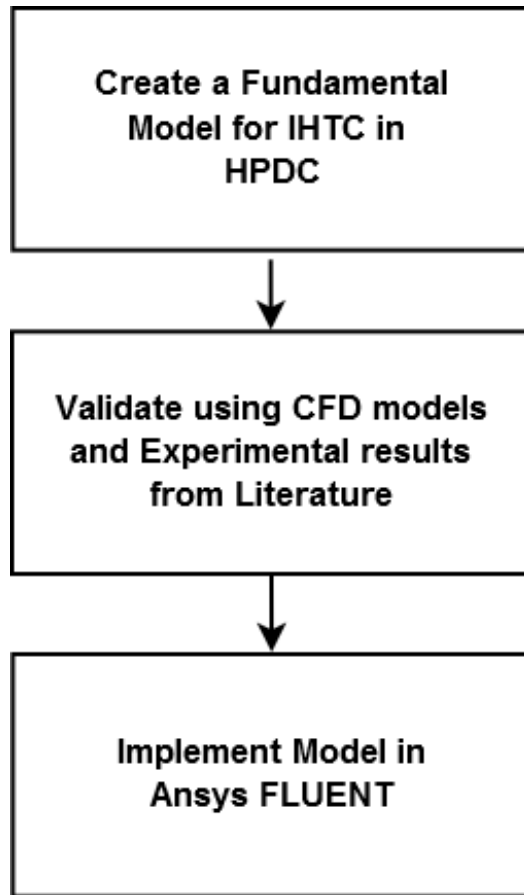


Figure 4.1 Strategy for developing IHTC model

The equation is given by

$$r_c = \frac{\left(1 - \frac{a_s}{b_s}\right)^{1.5}}{2\lambda a_s} \quad \text{(Equation 4-1)}$$

where a_s is the radius of the microcontact spot, b_s is the radius of the heat flux tube. λ is the harmonic mean thermal conductivity [61], given by

$$\lambda = \frac{2k_1k_2}{(k_1 + k_2)} \quad (\text{Equation 4-2})$$

where k_1 and k_2 are the thermal conductivities of the two materials in contact.

The overall resistance between the two real surfaces can be found by calculating the thermal resistance of all microcontact points connected in parallel:

$$R_c = \frac{r_c}{n_s} = \frac{\left(1 - \frac{\langle a_s \rangle}{\langle b_s \rangle}\right)^{1.5}}{2\lambda n_s \langle a_s \rangle} \quad (\text{Equation 4-3})$$

where $\langle a_s \rangle$ and $\langle b_s \rangle$ are the average micro-contact spot and heat flux tube radii respectively. n_s is the area density of the microcontact spots. The total heat transfer coefficient is then given by

$$h = \frac{1}{R_c} = \frac{2\lambda n_s \langle a_s \rangle}{\left(1 - \frac{\langle a_s \rangle}{\langle b_s \rangle}\right)^{1.5}} \quad (\text{Equation 4-4})$$

Hamasaiid was able to derive expressions for $\langle a_s \rangle$, $\langle b_s \rangle$ and n_s assuming a surface profile of conical asperities following a Gaussian height distribution in partial contact with the liquid. Two measured surface roughness parameters were used for this model: the mean asperity height σ and the mean peak spacing R_{sm} . The surface profile model by Hamasaiid et al. is visualized in Figure 4.2 Surface profile description by Hamasaiid et al. [18]Figure 4.2.

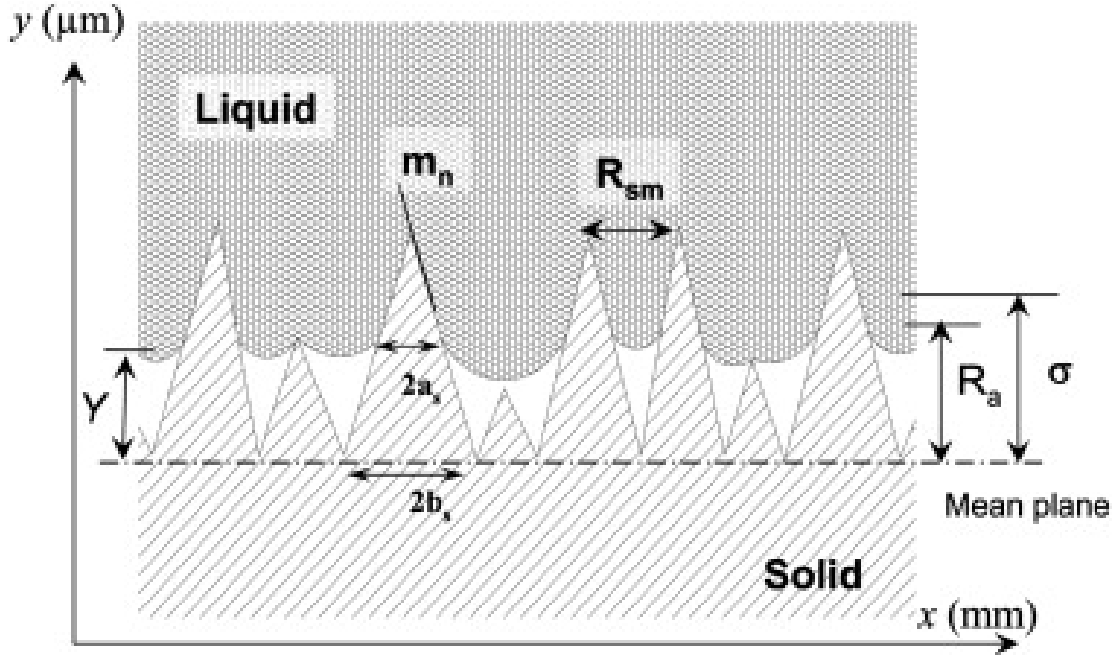


Figure 4.2 Surface profile description by Hamasaiid et al. [18]

The complete derivations for $\langle a_s \rangle$, $\langle b_s \rangle$ and n_s can be found in [18, 25]. However, care should be taken, since there are typographical errors in eq. 46 in [18] and equations 26 and 28 in [25]. The equation for the area asperity density n_s for the model is given by

$$n_s = \frac{8}{\epsilon \pi^2} \left(\frac{1}{R_{sm}} \right)^2 \operatorname{erfc} \left(\frac{Y}{\sqrt{2}\sigma} \right) \quad (\text{Equation 4-5})$$

where Y is the width of the air gap measured from the mean plane to the liquid surface, ϵ is a numeric parameter determined from image analysis equal to 1.5, and erfc is the complementary error function. The average radius of the microcontact spot $\langle a_s \rangle$ is given by

$$\langle a_s \rangle = \frac{1}{4} R_{sm} \left(2 \exp\left(-\frac{Y}{2\sigma^2}\right) + \frac{Y\sqrt{2\pi}}{\sigma} \operatorname{erfc}\left(\frac{Y}{\sqrt{2}\sigma}\right) \right) \quad (\text{Equation 4-6})$$

Finally, the average radius of the heat flux tubes is equal the radius of the base of the asperity cone:

$$\langle b_s \rangle = \frac{R_{sm}}{2} \quad (\text{Equation 4-7})$$

4.2.2 Air gap thickness

The value of the interfacial heat transfer coefficient thus becomes a function of mean asperity height σ , mean peak spacing R_{sm} and air gap width Y . The peak spacing and height need to be determined experimentally using a profilometer. This leaves the air gap width as the only unknown. To determine the value of the air gap width at the initial impact of the melt with the die surface, Hamasaiid used the ideal gas law to formulate the following expression:

$$Y = \frac{\sqrt{2}\sigma}{\pi^{1/6}} \left(\frac{P_0 T_1}{(P_1 \pm P_\gamma) T_0} \right)^{1/3} \quad (\text{Equation 4-8})$$

where P_0 and T_0 are the pressure and temperature at NTP-conditions. P_1 and T_1 are temperature and pressure during liquid metal impact. P_γ is the capillary pressure, and its sign depends on the wetting conditions between the liquid and the die surface. Positive sign indicates good wetting, while negative sign indicates poor wetting.

To determine the value for the impact pressure P_1 , Hamasaiid used pressure measurements taken from the casting during die-filling at two locations: the gate location and the rib location. The sensor locations and the geometry of their casting are shown in Figure 4.3.

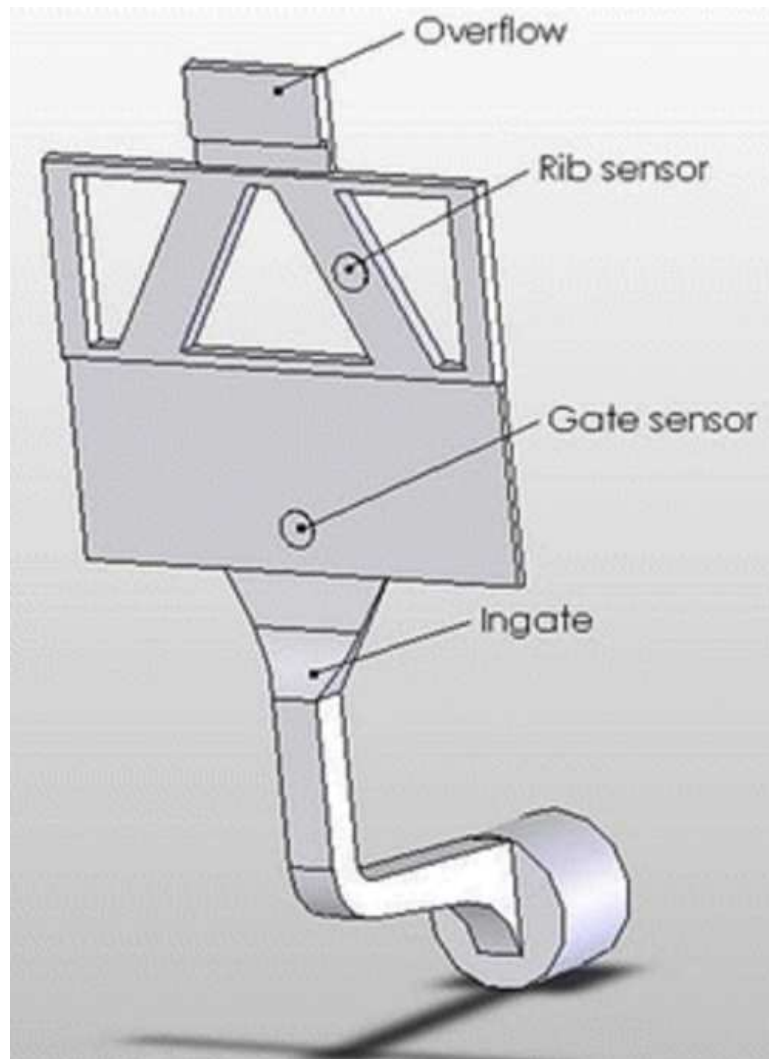


Figure 4.3 Casting geometry and sensor locations [12]

The measured temperature and pressure evolution at these locations is shown in Figure 4.4. They determined the impact pressure to be 26 MPa at the gate location.

Without accounting for the capillary pressure P_c and using a measured impact pressure value of $P_1 = 26$ MPa, the gap width estimated using this method was found to lead to estimated peak heat fluxes 5 times too large. The comparison between the model and experimental results for the two materials studied, A380 and AZ91D, is shown in Figure 4.5.

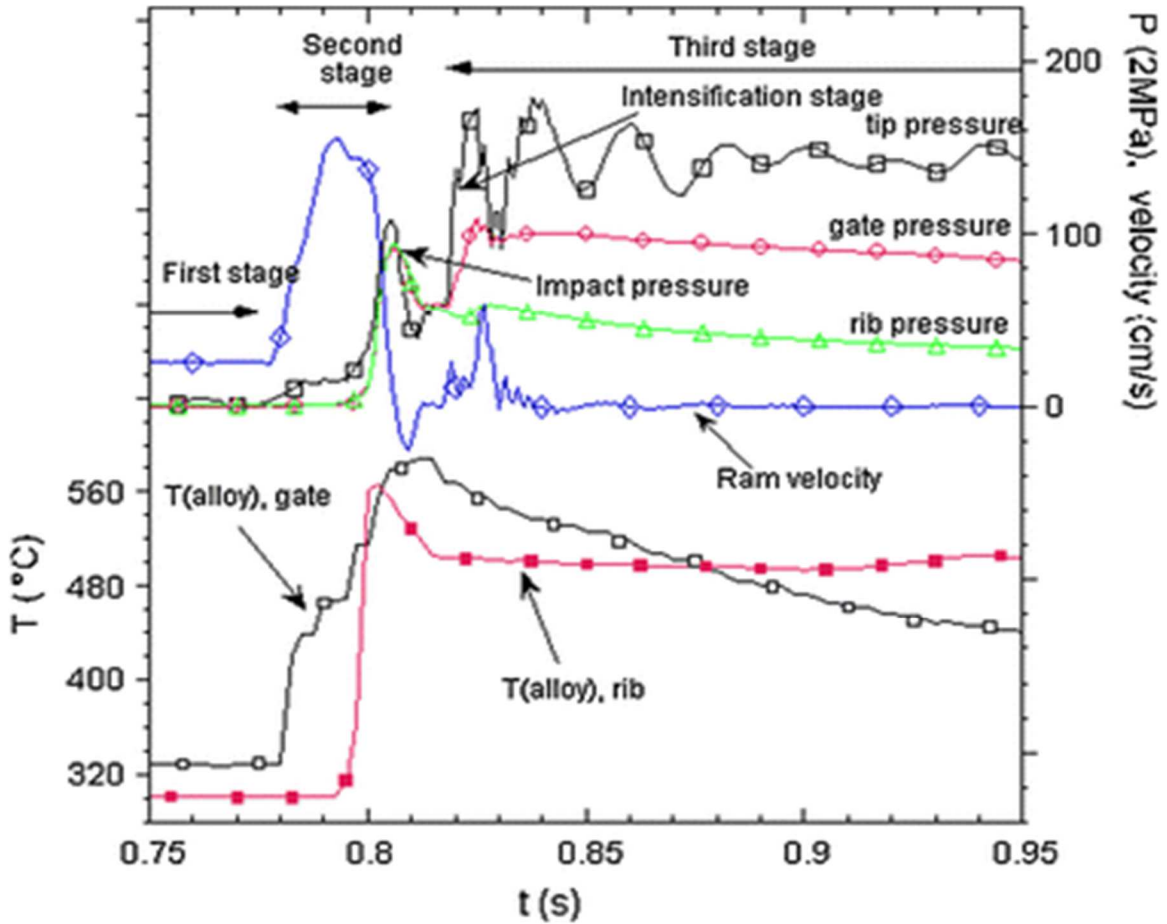


Figure 4.4 Temperature and pressure evolution in HPDC [12]

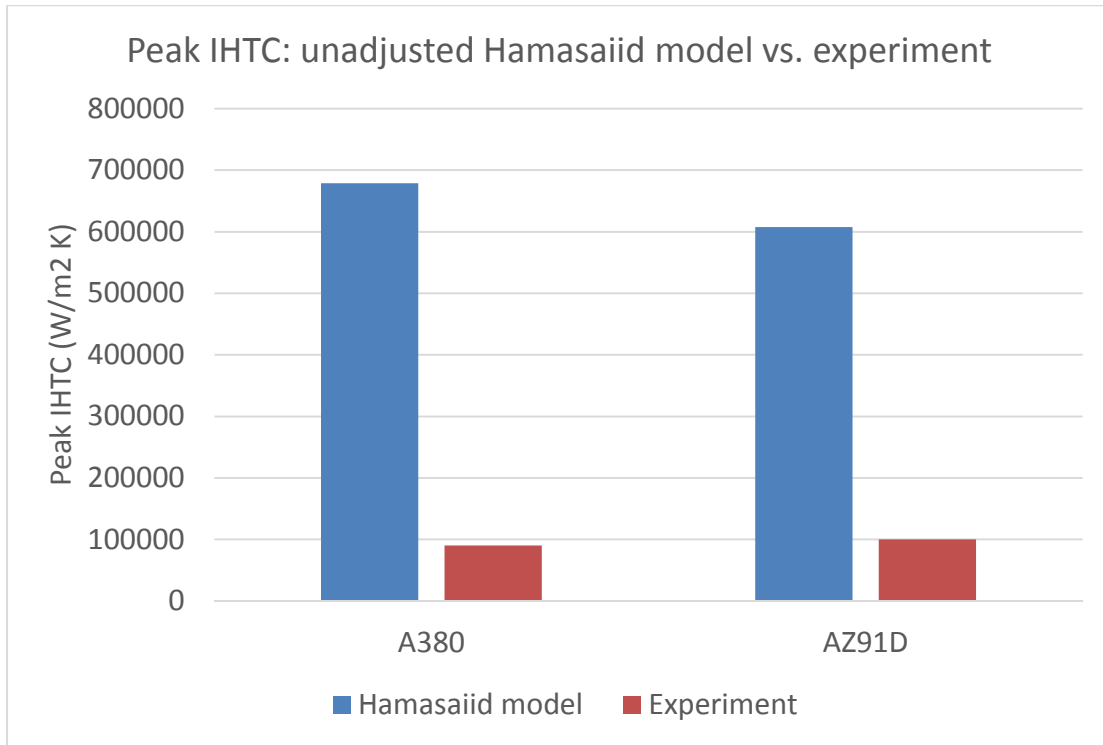


Figure 4.5 Comparison of experimental IHTC and model by Hamasaiid when neglecting the effect capillary pressure.

4.2.4 Capillary pressure

Due to this result, Hamasaiid determined that the capillary pressure must account for the difference between the model and the experimental results. Empirically, they determined P_γ to be negative (poor wetting) and for it to follow the relation:

$$P_\gamma = -0.87P_1 \quad (\text{Equation 4-9})$$

where P_1 is the melt impact pressure. Using the measured impact pressure $P_1 = 26$ MPa, $P_Y = -22.62$ MPa.

We will examine the validity of this assumption. The magnitude of the capillary pressure can be determined from Young's equation, if the contact angle between the die and melt is known. This approach has been used by Prasher et al. to determine the capillary pressure between thermal interface materials (TIM) and rough substrates. [62] They used a model visualized in Figure 4.6 for a conical air gap in contact with a solid substrate and liquid, where ϕ is the angle between the cone of air and the mean plane, and θ is the contact angle between melt and the substrate.

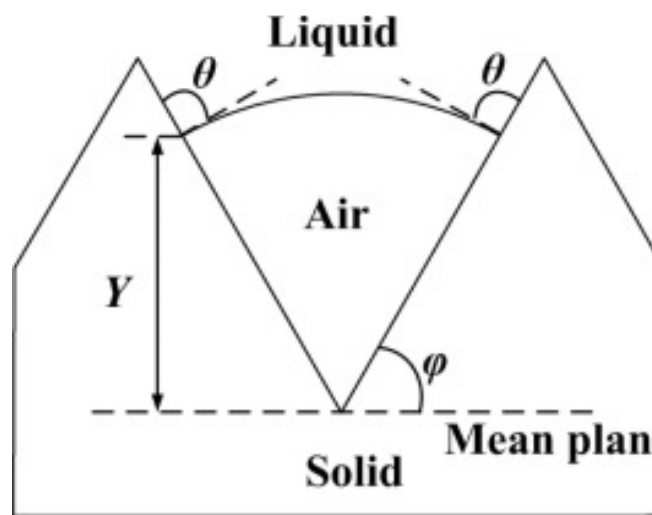


Figure 4.6 Conical air gap model [62]

Using this air gap model, Yuan et al. [50] developed the following expression for capillary pressure:

$$P_{\gamma} = \pm \frac{2\gamma_l \sin(\theta + \phi)}{Y \cot \phi} \quad (\text{Equation 4-10})$$

where γ_l is the liquid surface tension.

Since the average slope of the asperity is known from the surface profile measurements of the die surface, the only remaining unknowns are the surface tension and wetting angle. Previous experimental studies on A380 have determined surface tension values of 1.07 N/m [49] and 0.781 N/m [63]. The wetting angle between aluminum and uncoated steel has been determined to be approximately 37°. [64] This would indicate good wetting conditions, counter to the empirical assumption of Hamasaid. However, a recent study on the wetting behavior of aluminum alloys on H13 steel has found that the wettability is hugely affected by oxidation of the melt, substrate temperature, effect of surface coatings on the substrate and reactions between the melt and the substrate. [65] They found contact angles of 80° to 120° in the temperature range of 700° C to 800° C. To determine an estimate for the magnitude of the capillary pressure, we plotted out the absolute value of

(Equation 4-10) using parameter values in Table 4.1. The results are shown Figure 4.7.

The maximum capillary pressure (40 kPa) is 2 orders of magnitude smaller than the value for (Equation 4-9). Therefore we argue that the empirical capillary pressure term is incorrect.

Table 4.1 Parameter values for capillary pressure study

Parameter	Value	Source
γ_l	1.07	[49]
R_{sm}	128.7e-6	[25]
σ	0.578e-6	[25]
Y	3.5e-7	[25]

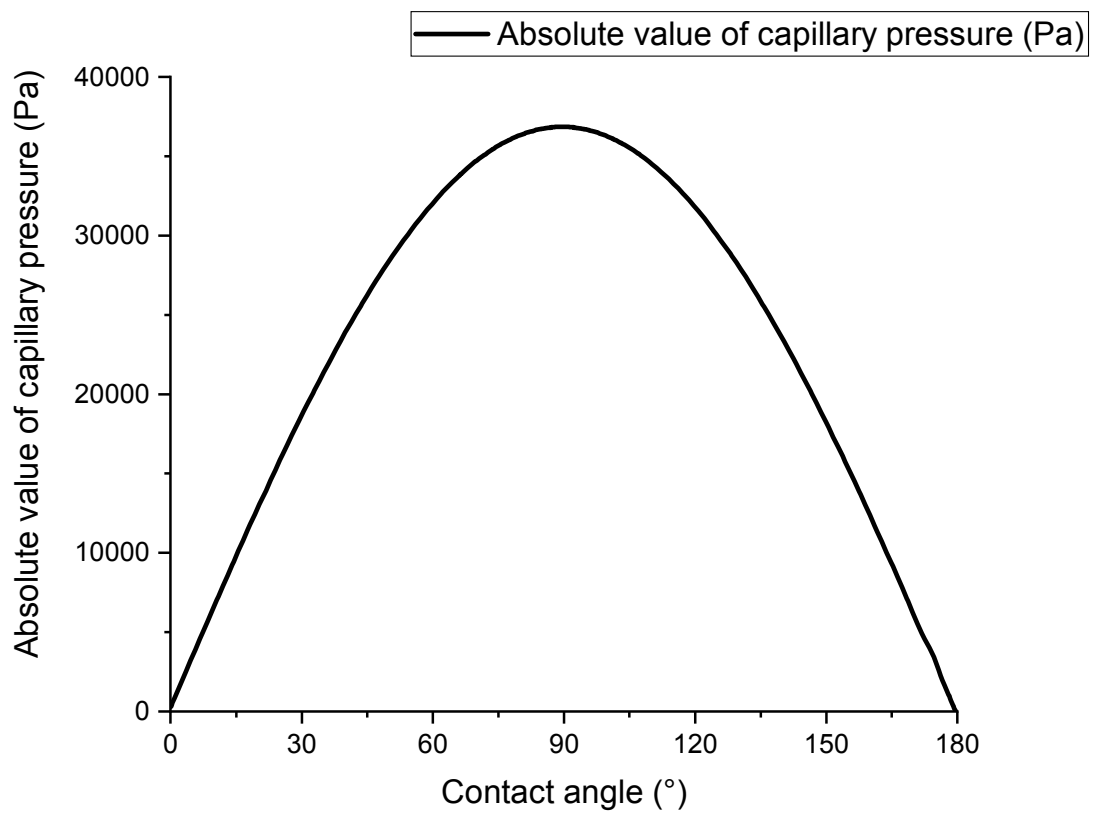


Figure 4.7 Absolute value of capillary pressure using (Equation 4-10) and values from Table 4.1.

The source of this confusion, we argue, is the misinterpretation of the impact pressure measurements. [62] The impact pressure highlighted in Figure 4.4 appears to be measured at the end of die filling, instead of the time of initial melt impact on the die. It may be that Hamasaiid mistaked the early onset of the intensification pressure for the impact pressure.

4.2.5 Impact pressure

To gain a better understanding of the true magnitude of the impact pressure in the HPDC process, we looked to literature. Chen et al. [17] suggested 2 possible models to calculate the impact pressure of melt in HPDC. One model is the stagnation pressure, applicable for modeling flow impingement in stagnation point flow. Stagnation point flow is fluid flow in the vicinity of a solid surface where the flow separates into two different streams. It is given by the equation:

$$\Delta P_s = \frac{1}{2} \rho v^2 \quad (\text{Equation 4-11})$$

where ρ is the fluid density and v is the upstream flow velocity. The values given by the stagnation pressure equation are on the order of $2e5$ Pa, too small to realistically reflect the casting metal – die impact.

Another model suggested by Chen is the water hammer pressure model. The water hammer pressure is the pressure wave caused by the hydraulic shock of fluid changing direction or stopping suddenly. This model successfully predicts the maximum impact pressure of droplets on a solid surface. [66]:

$$\Delta P_{whp} = \rho c v \quad (\text{Equation 4-12})$$

where c is the fluid sonic velocity, given by

$$c = \sqrt{\frac{E}{\rho}} \quad (\text{Equation 4-13})$$

where E is the bulk modulus of the fluid.

To find an estimate for the value of water hammer pressure, we looked for material properties from literature. To determine the velocity of the flow field at the sensor locations shown in Figure 4.3, we carried out die-filling simulations for a casting geometry based on the experimental setup in [15] [12] [16].

4.3 Die-filling simulation

4.3.1 Goals

The goal of the die-filling simulation was to determine the flow velocity inside the die during casting. This velocity can be used to calculate the value of the water hammer pressure, which can then be used as an input in the IHTC model. To ensure that the mesh sizing is sufficient for a realistic simulation, a mesh independence study was carried out. It should be noted that the resolution of the simulation is not sufficient to describe the initial liquid metal jet impact with the die wall with the level of detail of droplet impact simulations, but it can be used to determine the flow velocity field in the casting. The simulations were carried out at the high-

performance computing cluster at the University of Alabama. The material properties used in the simulation are found in Table 4.2. The simulation parameters for the study are found in Table 4.3. The geometry for the simulation, which takes use of symmetry, is shown in Figure 4.8.

Table 4.2 Material parameters for die-filling simulation

Material	Velocity (m/s)	Viscosity (Pa/s)	Density (kg/m ³)	Bulk modulus (GPa)
Al-9Si-3Cu	0.87	0.001 [67]	2800 [25]	41.3 [68]
AZ91D	1.53	0.0015 [69]	1800 [25]	20.4 [68]

Table 4.3 Simulation parameters for die-filling simulation

Parameter	
Turbulence model	K-omega SST
Mesh sizing	5e-4 m, 1e-3 m
Time-step	1e-5 s
Processors	32
Double precision	Yes
Calculation time	2 weeks
Solver	PISO
VOF global courant number criterion	0.5-1.5

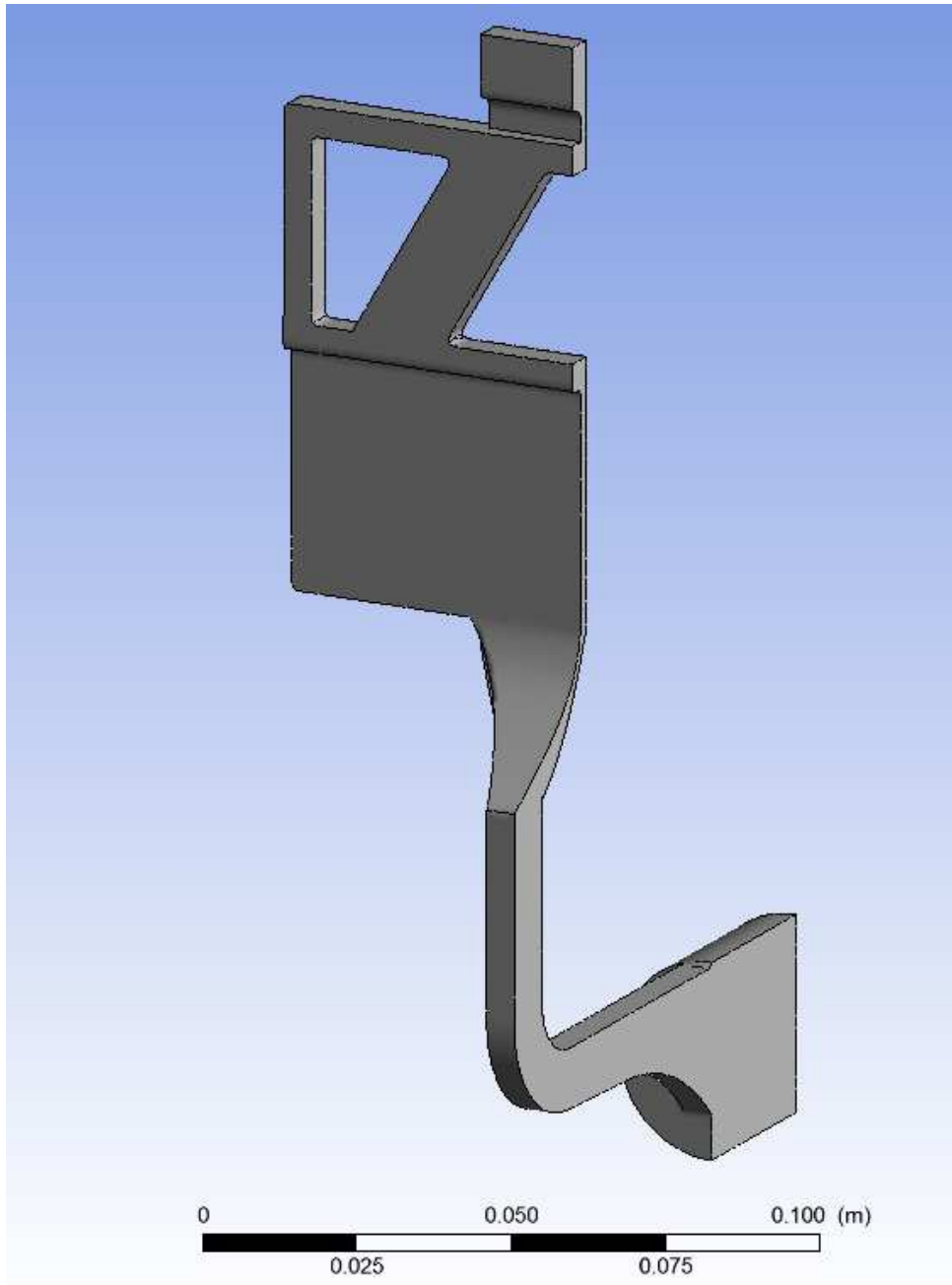


Figure 4.8 FLUENT simulation geometry

4.3.2 Mesh independence study

To make sure that the mesh size was sufficient to capture the turbulent behavior of the metal at the die-casting boundary, a mesh independence study was carried out. Two different mesh sizes were simulated: 1e-3 m and 5e-4 m. Both meshes are tetrahedral with no wall inflation layers. Wall inflation layers were tried but left out, since they caused numerical instability at the gate region. The material used was Al-9Si-3Cu and the piston velocity was 0.87 m/s.

The wall y^+ values and filling velocity were compared. For the k-omega SST turbulence model, the wall y^+ value should optimally be ~ 1 to accurately model boundary phenomena. [53] The results for the mesh independence study are shown Figure 4.9, Figure 4.10, Figure 4.11, Figure 4.12, Figure 4.13 and Figure 4.14.

Figure 4.9 shows that the wall y^+ value is on the order ~ 10 for the fine mesh (right) and order ~ 20 for the coarse mesh (left) at the gate location. We chose to use the finer mesh but not refine it further due to calculation capacity constraints.

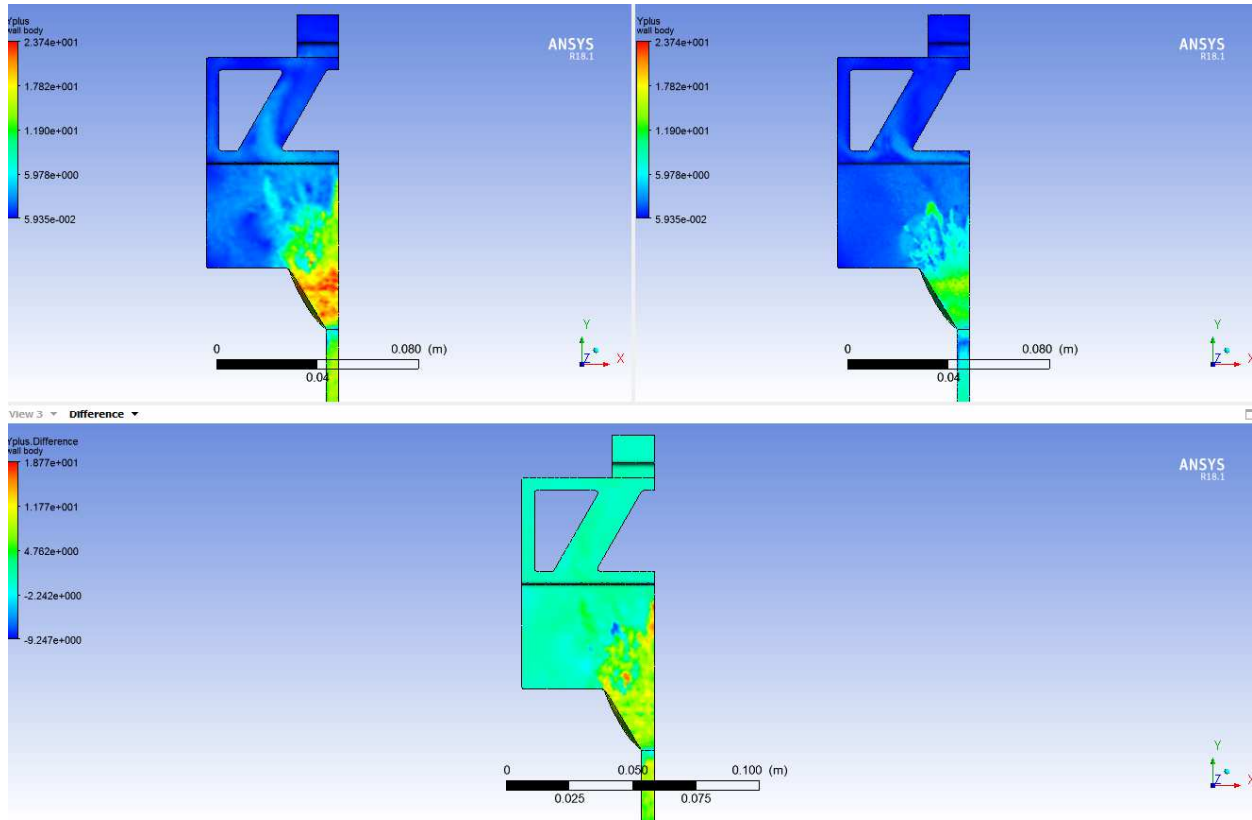


Figure 4.9 Wall y^+ value at $t=0.075$ s for coarse mesh (left), fine mesh (right), and difference between two models (bottom).

Figure 4.10, Figure 4.11 Figure 4.12 show the simulated melt volume fraction at times 0.09 s, 0.12 s and 0.14 s after start of injection for the fine and coarse mesh. The coarse mesh has noticeably less detail at the melt-air interface, and has a slightly different filling pattern, which is best visible at $t=0.14$ s.

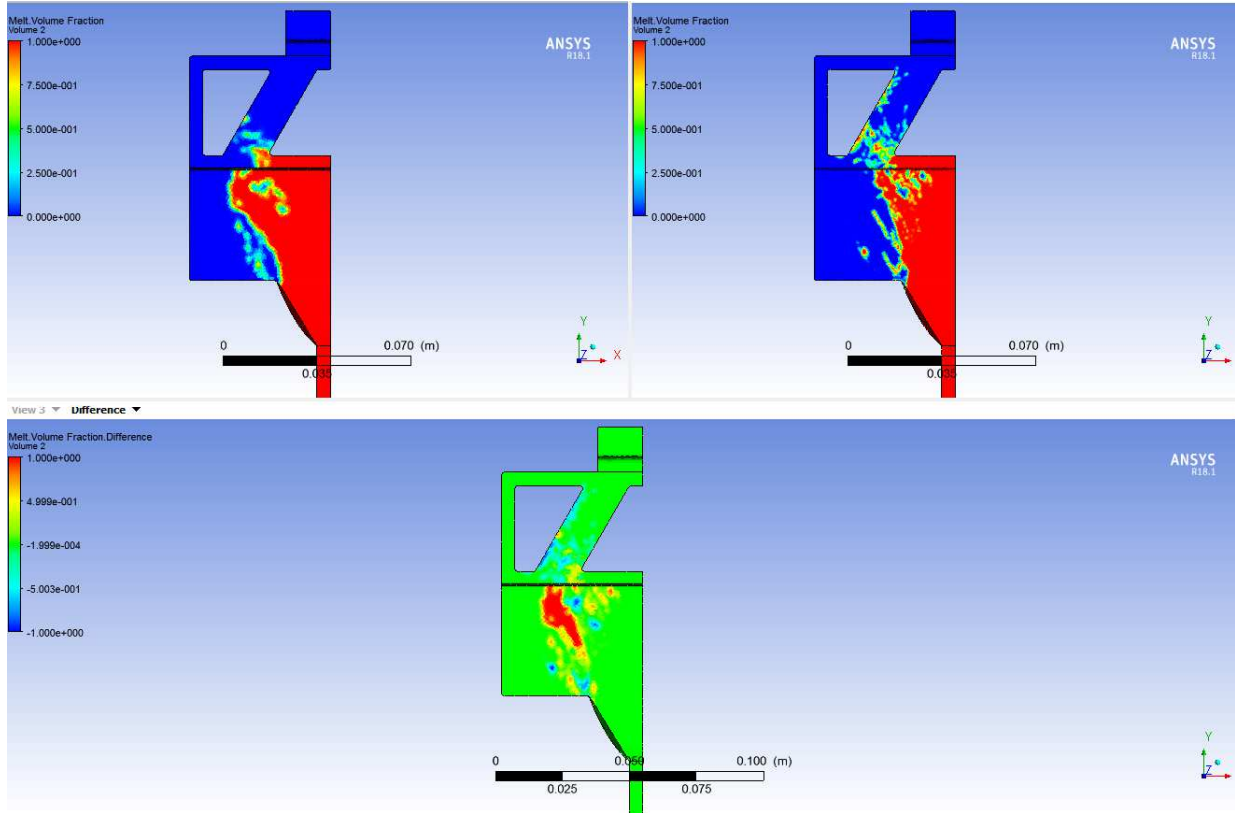


Figure 4.10 Melt volume fraction for coarse mesh (left), fine mesh (right) and difference (bottom) at $t=0.09$ s

The velocity profile in the casting for the fine and coarse mesh is shown in Figure 4.13 and Figure 4.14. The fine mesh appears to capture backflow and vortices in more detail than the coarse mesh.

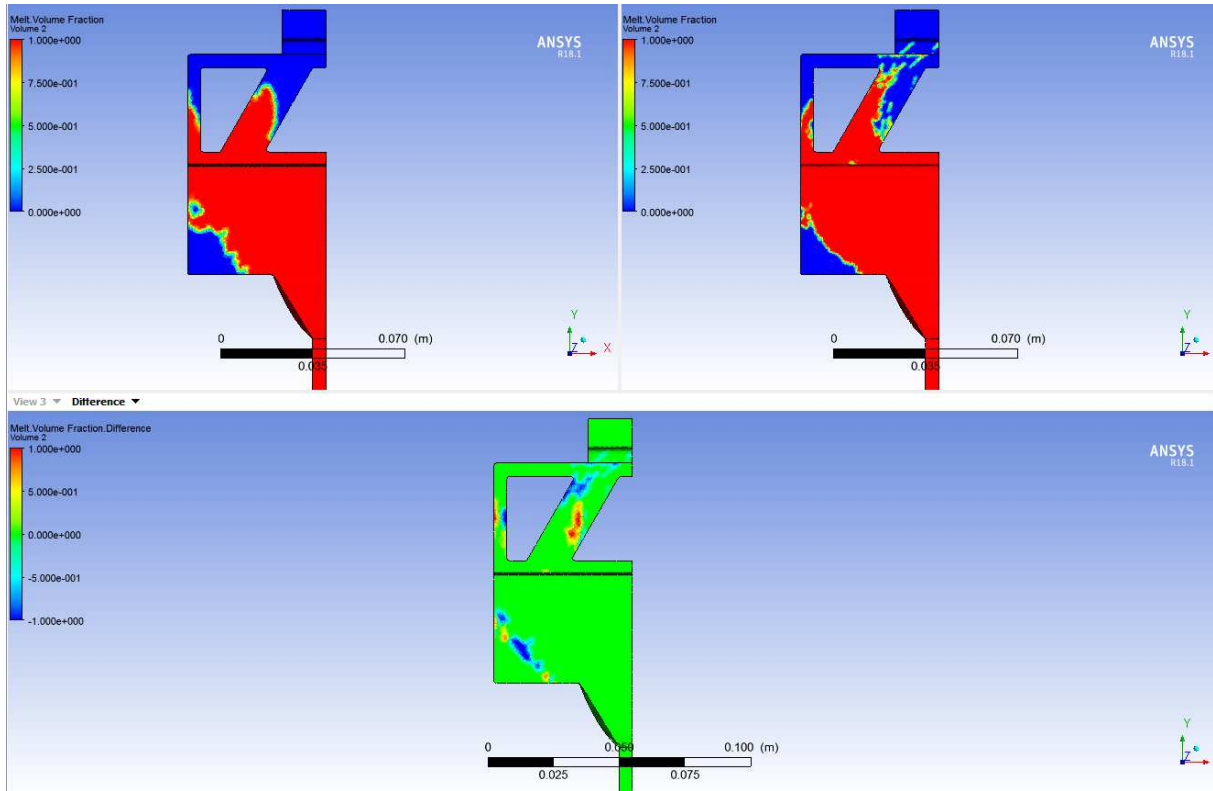


Figure 4.11 Melt volume fraction for coarse mesh (left), fine mesh (right) and difference (bottom) at $t=0.12$ s

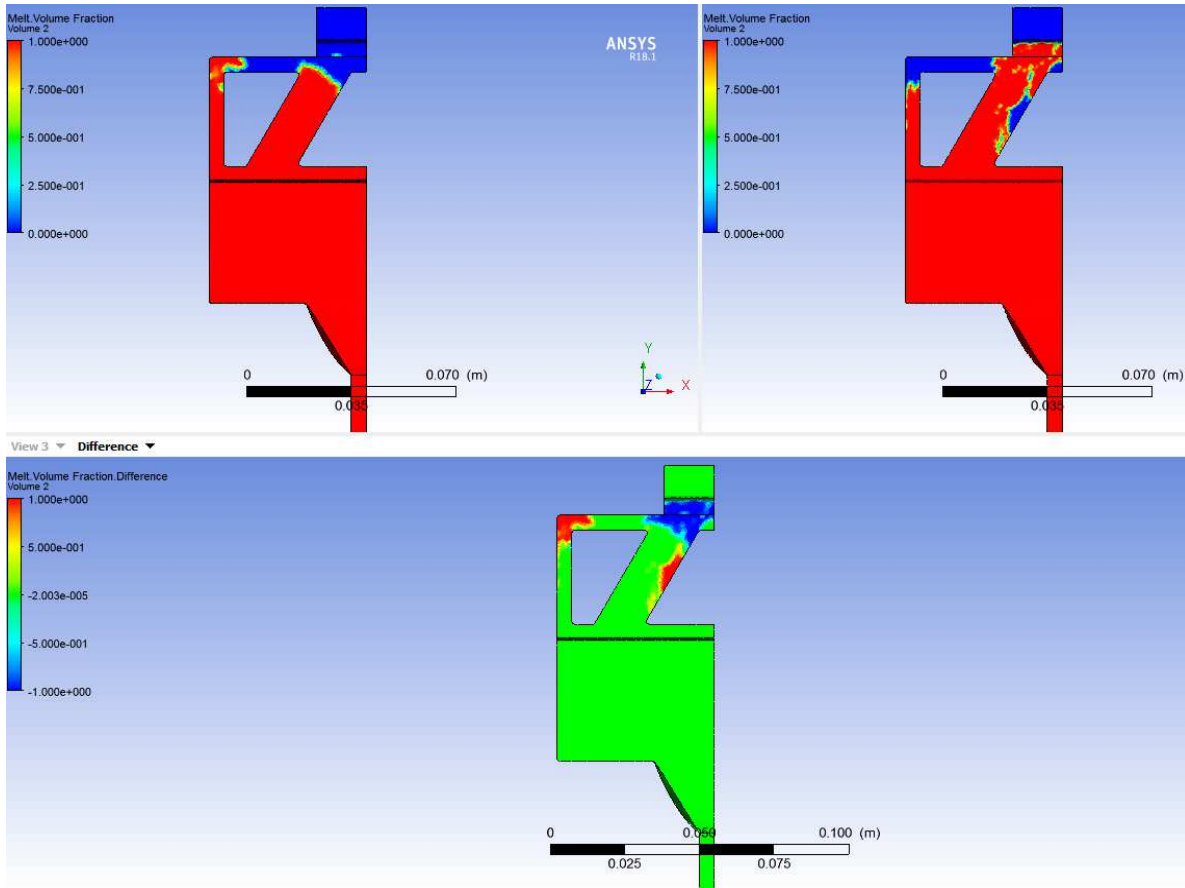


Figure 4.12 Melt volume fraction for coarse mesh (left), fine mesh (right) and difference (bottom) at $t=0.14$ s

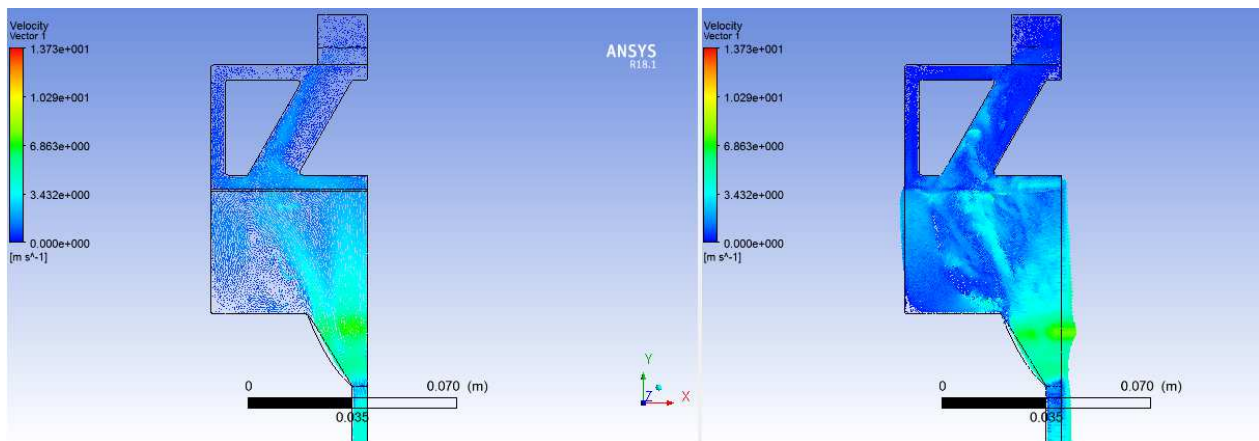


Figure 4.13 Velocity vectors for filling, time-step at 0.09 s

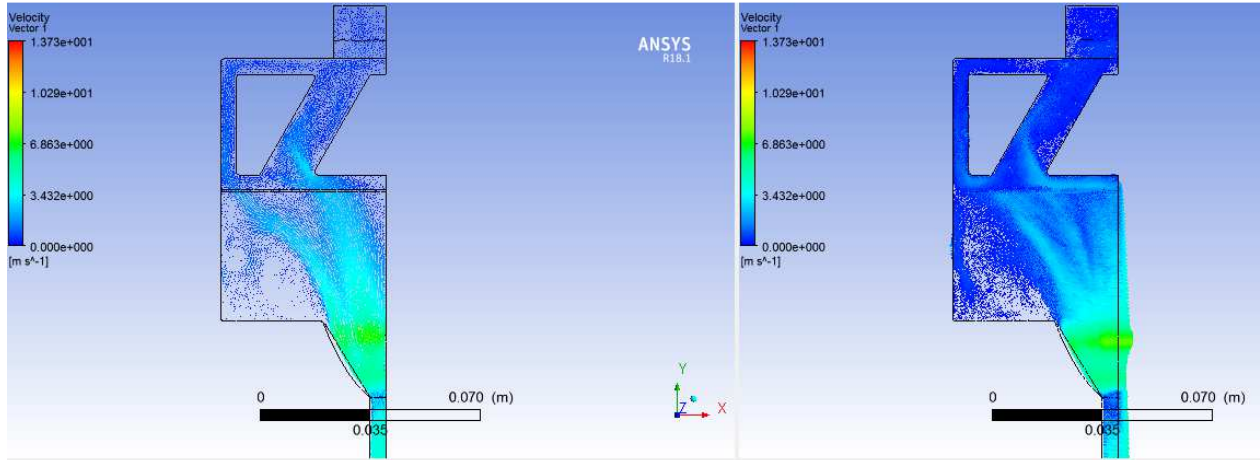


Figure 4.14 Velocity vectors for filling at time-step 0.14 s

4.3.3 Velocity at the gate and rib locations

To find an estimate for the impact pressure at the sensor areas (gate, rib) for AZ91D and Al-9Si-3Cu, cross-sectional average velocities during filling were established at the gate and rib location, where the pressure and temperature sensors were located. The locations are displayed in Figure 4.15. The velocity profile for Al-9Si-3Cu at the gate location is shown in Figure 4.17. The velocity profile for the rib location for Al-9Si-3Cu is shown in Figure 4.17. For further analysis, the average area velocity was determined.

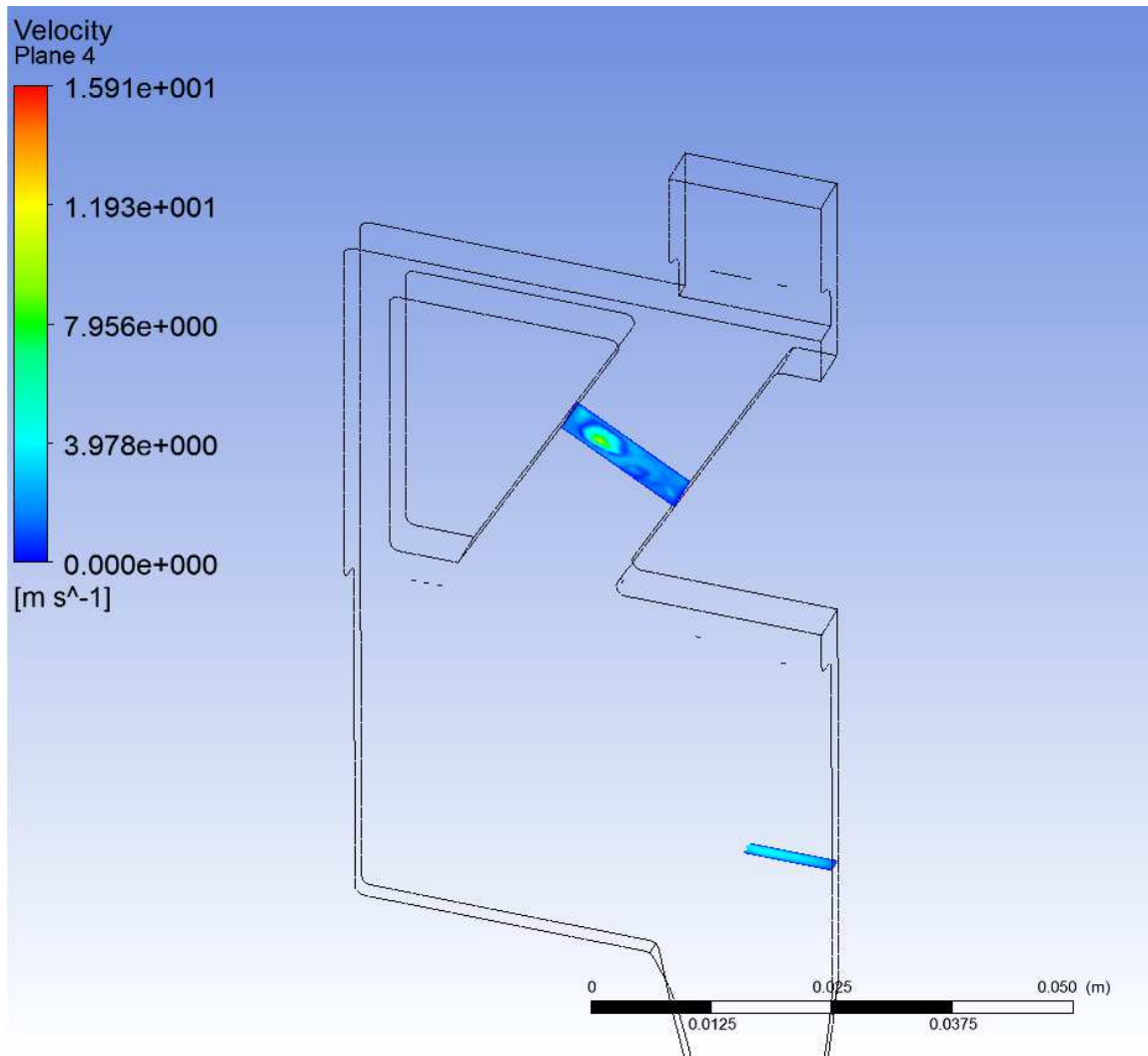


Figure 4.15 Locations for determining velocity profile

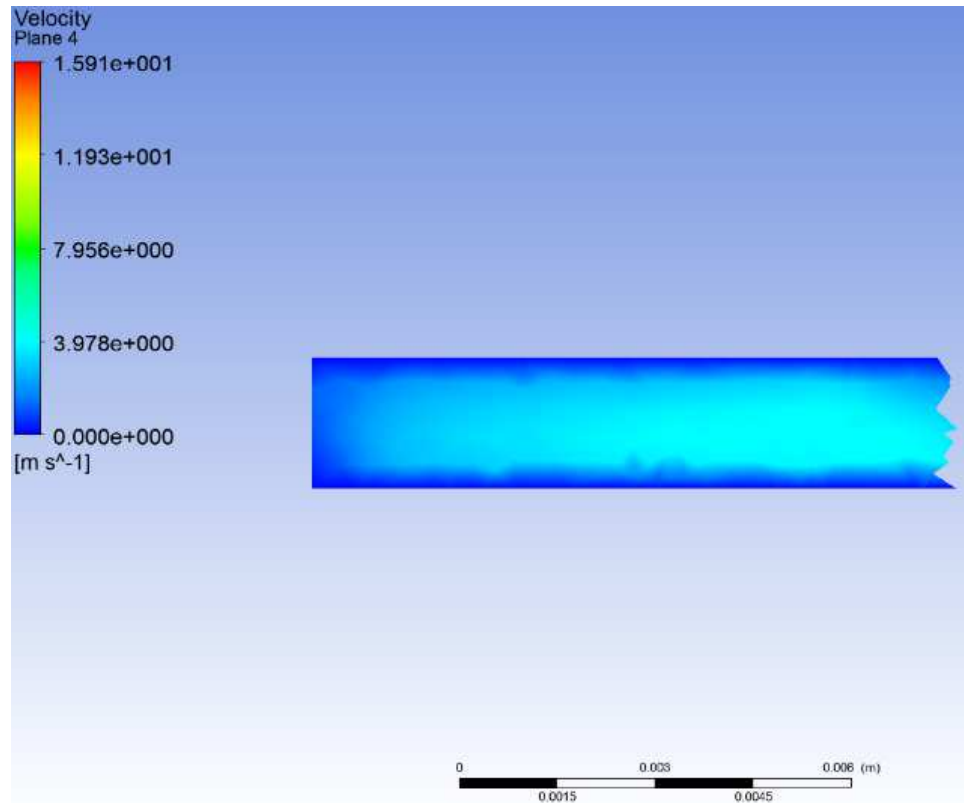


Figure 4.16 Gate velocity profile for Al-9Si-3Cu

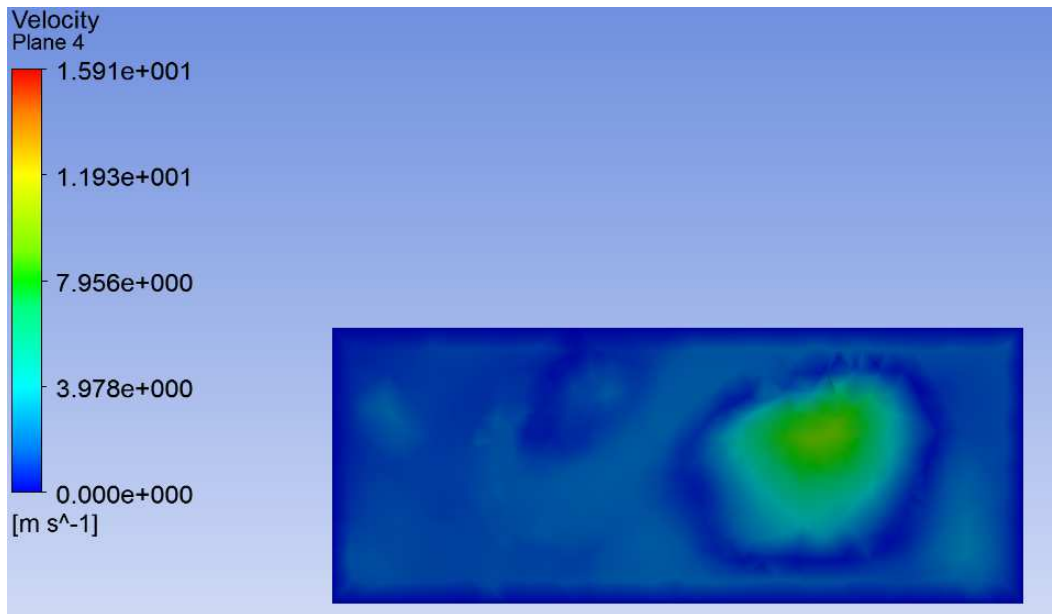


Figure 4.17 Rib velocity profile for Al-9Si-3Cu

4.3.3 Impact pressure and IHTC

The velocity profiles were used to calculate the water hammer pressure. The IHTC was calculated using the Hamasaiid model based on this pressure. The flow velocity was measured at 3 time steps to show that the results are not too sensitive to fluctuation during the die filling. The resulting values for the water hammer pressure, the peak IHTC and the experimental results are shown in Table 4.4 and Table 4.5 for the Al-alloy and Mg-alloy respectively. The impact pressure is used to calculate the initial air gap width, which is used to calculate the peak IHTC according to the Hamasaiid model.

The calculated impact pressures for both alloys are very similar, even though the processing parameters and material parameters are vastly different for the two castings. This is promising, since the experimental peak IHTC is also very similar for the two.

However, the calculated water hammer pressure is too high to give correct results. A fitting constant related to the impact angle was used to scale the pressure. The exact impact angle is difficult to determine from the simulation, but it can be expected to be small, since the flow is mostly lateral to the die surface. The impact pressure of droplets has been shown to be dominated by the surface-normal component of velocity [70]. Therefore we can make the assumption that only the normal component of the flow velocity matters. Instead of using the full value of the water hammer pressure, we adjust it according to the relation:

$$\Delta P_{impact} = \Delta P_{whp} \cdot \sin(\alpha) \quad (\text{Equation 4-14})$$

where α is the impact angle. Using a contact angle of 3.5° , we obtain the correct estimates for IHTC at the gate location. For comparison, the values obtained by Hamasaiid are shown in Table 4.6 and Table 4.7. Finally, a comparison between the two models and experiments can be seen in Figure 4.18.

The results show good agreement at the gate location. At the rib location, the deviation from experiment may be explained by the more complicated filling pattern which makes the impact velocity more difficult to predict. Any differences between our simulated geometry and the actual casting geometry can cause error. Additionally, the flow at the rib location is very turbulent and the average velocity fluctuates significantly, which may introduce errors.

Table 4.4 IHTC for Al-alloy, present study

		Water	Pressure	Initial		
	Velocity	hammer	normal	Air gap	Present	Experimental
		pressure	component	width	study IHTC	peak IHTC
		10^6 Pa	10^6 Pa	10^{-6} m	(W/m ² K)	(W/m ² K)
Gate 0.10 s	2.938	31.7	1.94	0.359	93 000	90 000
Gate 0.11 s	2.911	31.4	1.92	0.360	92 000	90 000
Gate 0.12 s	2.993	32.3	1.97	0.357	94 000	90 000
Rib 0.10 s	1.739	18.8	1.15	0.427	55 000	N/A
Rib 0.11 s	2.048	22.1	1.35	0.405	65 000	N/A
Rib 0.12 s	1.931	20.8	1.27	0.413	61 000	N/A

Table 4.5 IHTC for Mg-alloy, present study

	Velocity (m/s)	Water hammer pressure 10^6 Pa	Pressure normal component 10^6 Pa	Initial Air gap width 10^{-6} m	Present study IHTC (W/m ² K)	Experiment al peak IHTC (W/m ² K)
Gate 0.05 s	5.677	34.5	2.11	0.349	92 000	100 000
Gate 0.06 s	5.453	33.1	2.02	0.354	86 000	100 000
Gate 0.07 s	5.459	33.2	2.03	0.353	86 000	100 000
Rib 0.05 s	1.656	10.0	0.614	0.817	24 000	85 000
Rib 0.06 s	3.336	20.3	1.24	0.416	54 000	85 000
Rib 0.07 s	2.867	17.4	1.06	0.439	46 000	85 000

Table 4.6 IHTC for Al-alloy, Hamasaiid

Impact pressure 10^6 Pa	Adjusted with $0.87 \cdot P_1$ 10^6 Pa	Initial Air gap width 10^{-6} m	Hamasaiid model peak IHTC (W/m ² K)	Experimental peak IHTC (W/m ² K)
26	3.38	0.298	152095	90 000

Table 4.7 IHTC for Mg-alloy, Hamasaiid

Impact pressure 10^6 Pa	Adjusted with $0.87 \cdot P_1$ 10^6 Pa	Initial Air gap width 10^{-6} m	Hamasaiid model peak IHTC (W/m ² K)	Experimental peak IHTC (W/m ² K)
26	3.38	0.298	136154	100 000

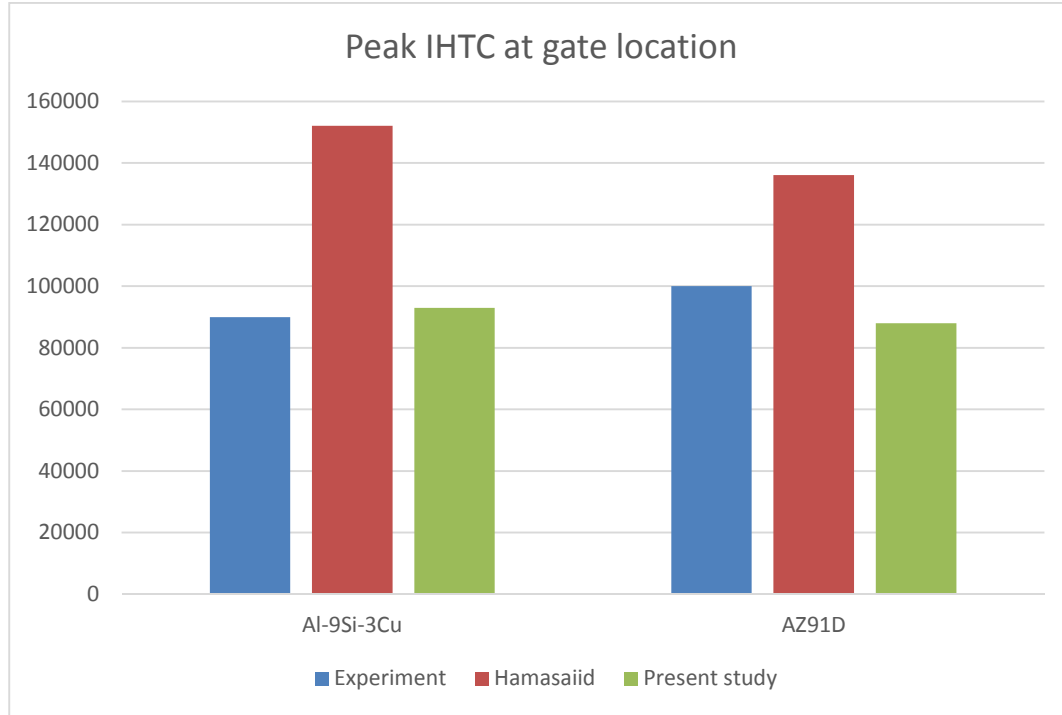


Figure 4.18 IHTC comparison between experiment, Hamasaiid model and present study.

4.4 Evolution of IHTC with time

The second goal of the paper is to create a method to implement the evolution of the IHTC with time in HPDC in a FLUENT simulation. We assume that the air gap between the die and casting grows as a linear function of the fraction of solid of the casting. We assume 1D solidification. This assumption is justified for the gate area, but might not be for the rib area. The geometry for the time evolution simulation is shown in Figure 4.19. The width of the air gap as a function of time is given by:

$$Y = Y_0 + c_0 f_s(t) \quad (\text{Equation 4-15})$$

where c_0 is a fitting constant, Y_0 is the initial air gap width, and f_s is the solid fraction of the fluid domain. The fraction of solid is calculated using an equilibrium solidification model in FLUENT. The script files required to run the simulation are included in Appendix A-F. The flowchart in Figure 4.20 details how to setup and run the simulation.

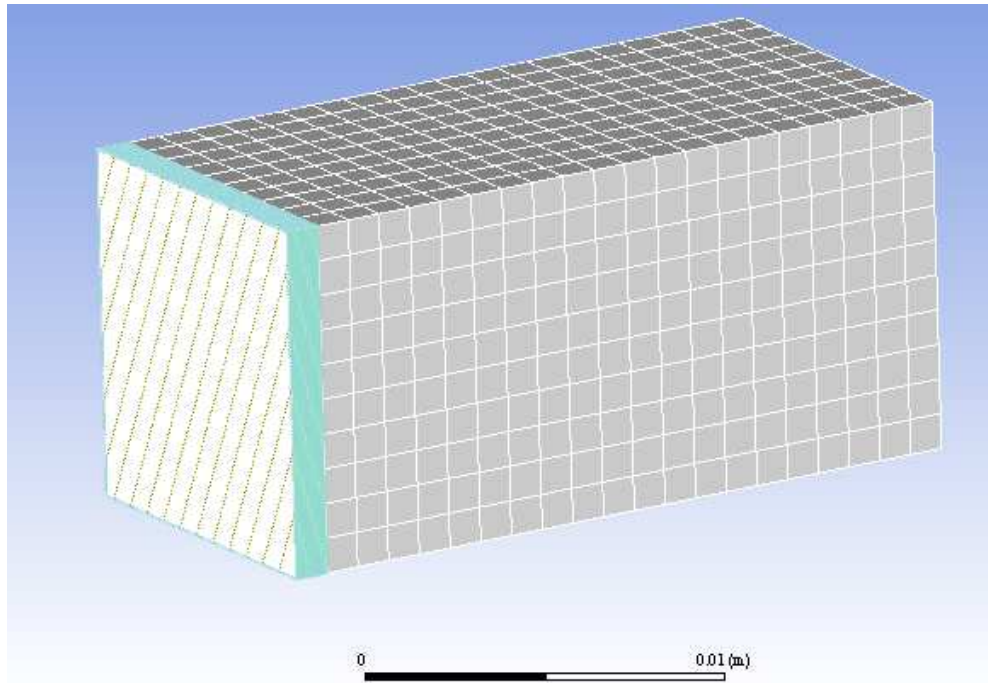


Figure 4.19 Geometry for IHTC evolution simulation. The casting half-thickness mesh is shown in teal and die mesh in grey.

A c_0 value of $1e-7$ was found to fit both the Aluminum and Mg-alloy. The results are shown in Figure 4.21 and Figure 4.22 with blue dots indicating experimental results, and the red line indicating simulation results. However, both the present study and the model by Hamasaiid ignore the effect of fluid flow on the IHTC. With a Nusselt number of 1, this may cause severe errors. Future work should aim to validate this model while taking into account fluid flow in the FLUENT simulation during the die-filling timeframe.

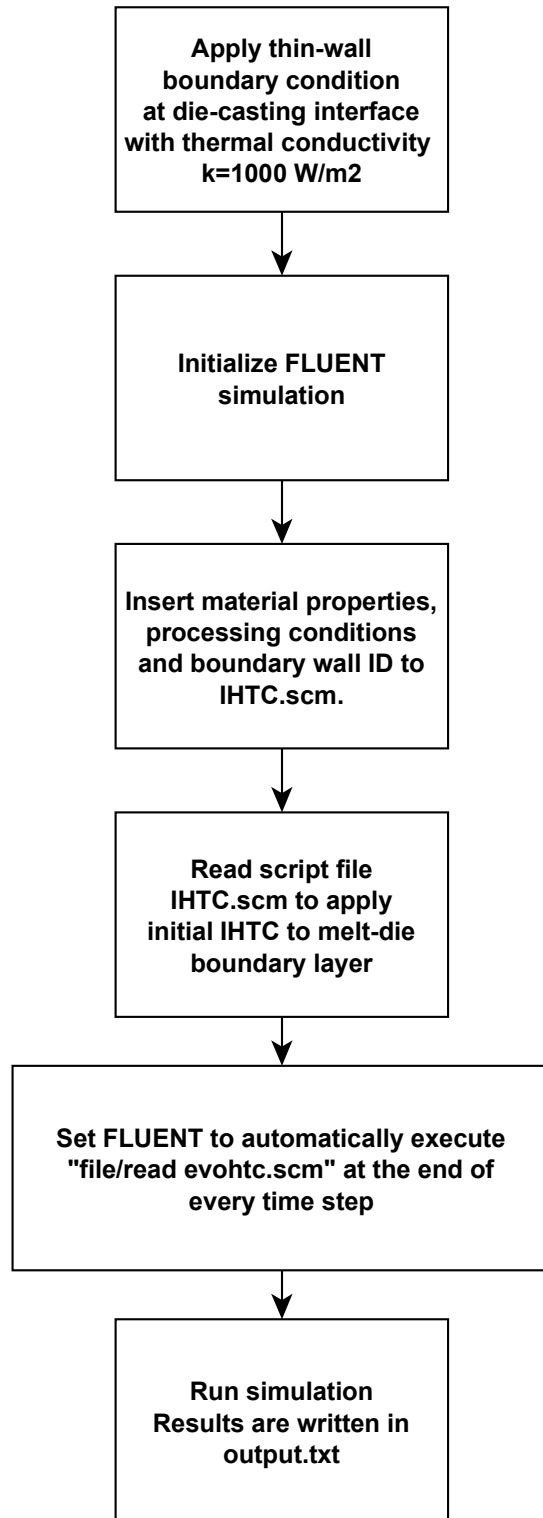


Figure 4.20 Flowchart for time-evolution simulation of IHTC

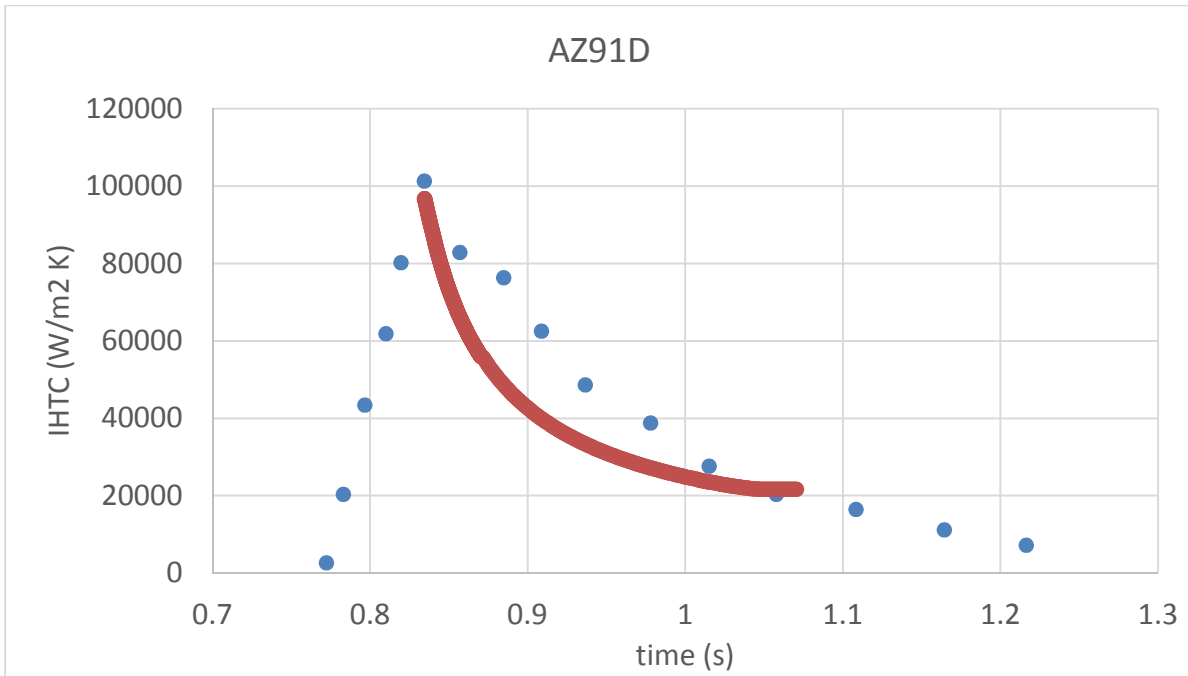


Figure 4.21 time evolution of modelled IHTC (red) vs experiment (blue) for Mg-alloy

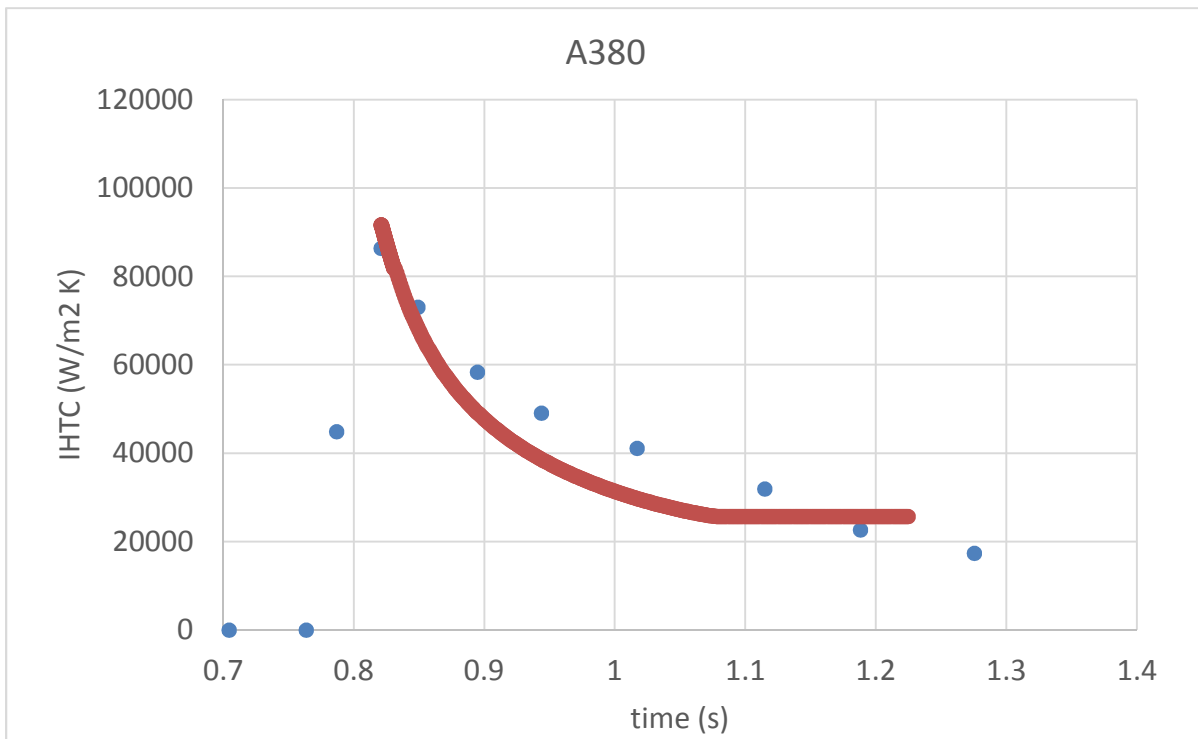


Figure 4.22 time evolution of modelled IHTC (red) vs experiment (blue) for Al-alloy

4.5 Conclusions

- 1) The IHTC model by Hamasaiid et al. was found to contain an unrealistic empirical capillary pressure term.
- 2) The impact pressure was predicted using the “water hammer pressure” model. The IHTC values for both Mg and Al alloys matched experimental results very well, when this pressure model was used with the addition of a scalar scaling factor. This is promising, because the material properties and casting conditions for both alloys were very different.
- 3) A model for the time-evolution of the IHTC was developed and implemented in FLUENT 18.1 using .scm script files and UDF-files. Modelling the air gap evolution as a linear function of fraction of solid gave moderately good results. The same fitting constant could be used for both the Mg and Al alloy

CHAPTER 5 – SOLIDIFICATION KINETICS OF FE-RICH INTERMETALLICS

5.1 Introduction

High-pressure die-cast of Al-alloys usually add Fe (1-2%) to reduce soldering of metal to die. However, as an unwanted side-effect, brittle iron-rich intermetallics are formed. The most common morphology of Fe-rich intermetallics in HPDC A383 is the polyhedral α - $\text{Al}_{15}(\text{Fe},\text{Mn},\text{Cr})_3\text{Si}_2$, shown in Figure 5.1.

These particles follow a bimodal size distribution. This is caused by two different particle growth mechanisms. Some particles nucleate in the holding tank before the casting takes place. The growth of these particles is not limited by diffusion, but instead by the low driving force for growth at high temperature. These particles grow up to large sizes. [71]

Other particles nucleate interdendritically during the casting, where the segregation of Fe and the lower temperature provides a greater driving force for phase transformation. However, their growth is limited by impingement on the primary or eutectic phase, and possibly also by the diffusion rate of Fe from the bulk to the liquid-intermetallic interface. The goal of the present study is to model the latter growth mechanism.

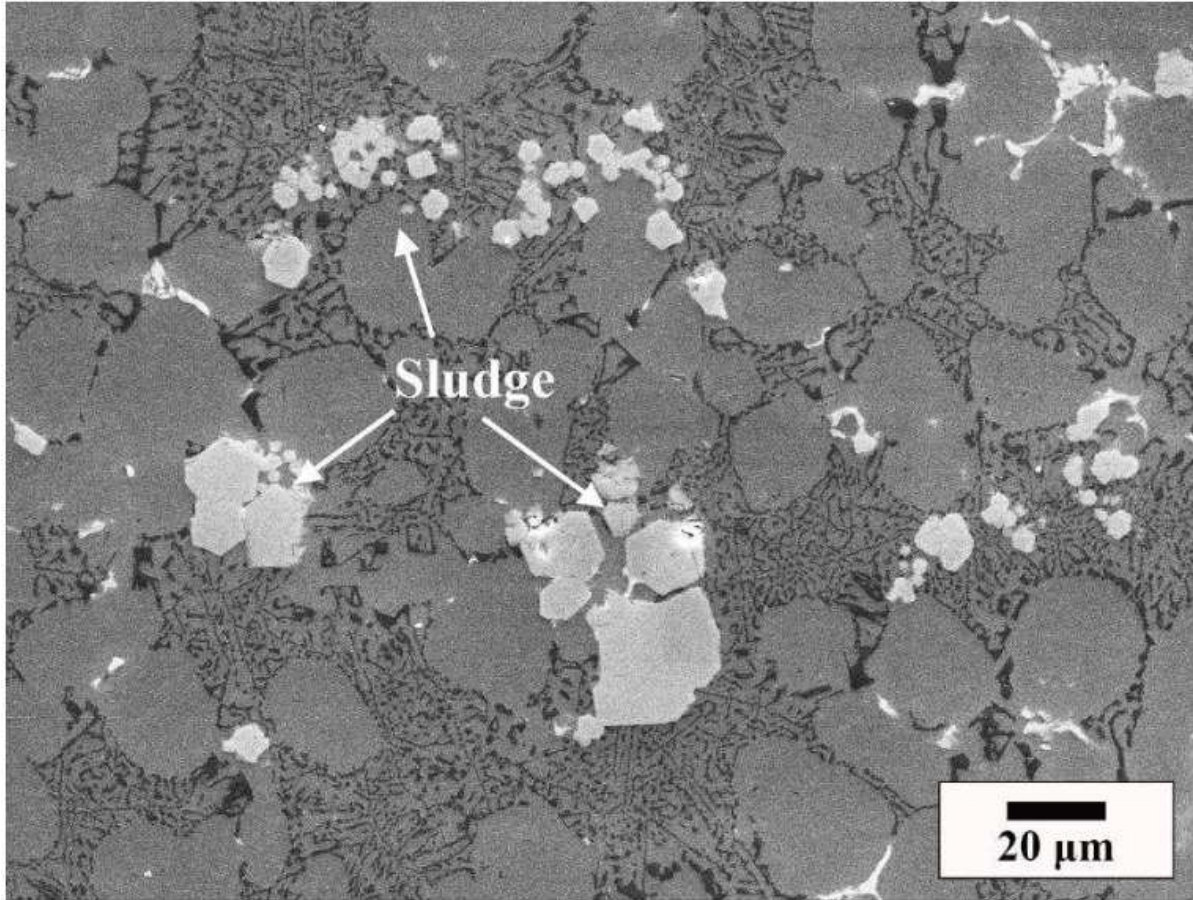


Figure 5.1 Polyhedral α -Fe intermetallic (“sludge”) [36]

We introduce a method to predict the average diameter of the interdendritic α -Fe intermetallics in A383 using the diffusion-controlled growth model by Nastac [72] combined with solidification simulations using the commercial casting simulation software NOVASOLID&FLOW. We validate our predictions using image analysis of optical micrographs of various cross-sections of the casting. The strategy of the study is shown in Figure 5.2.

α -Fe intermetallics have a BCC crystal structure, and exhibit faceted growth. The terminal faces of polyhedral α -Fe intermetallic particles belong to plane $\{110\}$, with 120° or 60° degree angles between faces. When viewed from the 111 direction, particles appear hexagonal. [73] These findings have led us to believe that the Fe-rich intermetallic has a rhombic

dodecahedron 3D-shape. [74] This observation is supported by SEM-analysis of deep-etched α -Fe intermetallic morphology in AlSi9Cu3Fe-alloys. [71]

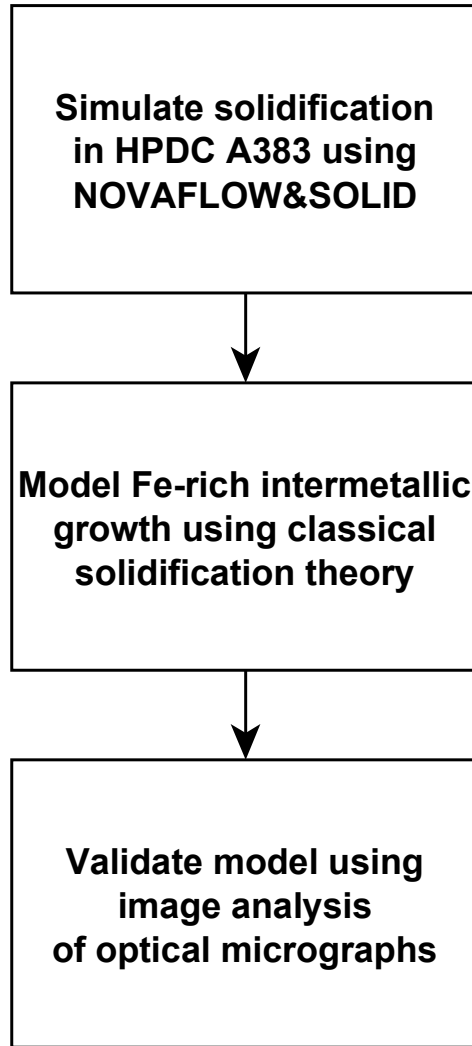


Figure 5.2 Strategy for α -Fe intermetallic growth study.

5.2 Mathematical models

We use the Scheil equation to model the evolution of the Fe-concentration in the casting during solidification:

$$C_l = C_0(1 - f_s)^{k-1} \quad (\text{Equation 5-1})$$

where C_0 is the bulk liquid concentration, f_s is the solid fraction, and k is the partition coefficient. This model has two major assumptions:

- Diffusion in liquid is infinitely fast.
- Diffusion in solid does not take place.

For the first assumption to be valid, the liquid diffusion must be faster than the particle growth velocity, otherwise we will overestimate growth. The second assumption is valid, if the solid diffusivity of Fe is significantly slower than liquid Fe diffusivity. The orders of magnitude for liquid and solid diffusivity of Fe in Al are $1e-9$ and $1e-18$ respectively, which justifies this assumption. [75]

For volume-diffusion limited growth, growth velocity of a particle is given by:

$$v_\alpha = \Omega_C \frac{D_L}{R_D - R_\alpha} \quad (\text{Equation 5-2})$$

where D_L is the liquid diffusivity, R_D is the radius of the micro-volume element, R_α is the radius of the intermetallic particle, and Ω_C is the solutal supersaturation. The use of (Equation 5-2) requires the assumption, that diffusion is the rate-limiting factor for intermetallic growth, instead of the rate of chemical reaction for formation of α -Fe. To ascertain this, the Gibbs formation

energy of α -Fe should be known as a function of temperature. Unfortunately, to the author's knowledge, no such studies have been carried out to date.

Solutal supersaturation is given by the equation:

$$\Omega_C = \frac{\langle C \rangle_l - C_l^*}{C_\alpha^* - C_l^*} \quad (\text{Equation 5-3})$$

where C_l^* is the liquid interface concentration, C_α^* is the interface concentration for α -Fe, and $\langle C \rangle_l$ is the average liquid concentration.

The volume of the microelement is given by:

$$R_D = \frac{3}{4\pi} \left(\frac{V_L}{N_\alpha} \right)^{1/3} \quad (\text{Equation 5-4})$$

where V_L is the volume of liquid in the solidification envelope, and N_α is the number of α -Fe nuclei in that volume.

Our model assumes that the α -Fe particles are spherical. To check the validity of this assumption, we can compare the statistical diameter distribution of spheres and rhombic dodecahedrons using the approach and data from Danilenko et al. [76]. The results shown in Figure 5.3 indicate that the match is adequate for all but the 10% largest and smallest diameters.

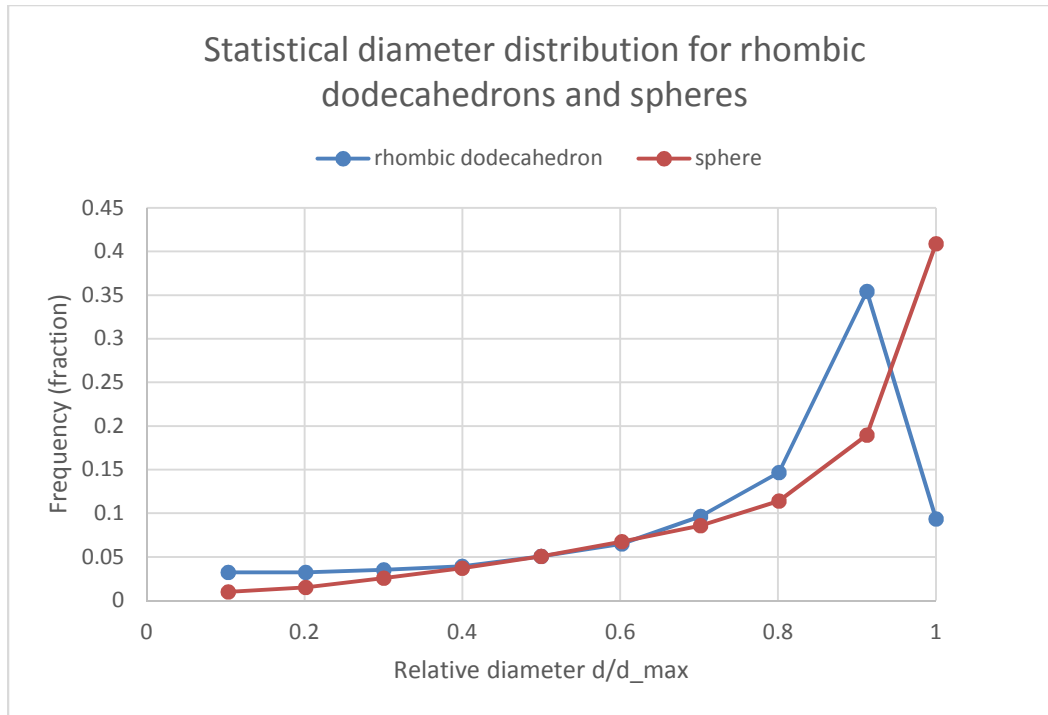


Figure 5.3 Comparison between statistical distribution of cross-sections of diameters for spheres and rhombic dodecahedrons.

5.3 Predicting cooling rate in HPDC A383

Casting simulations were carried out in NOVAFLOW&SOLID to determine the time-evolution of temperature and solid fraction in the casting. To validate the simulation, the predicted temperature of the die surface at 6 distinct locations was compared with FLIR thermal camera measurements taken after removal of the casting. These locations are shown in Figure 5.4 alongside the temperature profile of the die surface. These measurements were carried out at two different stages of the casting cycle: before the application of water sprays, and after the application of water sprays. The measured temperature values are shown in Table 5.1. The letter A and B stand for measurements taken before the spray and after the spray respectively. The numbers 1-6 indicate the location of the measurement.

The NOVAFLOW&SOLID model contains subroutines for air gap evolution, water sprays and cycling. However, in the scope of this study, it was not possible to experimentally determine the correct parameters for these models, so we had to rely on parameter fitting.

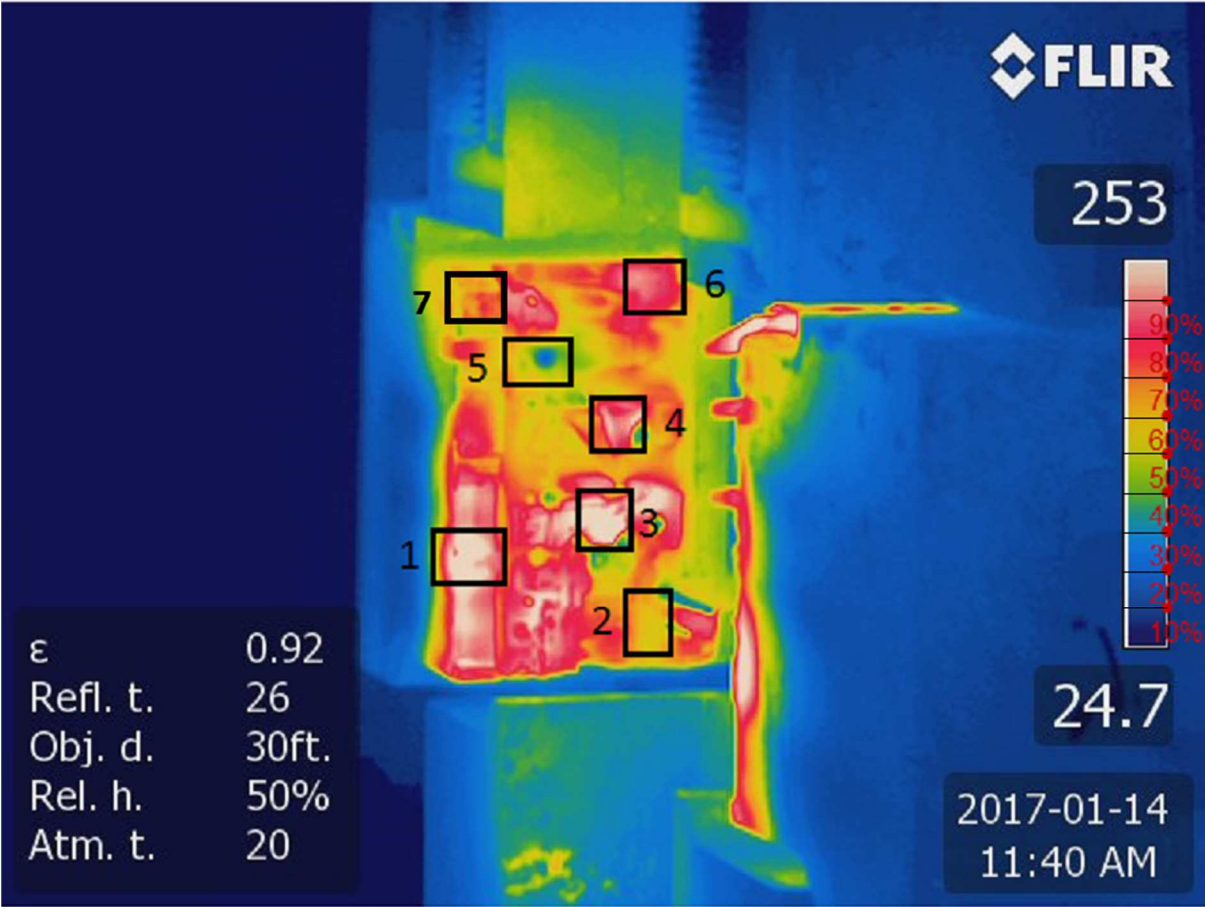


Figure 5.4 FLIR temperature measurement of Die-surface after casting

Table 5.1 FLIR temperature measurements

	1	2	3	4	5	6	7	8	9	10	Average
A1	334	334	314	313	339	318	322	318	322	320	323
B1	264	261	270	270	265	266	271	266	276	274	268
A2	175	175	179	179	157	187	189	187	188	186	180
B2	165	163	166	167	167	180	184	180	185	171	173
A3	334	335	348	346	339	318	322	318	322	320	330
B3	264	261	270	270	265	266	271	266	276	261	267
A4	334	334	348	346	339	318	322	318	322	320	330
B4	264	261	270	270	265	266	271	266	276	261	267
A5	112	112	112	112	124	121	123	121	105	119	116
B5	91	90	88	90	85	95	97	95	82	94	91
A6	271	271	280	279	273	285	289	285	289	286	281
B6	215	212	218	218	188	193	197	193	198	197	203

4 parameters were chosen to be varied for the fitting process:

- The die-air contact temperature
- Maximum air gap width
- Temperature of air gap formation
- Cooling channel water flow

To minimize the amount of simulations needed to establish the correct fitting parameter values, we used orthogonal array testing (Taguchi method) [77] [78]. Orthogonal array testing provides a systematic way to estimate the effect of multiple independent variables on the

outcome of a process. It is a less robust approach than ANOVA (analysis of variance), but significantly faster. In orthogonal array testing, the user chooses a set number of independent variables and a set number of levels for each variable. The method then provides the user with the least number of trials required to test each pairwise combination of each variable level. For our case, we chose 3 levels for each variable. The resulting set of trials is shown in Table 5.2.

By analyzing the simulations, we could establish the relative significance of each parameter on the temperature evolution of locations 1-6. These results are shown in Figure 5.5 and Figure 5.6. The maximum air gap width parameter is the most significant, followed by cooling channel water flow and the air gap formation temperature. The effect of air temperature is insignificant.

Table 5.2 Values of optimization parameters

Trial	Contact gap (μm)	Air gap formation temperature ($^{\circ}\text{C}$)	Cooling channel water flow multiplier	Air inside die temperature ($^{\circ}\text{C}$)
1	100	440	1x	150
2	100	480	3x	200
3	100	520	5x	250
4	200	440	3x	250
5	200	480	5x	150
6	200	520	1x	200
7	300	440	5x	200
8	300	480	1x	250
9	300	520	3x	150

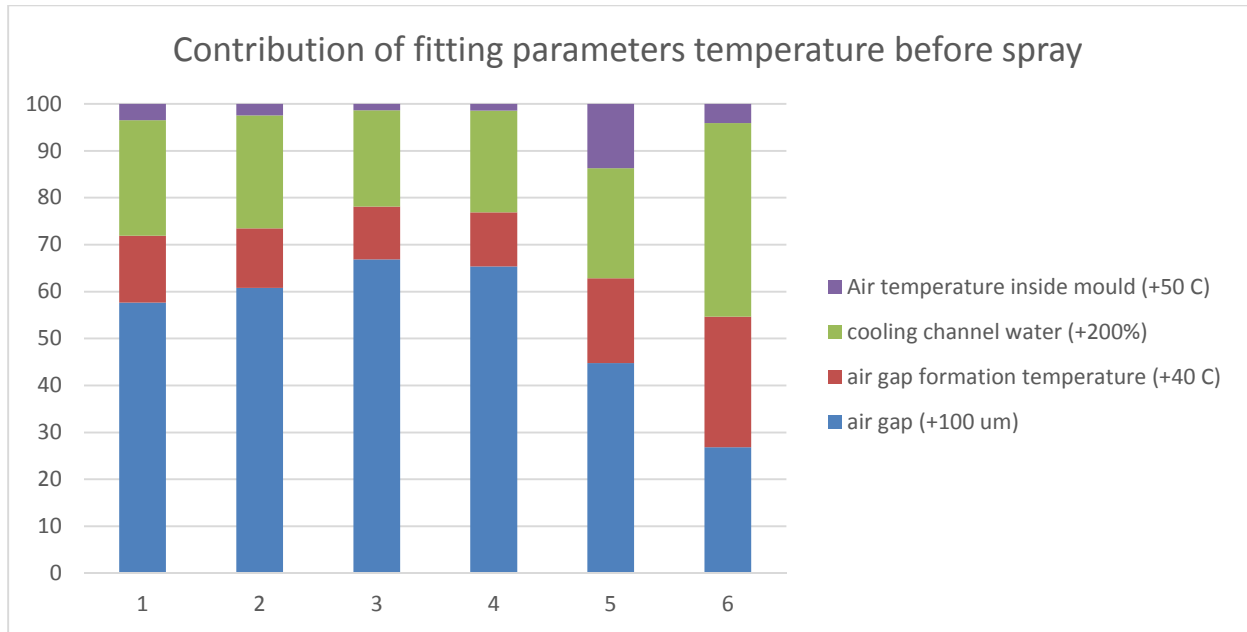


Figure 5.5 Relative effect of varying fitting parameters to temperatures at locations 1-6 before water spray.

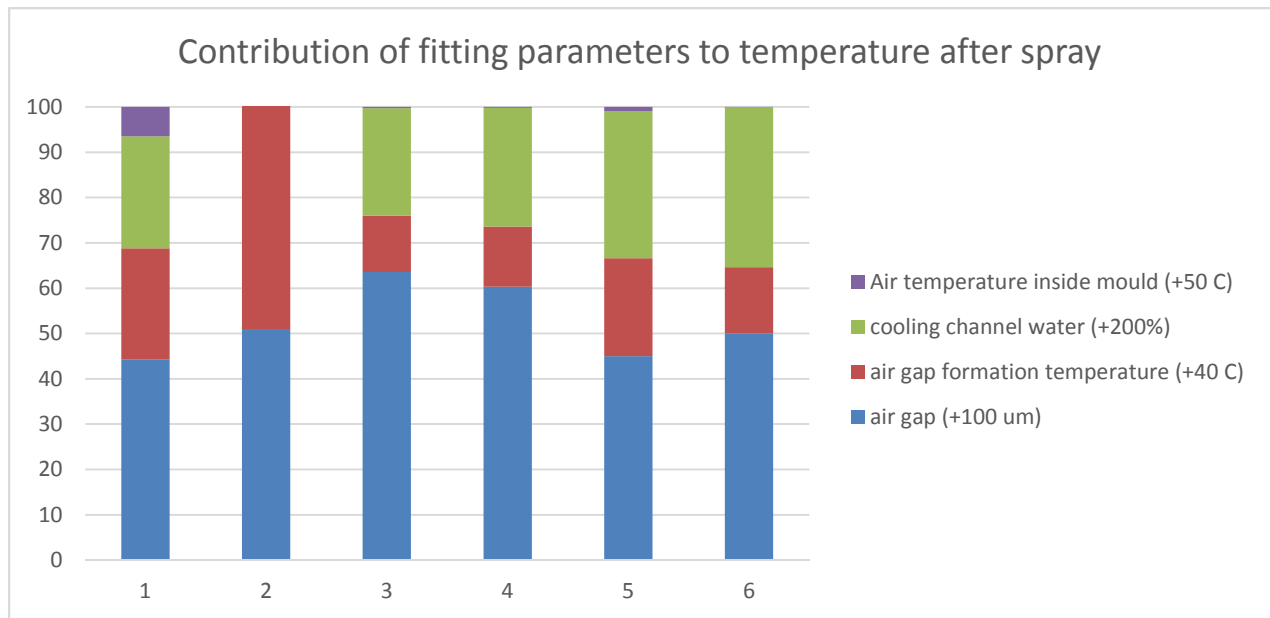


Figure 5.6 Relative effect of varying fitting parameters to temperatures at locations 1-6 after water spray.

To determine which trial provided us with the best results, the temperature evolution at locations 1-6 was compared with the experimental results. It was found that trial 9 gave the best results. The comparison between the average experimental temperature measurements and simulated temperature evolution for trial 9 at locations 1-6 is shown in Figure 5.7, Figure 5.8, Figure 5.9, Figure 5.10, Figure 5.11 and Figure 5.12. At some locations, the die surface temperature drops sharply immediately after the removal of the casting. The FLIR measurements are taken after a small delay after the opening of the die, which explains why the measurements do not match the peak temperature in the simulation, but rather the temperatures after this rapid drop.

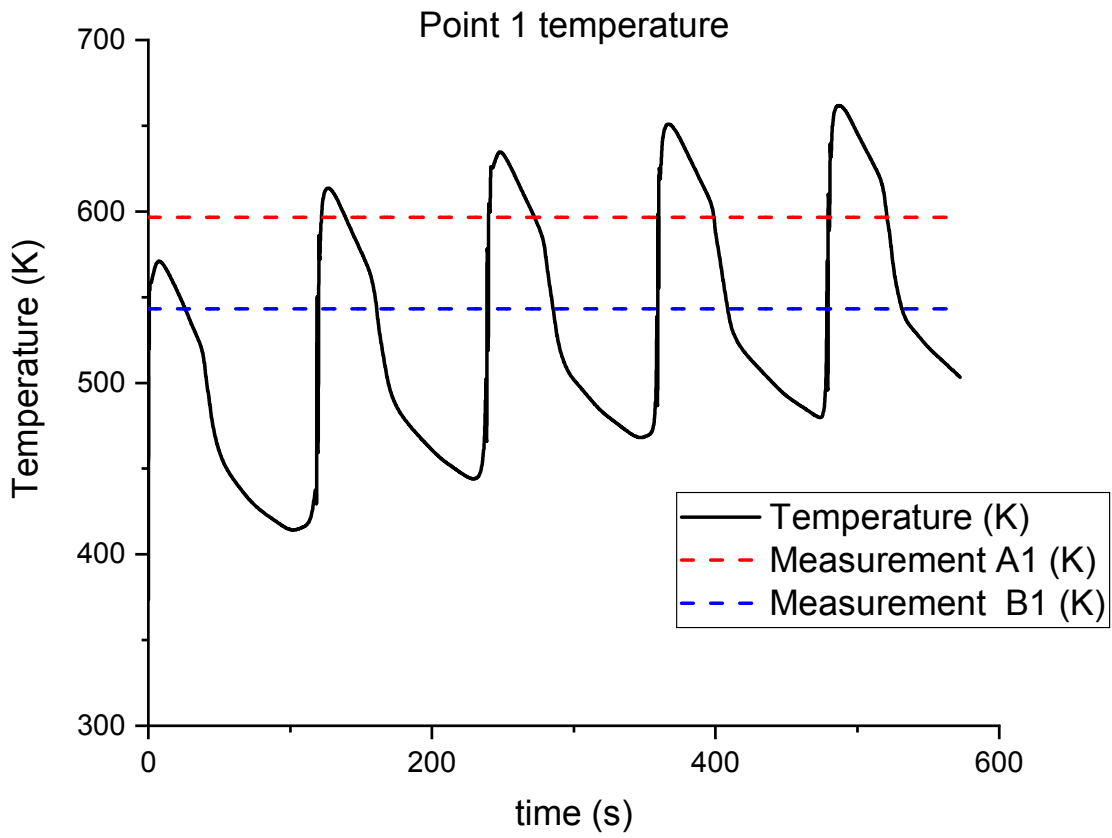


Figure 5.7 Trial 9 temperature evolution at location 1 compared with experimental measurements.

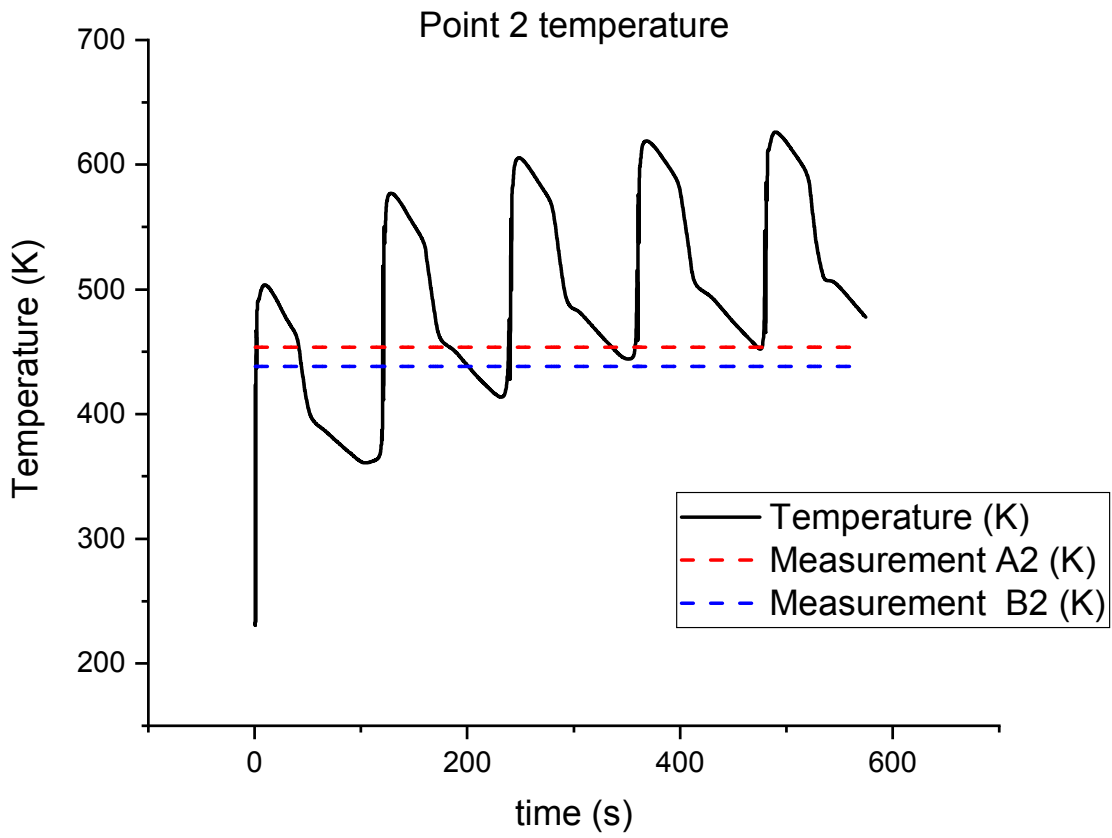


Figure 5.8 Trial 9 temperature evolution at location 2 compared with experimental measurements.

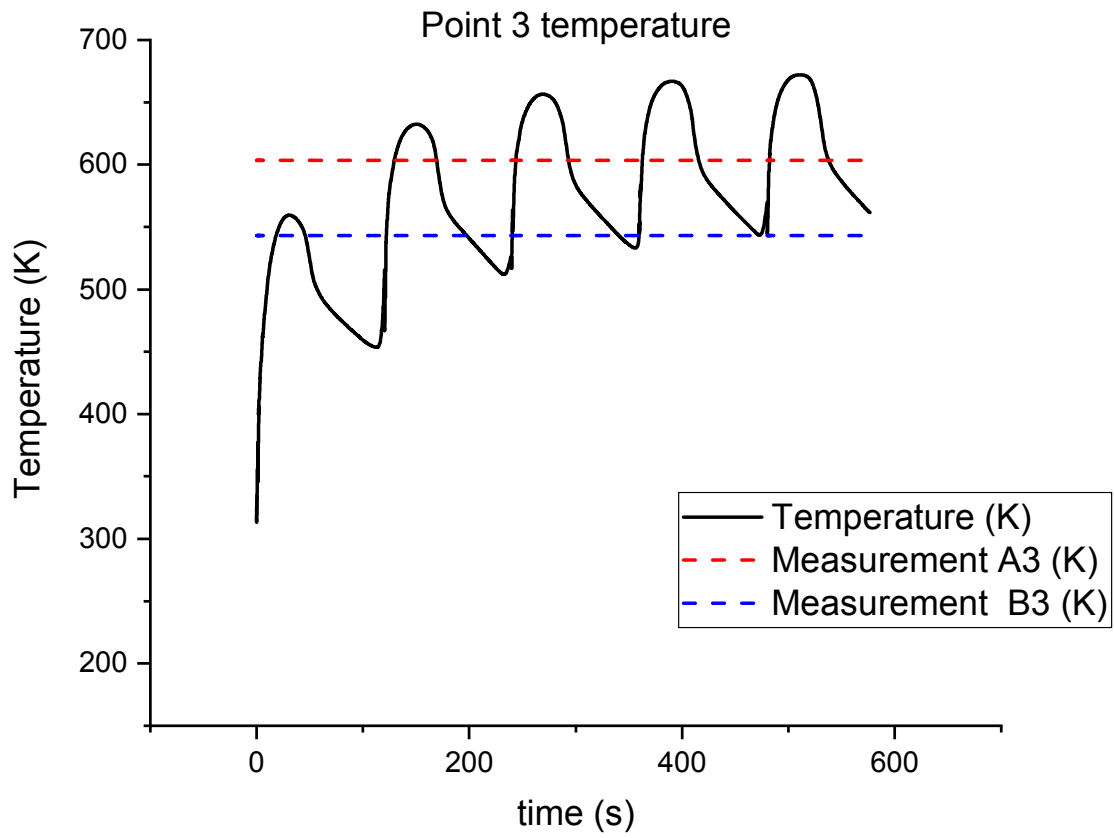


Figure 5.9 Trial 9 temperature evolution at location 3 compared with experimental measurements.

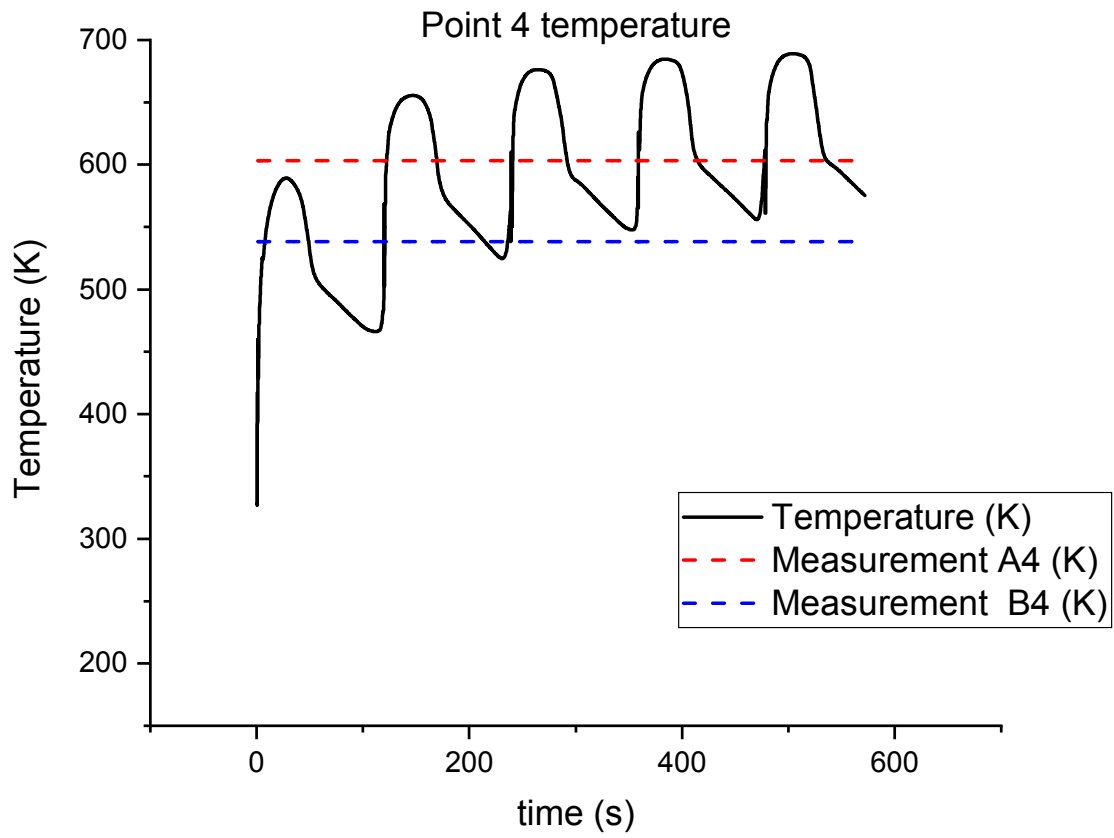


Figure 5.10 Trial 9 temperature evolution at location 4 compared with experimental measurements.

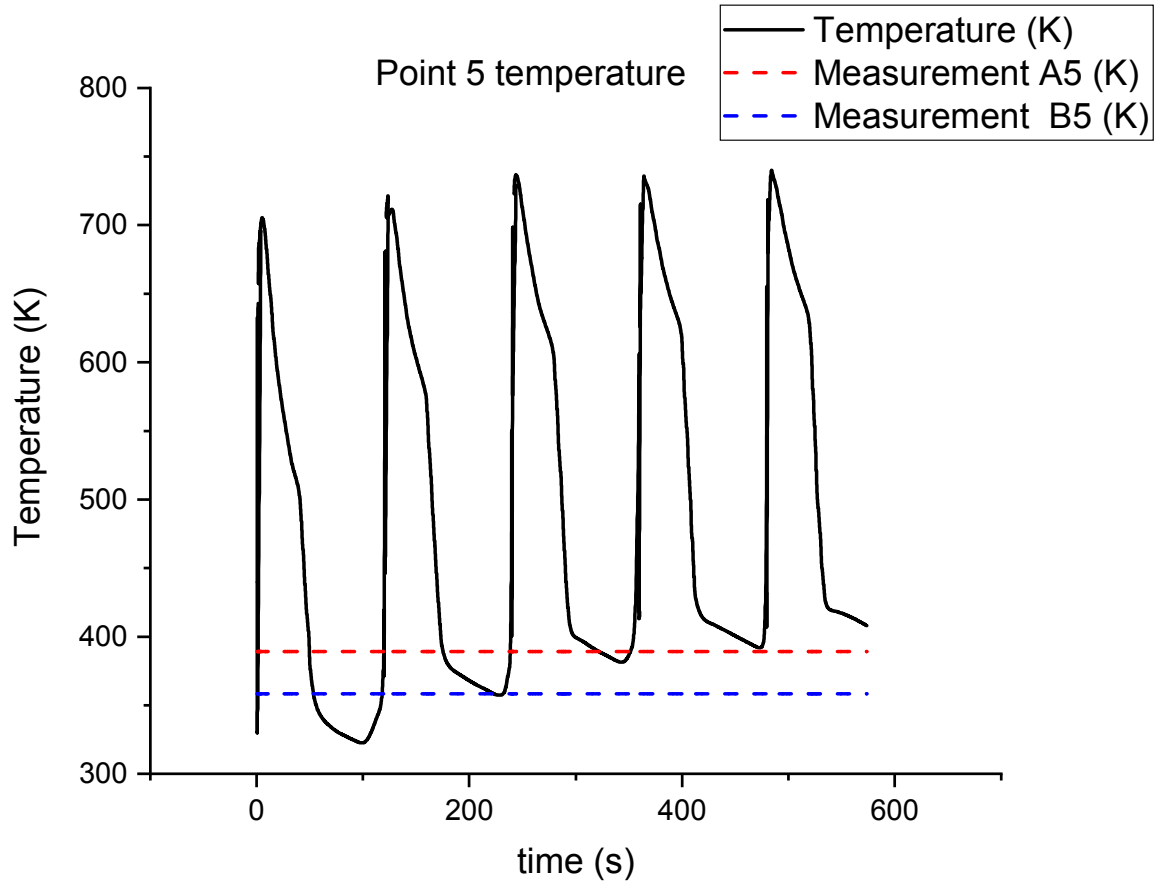


Figure 5.11 Trial 9 temperature evolution at location 5 compared with experimental measurements.

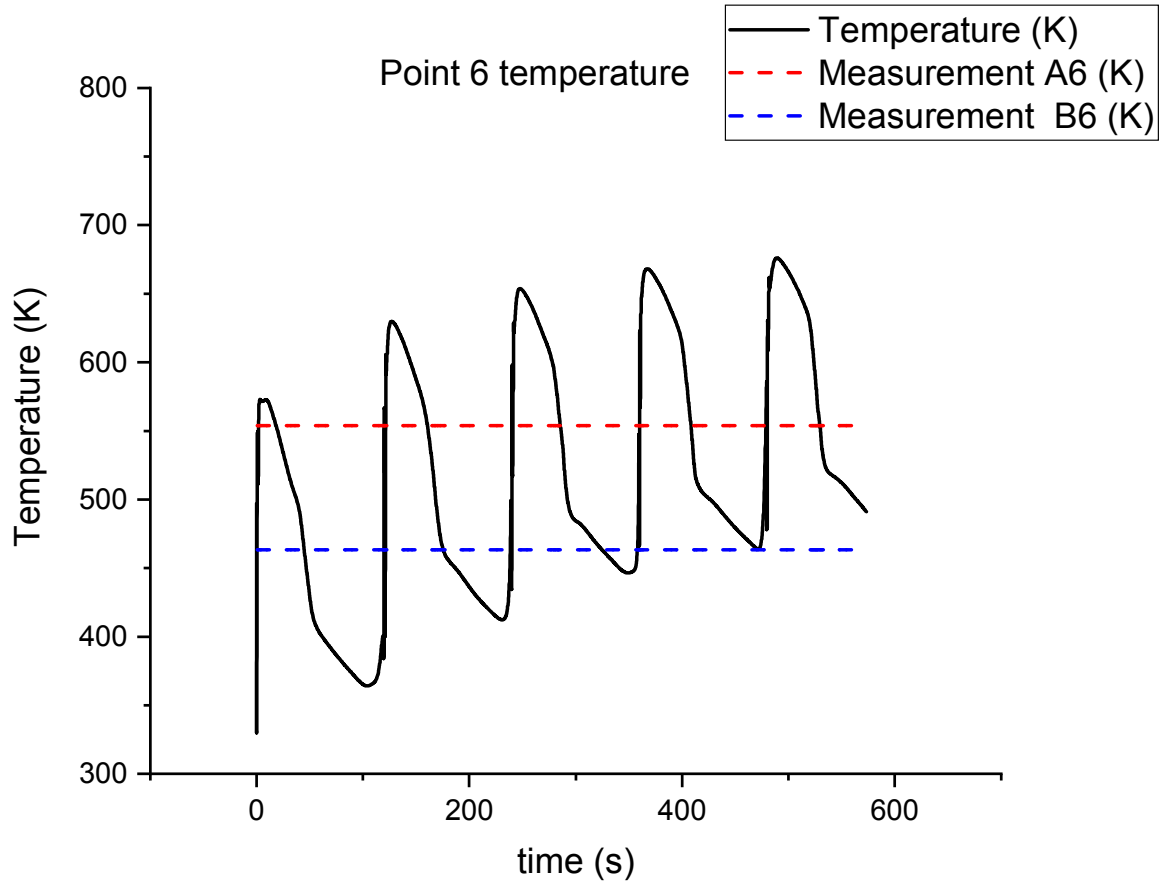


Figure 5.12 Trial 9 temperature evolution at location 6 compared with experimental measurements.

5.4 Methods

5.4.1 Experimental methods

An as-cast A383 engine block was cut, and 5 samples were obtained for image analysis. The samples 1,2,3 correspond to the front, center and rear of the bulkhead respectively. The location of the samples is shown in Figure 5.13.

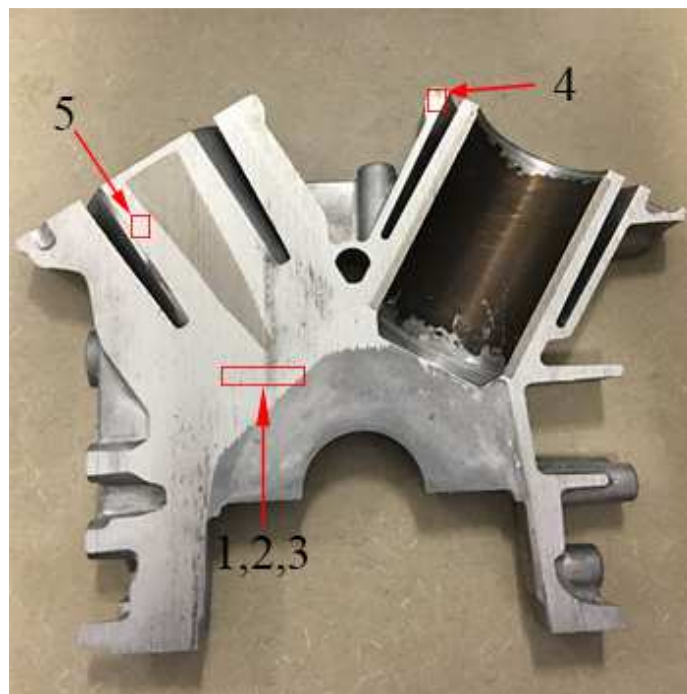


Figure 5.13 Location of samples for sludge size measurements

The area of each α -Fe intermetallic particle in 3 micrograph from each sample was measured using Photoshop. Unfortunately, there were too few measurements available from sample 2 to make a statistically relevant determination of intermetallic size, so it was ignored. Figure 5.14 shows a micrograph taken from sample 1, the front of the bulkhead. The α -Fe intermetallic phase is visible as light grey. The dark grey phase is eutectic silicon. The white

phase is primary or eutectic aluminum. Figure 5.15 shows an optical micrograph taken from sample 5. Due to the higher cooling rate, the microstructure is finer, and silicon and sludge particles exhibit higher circularity.

The α -Fe intermetallic diameter distribution was calculated from the measurements using the open source Python script GrainSizeTools. We used the app to calculate and visualize the average 2D-diameter distribution and the estimated 3D-size distribution (using the Saltykov-method).

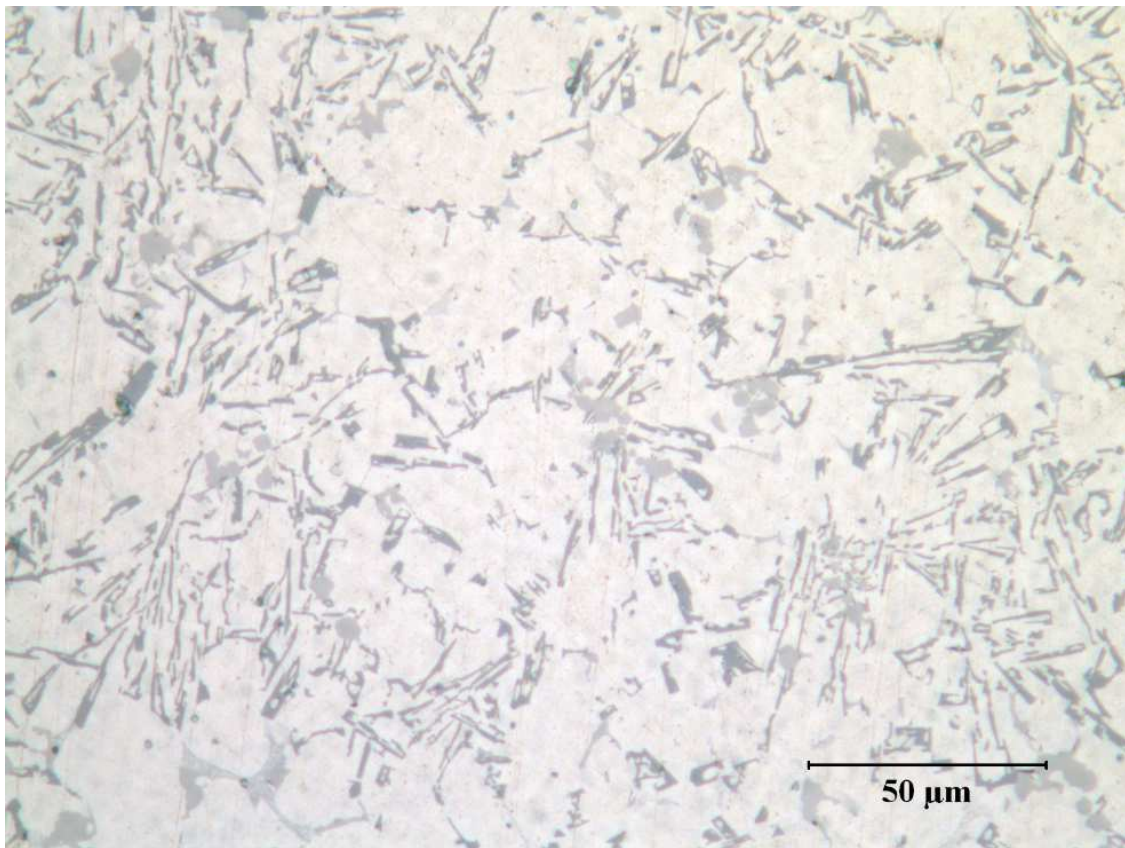


Figure 5.14 Optical micrograph taken from sample 1.

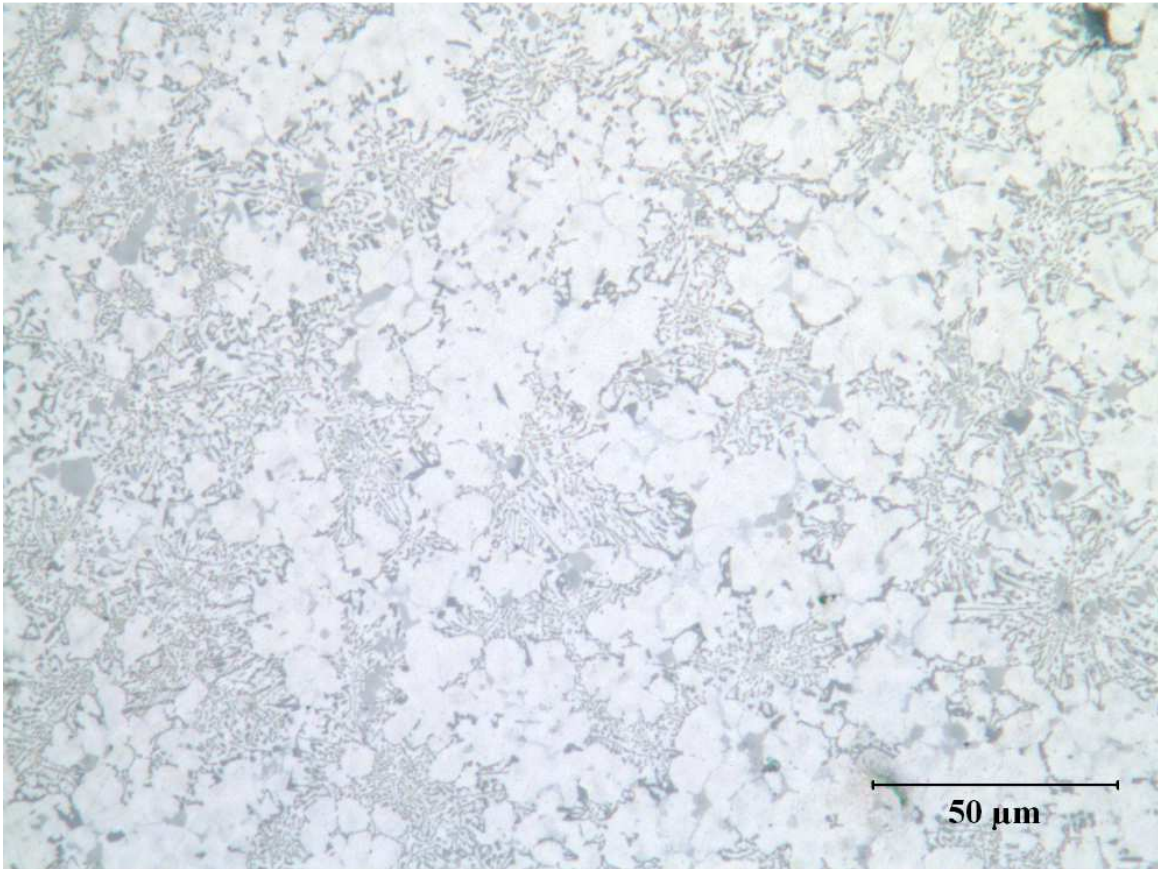


Figure 5.15 Optical micrograph taken from sample 5.

5.4.2 Growth model parameters

The solidification kinetics for the locations of samples 1, 3, 4 and 5 were determined from the NOVAFLOW&SOLID simulation trial 9. Our hypothesis is that the growth of the α -Fe particle starts at the liquidus temperature of the Al-aluminum, and ends at the start of eutectic growth. The parameters used for the solidification model are shown in Table 5.3. The density of α -Fe nuclei in the melt was unknown, so the parameters N_α and V_L were considered fitting parameters.

Table 5.3 Input parameters for α -Fe growth model

Parameter	Value	Source
k	0.029	[37]
D_L	2.7e-9	[75]
C_0	1 wt%	NEMAK Alabama
N_α	1000	Fitting parameter
V_L	4.2e-6	Fitting parameter

5.5 Results and discussion

5.5.1 Samples 1 and 3

Figure 5.16 shows the simulated evolution of temperature and fraction of solid for the bulkhead edge location (samples 1 and 3). It is seen that melt reaches the solidus temperature

after approximately 1.2 seconds, which according to our hypothesis, is the timeframe for α -Fe particle growth.

Figure 5.17 and Figure 5.18 show the measured diameter distributions for the α -Fe particles. The average size is approximately 2 μm . The Saltykov-method correction slightly shifts the distribution to larger diameters, but not significantly.

Figure 5.19 shows the predicted α -Fe diameter evolution according to our solidification model. The agreement with experiments is good.

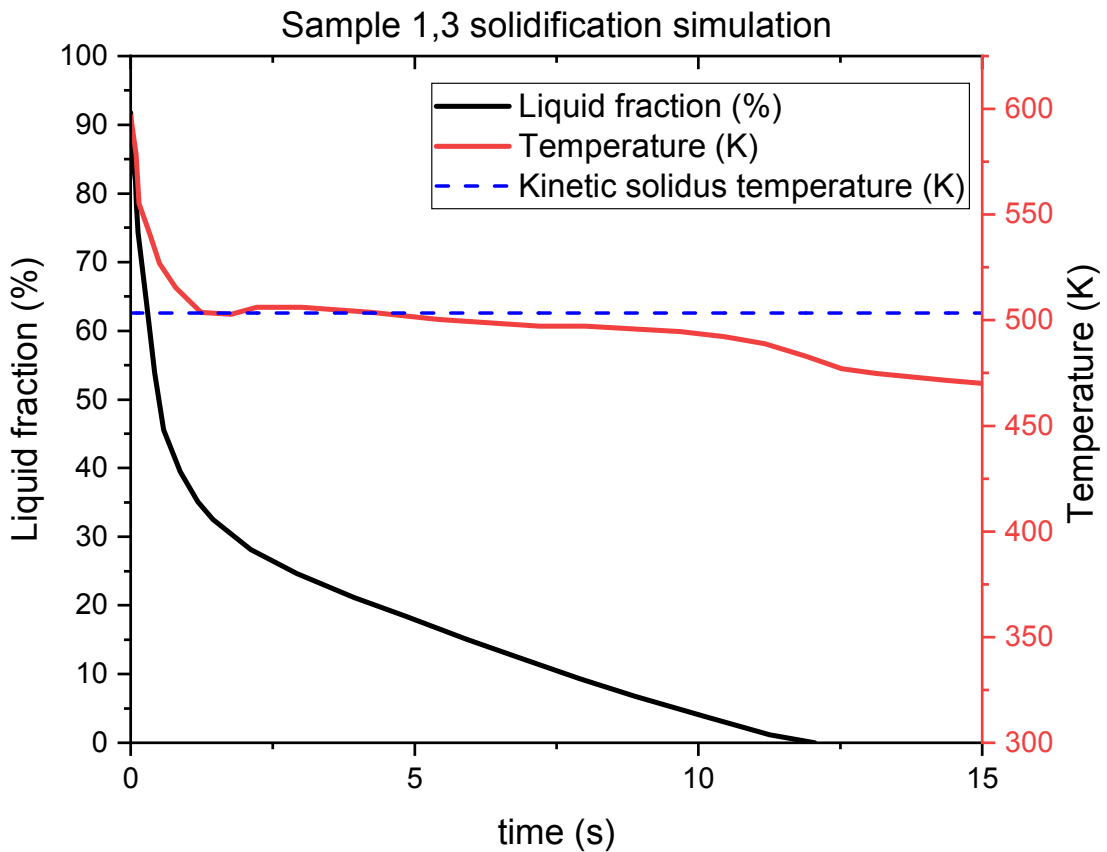


Figure 5.16 NOVAFLOW&SOLID simulation of Samples 1,3

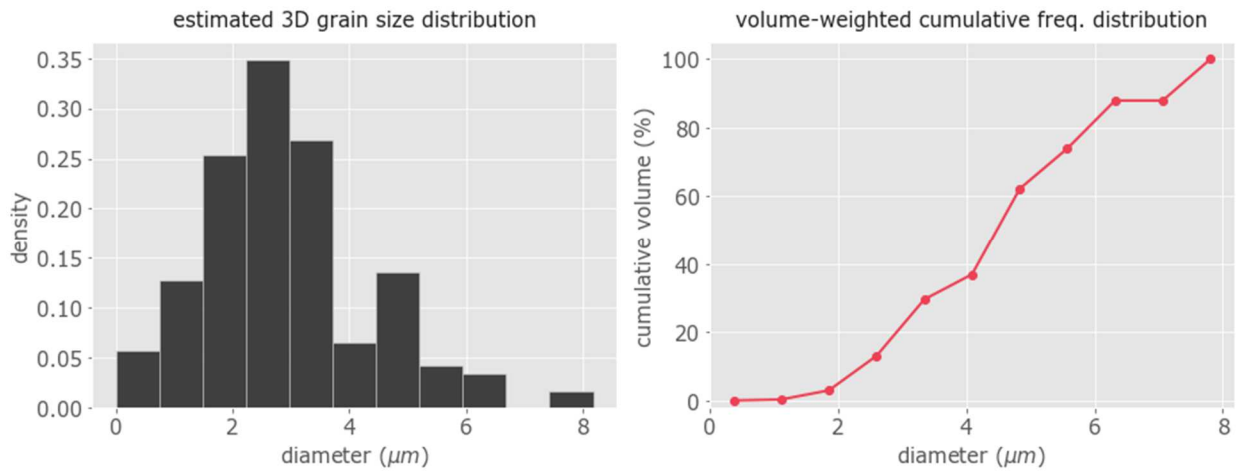
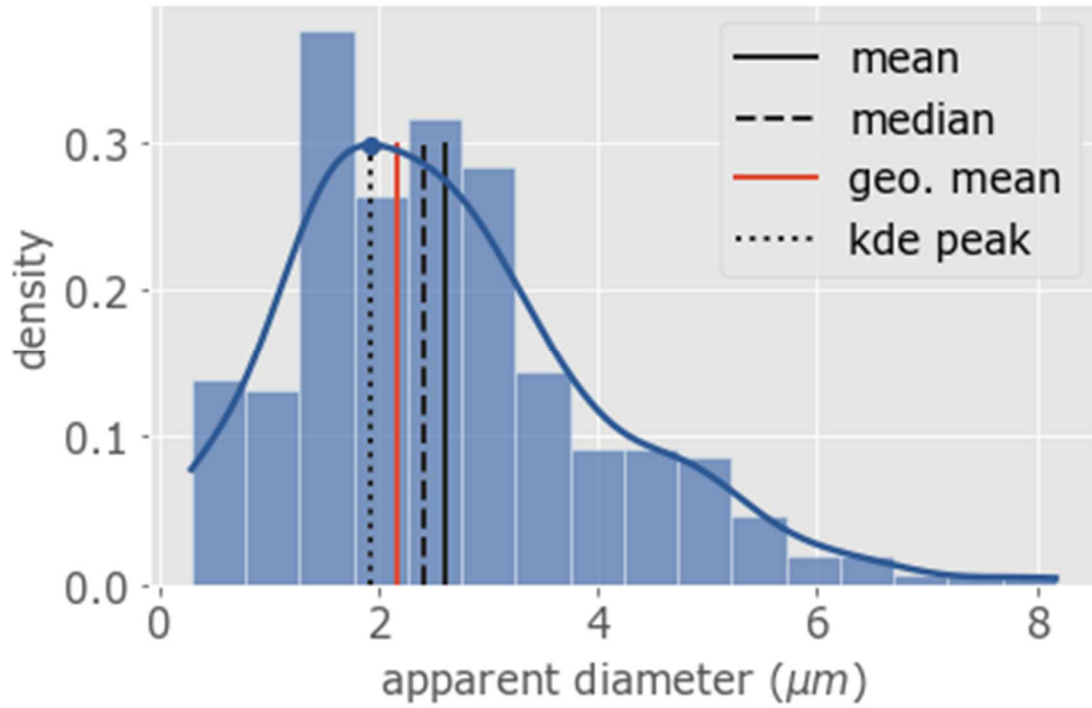


Figure 5.17 Measured α -Fe diameter distribution and Saltykov-method estimate for 3D diameter distribution for sample 1.

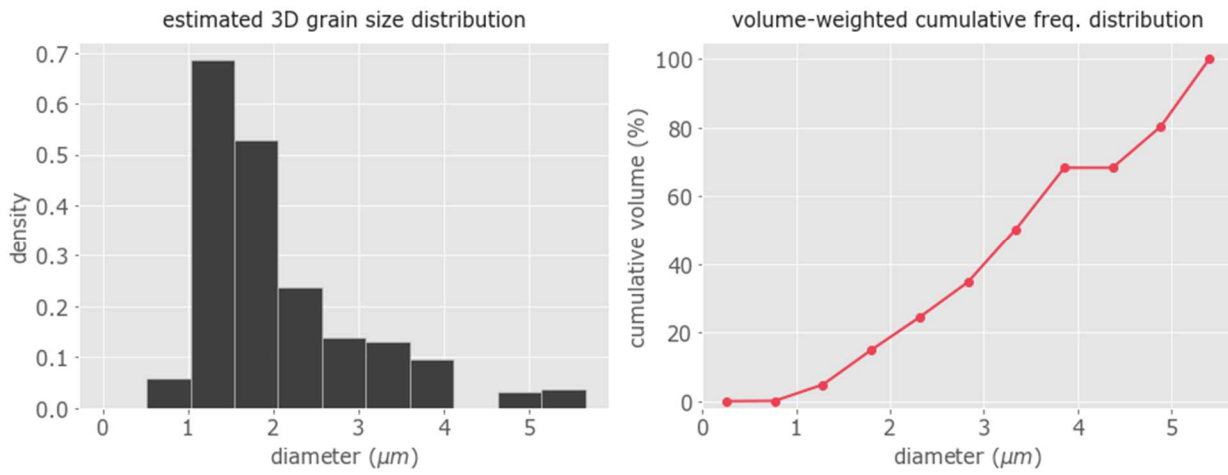
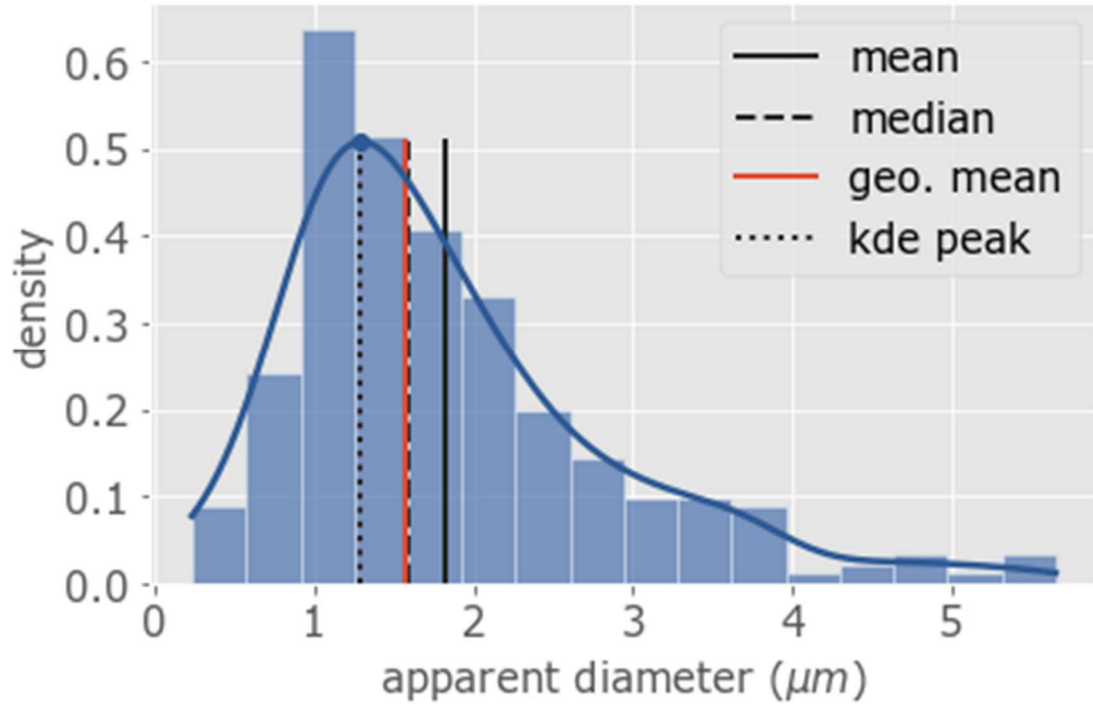


Figure 5.18 Measured α -Fe diameter distribution and Saltykov-method estimate for 3D diameter distribution for sample 3.

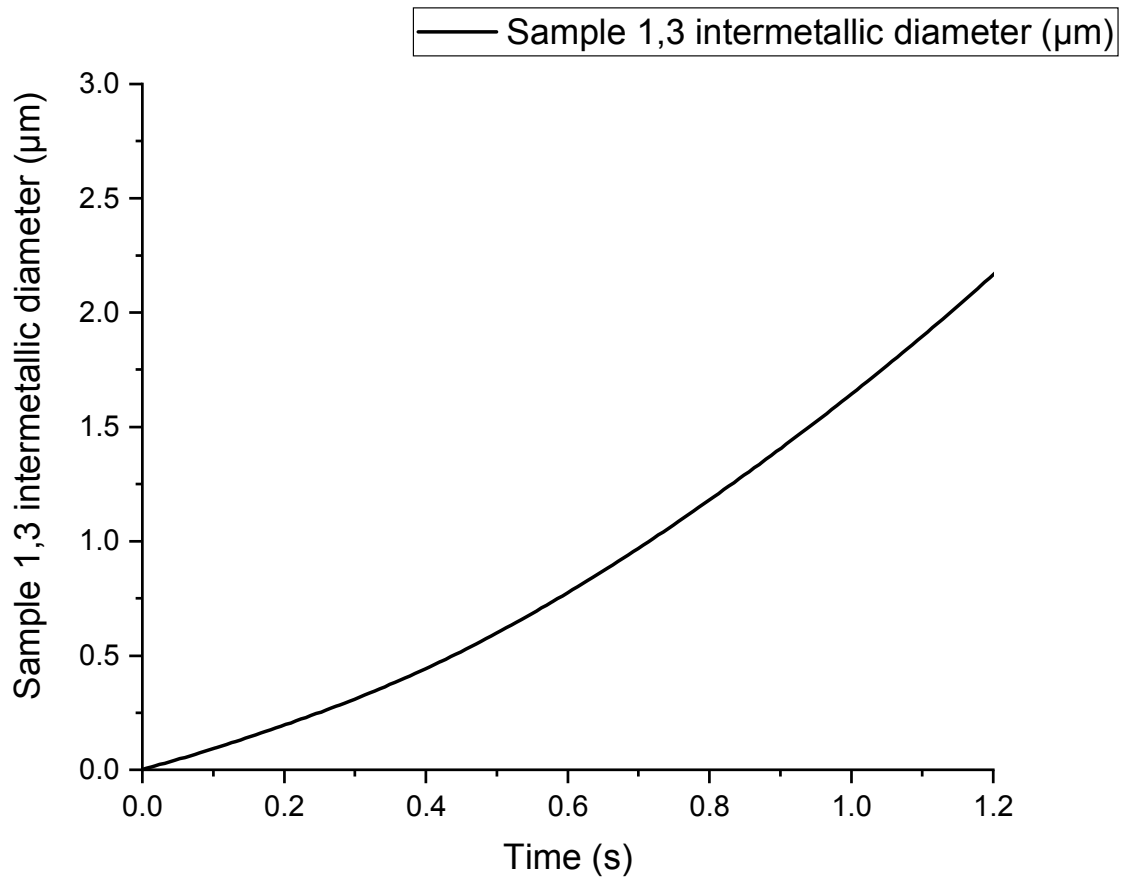


Figure 5.19 α -Fe growth model predicted diameter at samples 1,3

5.5.2 Sample 4

Figure 5.20 shows the simulated evolution of temperature and fraction of solid at the top of the cylinder outer rim (sample 4). It can be seen that melt reaches the solidus temperature after approximately 0.5 seconds.

Figure 5.21 shows the measured diameter distributions for the α -Fe particles. The average size is approximately 1.5 μm . The Saltykov-method correction slightly shifts the distribution to larger diameters, but not significantly.

Figure 5.22 shows the predicted α -Fe diameter evolution according to our solidification model. The agreement with experiments is good.

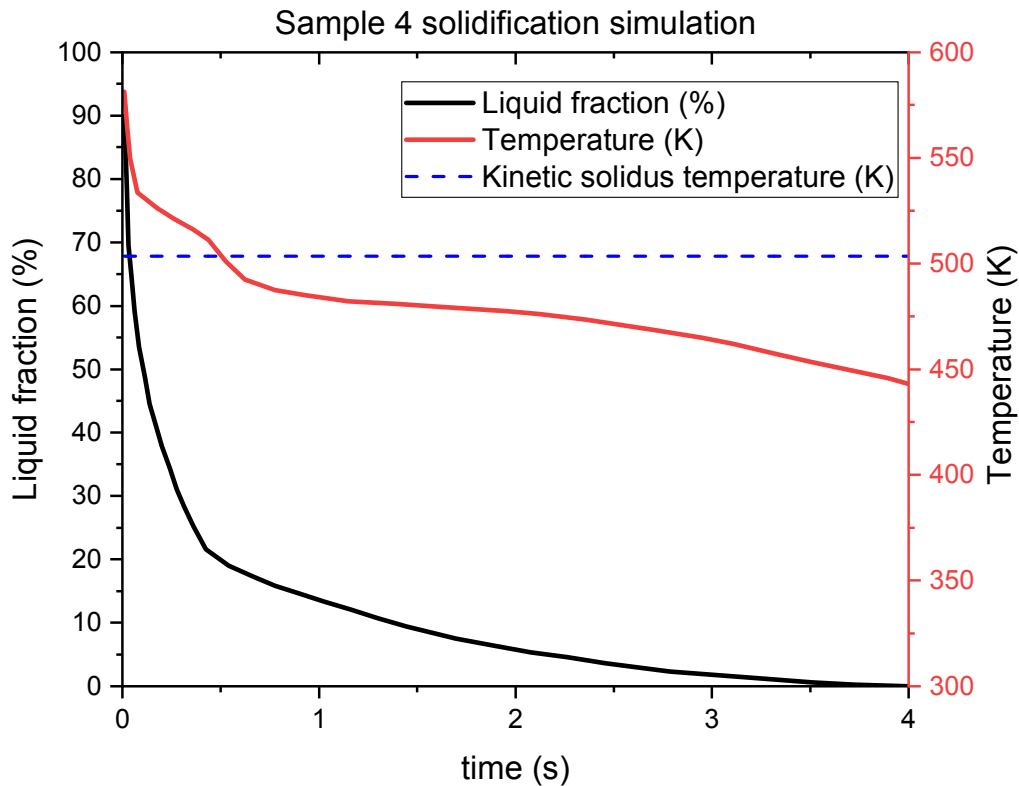


Figure 5.20 NOVAFLOW&SOLID simulation of Sample 4

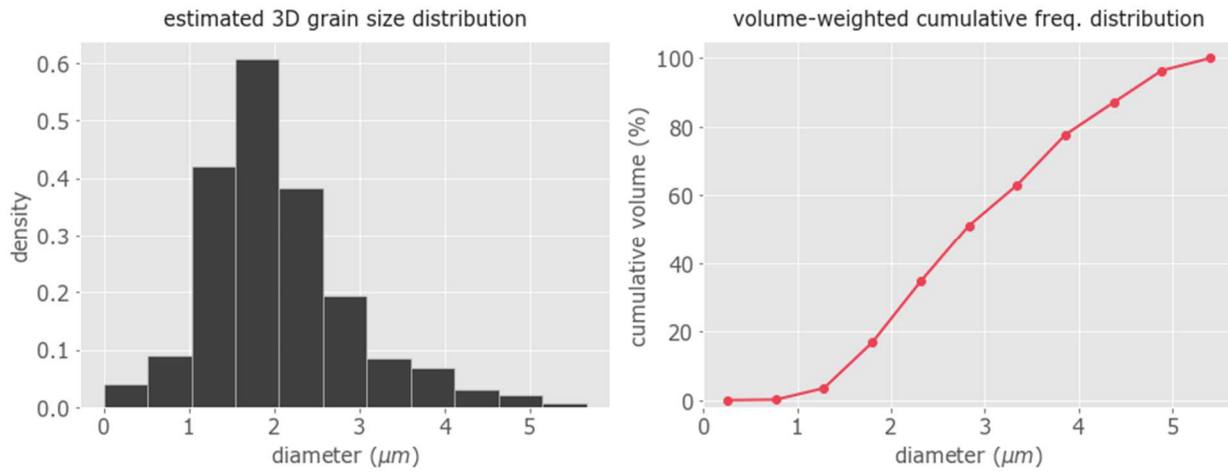
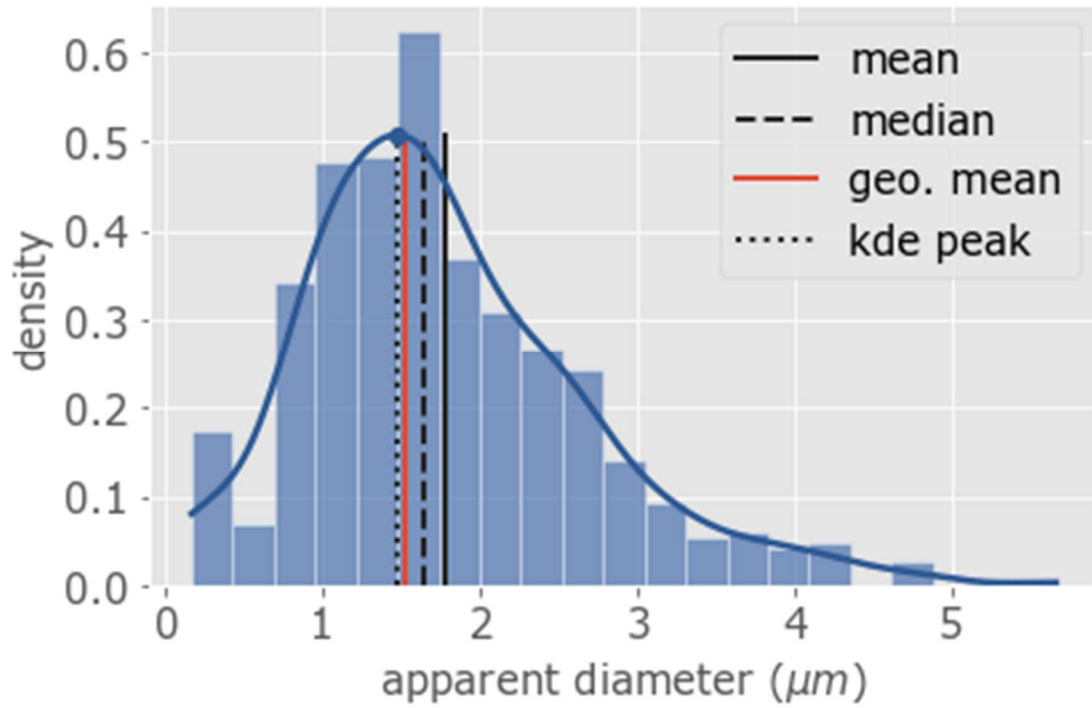


Figure 5.21 Measured α -Fe diameter distribution and Saltykov-method estimate for 3D diameter distribution for sample 4.

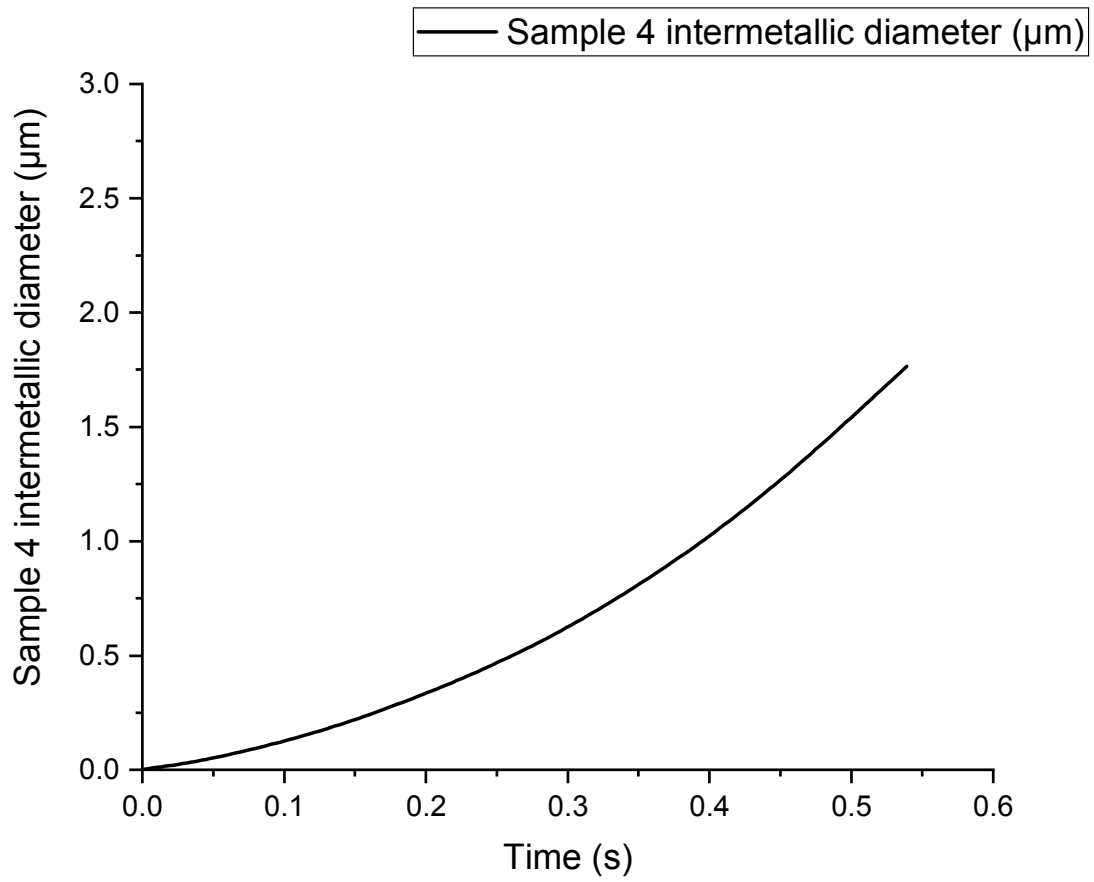


Figure 5.22 α -Fe growth model predicted diameter at sample 4

5.5.2 Sample 5

Figure 5.23 shows the simulated evolution of temperature and fraction of solid at the inner cylinder surface (sample 4). It can be seen that melt reaches the solidus temperature after approximately 3 seconds.

Figure 5.24 shows the measured diameter distributions for the α -Fe particles. The average size is approximately 0.8 μm . The Saltykov-method correction slightly shifts the distribution to larger diameters, but not significantly.

Figure 5.25 shows the predicted α -Fe diameter evolution according to our solidification model. The agreement with experiments is not good. According to the α -Fe particle size, predicted solidification time at this location should be shorter. By looking at Figure 5.23, we can see that the initial cooling rate is slower than in sample 4, even though the final solidification time is similar. It may be that the NOVAFLOW&SOLID does not properly account for the effect of the steel liners adjacent to the cylinder, or the large water cooling channel inside the cylinder.

In general NOVAFLOW&SOLID tends to underestimate the effect of water cooling channels, as seen from the parameter sensitivity analysis.

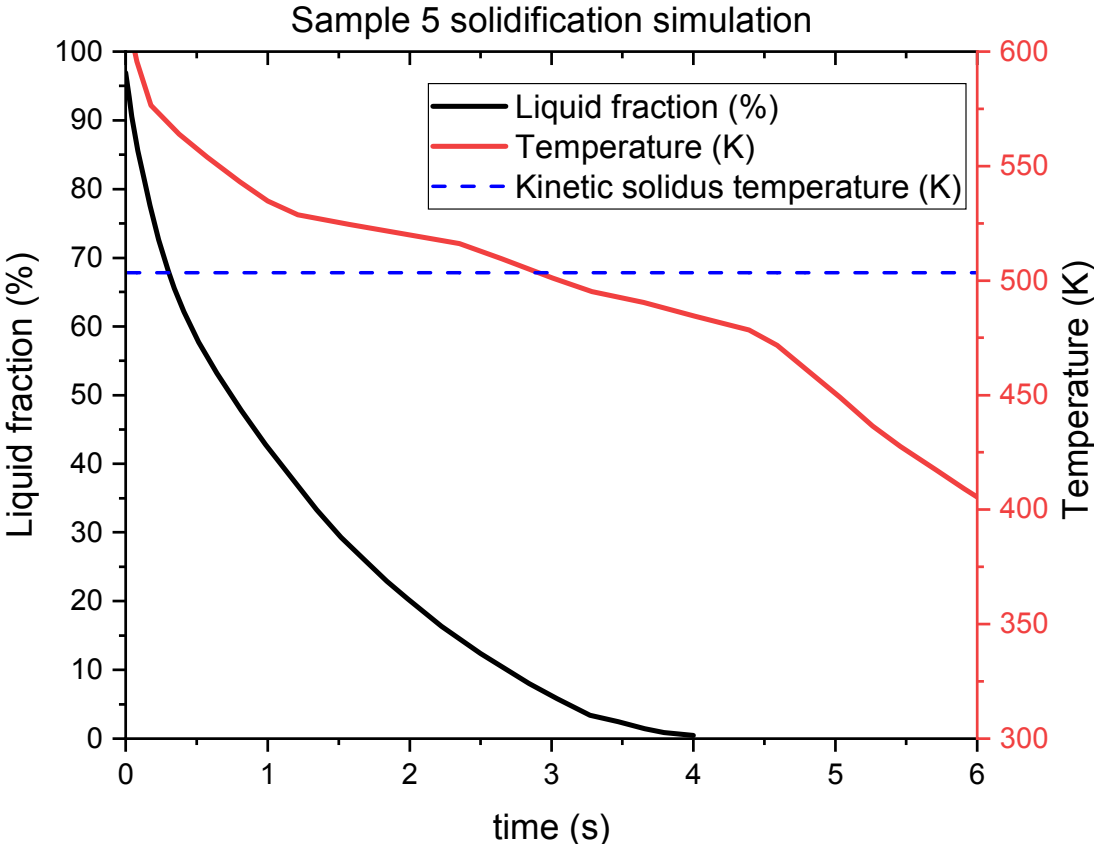


Figure 5.23 NOVAFLOW&SOLID simulation of Sample 5

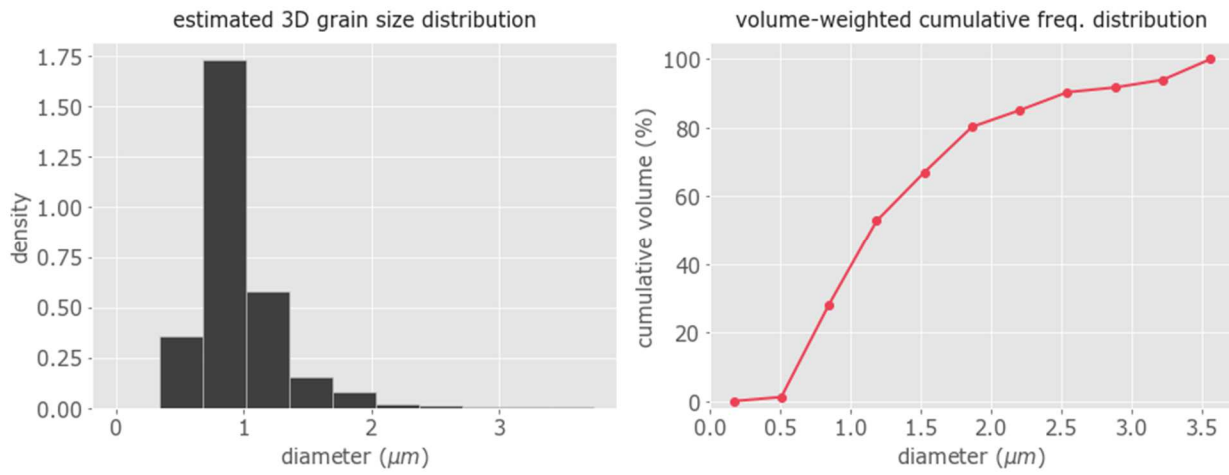
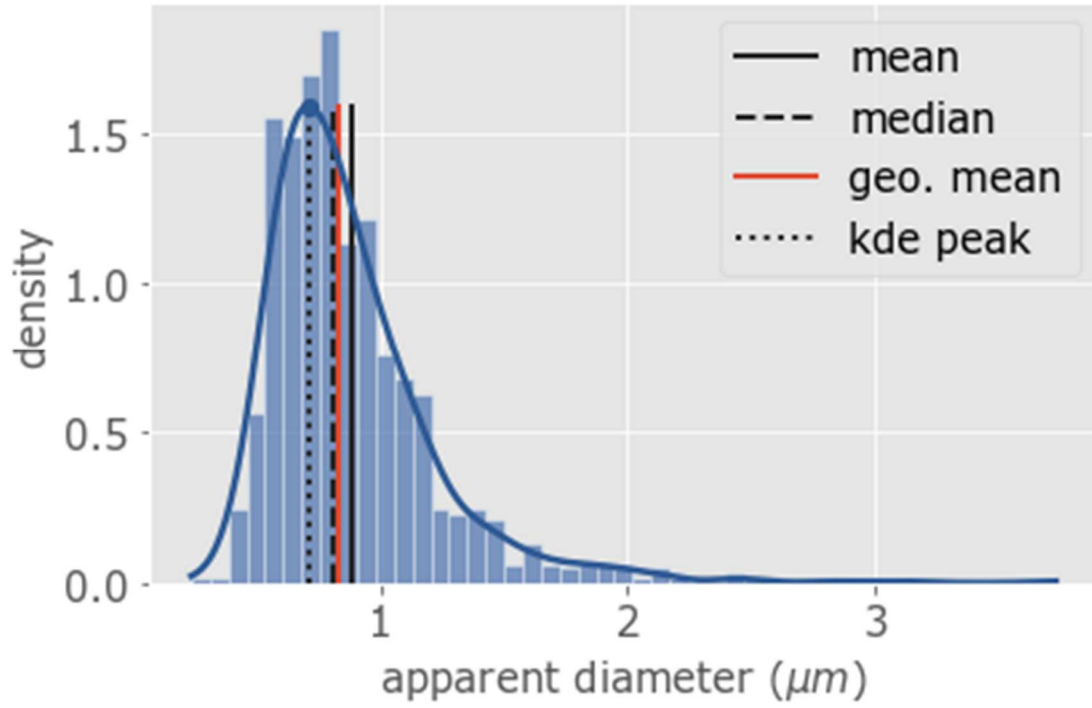


Figure 5.24 Measured α -Fe diameter distribution and Saltykov-method estimate for 3D diameter distribution for sample 5.

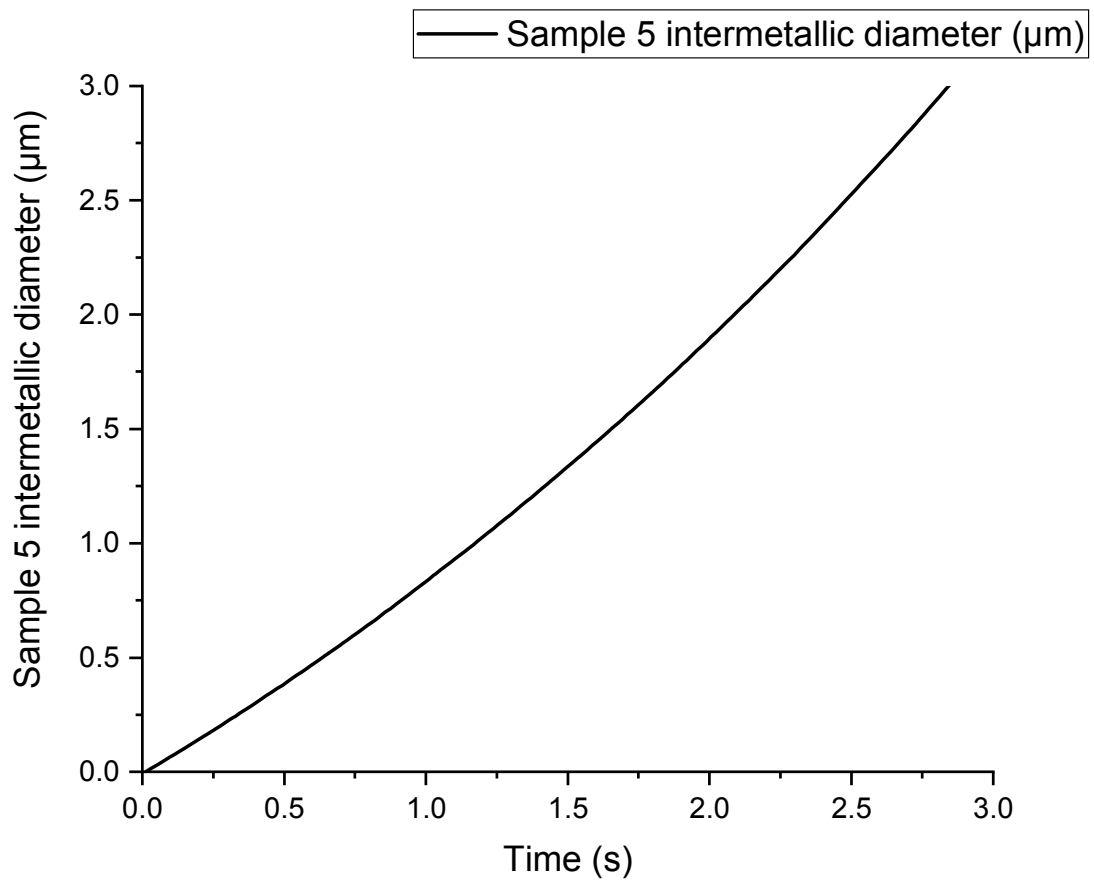


Figure 5.25 α -Fe growth model predicted diameter at sample 5

5.6 Conclusions

- 1) Orthogonal array testing was used to determine fitting parameter values for simulating A383 HPDC heat transfer.
- 2) The Saltykov-method 3D-adjusted α -Fe diameter distribution does not significantly differ from the 2D distribution.
- 3) The average particle diameter is 2.1, 1.6, 1.5, 0.8 μm for samples 1,3,4,5 respectively.
- 4) The α -Fe growth model was able to predict the average size for α -Fe diameter for samples 1,3 and 4. For sample 5, it seems as if the NOVASOLID&FLOW underestimates heat transfer near the cylinder, and thus over-predicts intermetallic size.
- 5) The number of samples is not sufficient to definitively determine the growth mechanism of the α -Fe particle. However, this study forms a good framework for further experiments and simulations.

CHAPTER 6 – CONCLUSIONS AND FUTURE WORK

6.1 Conclusions

6.1.1 Water cooling channels

- 1) A model based on the Gnielinski correlation was developed. It is capable of predicting the Nu-number of bubbler water-cooling channels within 15% margin of error for $6000 < Re < 25000$ and channel diameters up to 5 mm.
- 2) This model can be used to validate water channel models in simulation softwares such as FLUENT or NOVAFLOW&SOLID. This is especially important in the case of commercial software, since their underlying implementation of heat transfer coefficients is usually unknown. This correlation can be used to validate the results of these black box models.

6.1.2 Die-casting interfacial heat transfer coefficient

- 1) The IHTC model by Hamasaiid et al. was found to contain an unrealistic empirical capillary pressure term.
- 2) The impact pressure was predicted using the “water hammer pressure” model. The IHTC values for both Mg and Al alloys matched experimental results very well, when this

- 3) pressure model was used. This is promising, because the material properties and casting conditions for both alloys were very different.
- 4) A model for the time-evolution of the IHTC was developed and implemented in FLUENT 18.1 using .scm script files and UDF-files. Modelling the air gap evolution as a linear function of fraction of solid gave moderately good results. The same fitting constant could be used for both the Mg and Al alloy.

6.1.3 Kinetics of α -Fe intermetallic growth in HPDC A383

- 1) Orthogonal array testing was successfully used to determine fitting parameter values and parameter sensitivity for simulating A383 HPDC heat transfer using NOVAFLOW&SOLID.
- 2) Measured sludge diameter distribution were compared with sizes calculated using numerical solvers for cooling rates and classical solidification theory for particle growth.
- 3) The average particle diameter is 2.1, 1.6, 1.5, 0.8 μm for samples 1,3,4,5 respectively.
- 4) The α -Fe growth model was able to predict the average size for α -Fe diameter for samples 1,3 and 4. For sample 5, it seems as if the NOVASOLID&FLOW underestimates heat transfer near the cylinder, and thus over-predicts intermetallic size.
- 5) The difference between the measured 2D diameters and the corrected estimated 3D diameters using the Saltykov-method was found to be minor.

6.2 Main contributions of this study

- 1) Developed an empirical model for Nusselt number in water cooling channels. This can be used to validate heat transfer coefficients for water cooling channels in commercial software to assist in modelling heat transfer in the HPDC process.
- 2) Developed a model for impact pressure in HPDC, which augments the Hamasaiid model for peak IHTC in HPDC and gives better results than their previous model.
- 3) Developed a method to integrate the Hamasaiid IHTC model as a boundary condition in FLUENT 18.1 using .scm and UDF-files.
- 4) Predicted size of polyhedral Fe-rich intermetallics using commercial casting simulation NOVAFLOW&SOLID for cooling rates and classical solidification theory for intermetallic size. This study lays the framework for how to combine commercial casting simulation software and micrograph measurements to make quantitative predictions of microstructure.

6.3 Recommendations for future work

To further validate the Hamasaiid IHTC model and the impact pressure model of the present study, experiments should be performed with metal jet/droplet striking substrates of varying roughness with varying velocity.

To estimate the impact of fluid flow on the IHTC model, simulations should be carried out with varying flow velocity profiles and surface roughness values to estimate the magnitude of the error caused by ignoring convection in our model.

To validate the heat transfer coefficients used in commercial casting software, comparisons between the models established in the present study and various commercial casting simulation software should be carried out. The findings should be validated with experimental measurements of heat transfer in high-pressure die-castings.

Once the models are validated, the microstructure evolution in the A383 casting should be revisited, and more sophisticated phase transformation models such as the phase field method should be used and compared with classical solidification models.

REFERENCES

- [1] G. Timelli and A. Fabrizi, "The Effects of Microstructure Heterogeneities and Casting Defects on the Mechanical Properties of High-Pressure Die-Cast AlSi9Cu3(Fe) Alloys," *Metallurgical and Materials Transactions A*, vol. 45, pp. 5486-5498, November 01 2014.
- [2] S. Otarawanna, H. I. Laukli, C. M. Gourlay, and A. K. Dahle, "Feeding Mechanisms in High-Pressure Die Castings," *Metallurgical and Materials Transactions A*, vol. 41, pp. 1836-1846, July 01 2010.
- [3] A. Long, D. Thornhill, C. Armstrong, and D. Watson, "Determination of the heat transfer coefficient at the metal-die interface for high pressure die cast AlSi9Cu3Fe," *Applied Thermal Engineering*, vol. 31, pp. 3996-4006, Dec 2011.
- [4] F. Bonollo, N. Gramegna, and G. Timelli, "High-Pressure Die-Casting: Contradictions and Challenges," *JOM*, vol. 67, pp. 901-908, May 01 2015.
- [5] W. D. Callister and D. G. Rethwisch, *Fundamentals of Materials Science and Engineering: An Integrated Approach, 5th Edition*: Wiley, 2016.
- [6] Y. Hangai and S. Kitahara, "Quantitative evaluation of porosity in aluminum alloy die castings by fractal analysis of spatial distribution of area," *Materials & Design*, vol. 30, pp. 1169-1173, Apr 2009.
- [7] G. Lasko, M. Apel, A. Carre, U. Weber, and S. Schmauder, "Effect of Microstructure and Hydrogen Pores on the Mechanical Behavior of an Al7%Si0.3%Mg Alloy Studied by a Combined Phase-Field and Micromechanical Approach," *Advanced Engineering Materials*, vol. 14, pp. 236-247, Apr 2012.
- [8] A. Carre, B. Bottger, and M. Apel, "Phase-field modelling of gas porosity formation during the solidification of aluminium," *International Journal of Materials Research*, vol. 101, pp. 510-514, Apr 2010.
- [9] F. P. Incropera, *Fundamentals of Heat and Mass Transfer*: John Wiley & Sons, Inc., 2006.
- [10] H. Herwig, "What Exactly is the Nusselt Number in Convective Heat Transfer Problems and are There Alternatives?," *Entropy*, vol. 18, May 2016.

- [11] D. D. Ndenguma, J. Dirker, and J. P. Meyer, "Heat transfer and pressure drop in annuli with approximately uniform internal wall temperatures in the transitional flow regime," *International Journal of Heat and Mass Transfer*, vol. 111, pp. 429-441, 2017.
- [12] A. Hamasaiid, G. Dour, M. S. Dargusch, T. Loulou, C. Davidson, and G. Savage, "Heat-transfer coefficient and in-cavity pressure at the casting-die interface during high-pressure die casting of the magnesium alloy AZ91D," *Metallurgical and Materials Transactions a-Physical Metallurgy and Materials Science*, vol. 39a, pp. 853-864, Apr 2008.
- [13] G. Dour, M. Dargusch, C. Davidson, and A. Nef, "Development of a non-intrusive heat transfer coefficient gauge and its application to high pressure die casting - Effect of the process parameters," *Journal of Materials Processing Technology*, vol. 169, pp. 223-233, Nov 10 2005.
- [14] Z. P. Guo, S. M. Xiong, B. C. Liu, M. Li, and J. Allison, "Effect of Process Parameters, Casting Thickness, and Alloys on the Interfacial Heat-Transfer Coefficient in the High-Pressure Die-Casting Process," *Metallurgical and Materials Transactions a-Physical Metallurgy and Materials Science*, vol. 39a, pp. 2896-2905, Dec 2008.
- [15] M. S. Dargusch, A. Hamasaiid, G. Dour, T. Loulou, C. J. Davidson, and D. H. St John, "The accurate determination of heat transfer coefficient and its evolution with time during high pressure die casting of Al-9%Si-3%Cu and Mg-9%Al-1%Zn alloys," *Advanced Engineering Materials*, vol. 9, pp. 995-999, Nov 2007.
- [16] A. Hamasaiid, G. Wang, C. Davidson, G. Dour, and M. S. Dargusch, "Interfacial Heat Transfer during Die Casting of an Al-Si-Cu Alloy," *Metallurgical and Materials Transactions A*, vol. 40, p. 3056, 2009/10/27 2009.
- [17] Z. W. Chen, "Skin solidification during high pressure die casting of Al-11Si-2Cu-1Fe alloy," *Materials Science and Engineering: A*, vol. 348, pp. 145-153, 2003/05/15/ 2003.
- [18] A. Hamasaiid, M. S. Dargusch, T. Loulou, and G. Dour, "A predictive model for the thermal contact resistance at liquid-solid interfaces: Analytical developments and validation," *International Journal of Thermal Sciences*, vol. 50, pp. 1445-1459, 2011/08/01/ 2011.
- [19] Y. Cao, Z. Guo, and S. Xiong, "Determination of the metal/die interfacial heat transfer coefficient of high pressure die cast B390 alloy," *IOP Conference Series: Materials Science and Engineering*, vol. 33, p. 012010, 2012/07/03 2012.
- [20] W. D. Griffiths and K. Kawai, "The effect of increased pressure on interfacial heat transfer in the aluminium gravity die casting process," *Journal of Materials Science*, vol. 45, pp. 2330-2339, 2010/05/01 2010.

- [21] S. Mirbagheri, M. Shrinparvar, and A. Chirazi, "Modeling of metallo-static pressure on the metal–mould interface thermal resistance in the casting process," *Materials & design*, vol. 28, pp. 2106-2112, 2007.
- [22] W.-w. Zhang, Y.-l. Zhao, D.-t. Zhang, Z.-q. Luo, C. Yang, and Y.-y. Li, "Effect of Si addition and applied pressure on microstructure and tensile properties of as-cast Al-5.0 Cu-0.6 Mn-1.2 Fe alloys," *Trans. Nonferrous Met. Soc. China*, vol. 28, p. 1072, 2018.
- [23] M. C. Flemings, "Behavior of metal alloys in the semisolid state," *Metallurgical Transactions A*, vol. 22, pp. 957-981, 1991/05/01 1991.
- [24] W.-b. Yu, S. Liang, Y.-y. Cao, X.-b. Li, Z.-p. Guo, and S.-m. Xiong, "Interfacial heat transfer behavior at metal/die in finger-plated casting during high pressure die casting process," *China Foundry*, vol. 14, pp. 258-264, July 01 2017.
- [25] A. Hamasaiid, G. Dour, T. Loulou, and M. S. Dargusch, "A predictive model for the evolution of the thermal conductance at the casting–die interfaces in high pressure die casting," *International Journal of Thermal Sciences*, vol. 49, pp. 365-372, 2010/02/01/ 2010.
- [26] M. Qi, Y. Kang, Q. Qiu, W. Tang, J. Li, and B. Li, "Microstructures, mechanical properties, and corrosion behavior of novel high-thermal-conductivity hypoeutectic Al-Si alloys prepared by rheological high pressure die-casting and high pressure die-casting," *Journal of Alloys and Compounds*, vol. 749, pp. 487-502, 2018/06/15/ 2018.
- [27] M.-f. Qi, Y.-l. Kang, and G.-m. Zhu, "Microstructure and properties of rheo-HPDC Al-8Si alloy prepared by air-cooled stirring rod process," *Transactions of Nonferrous Metals Society of China*, vol. 27, pp. 1939-1946, 2017/09/01/ 2017.
- [28] E. Brosh, G. Makov, and R. Z. Shneck, "Application of CALPHAD to high pressures," *Calphad-Computer Coupling of Phase Diagrams and Thermochemistry*, vol. 31, pp. 173-185, Jun 2007.
- [29] J. J. Sobczak, L. Drenchev, and R. Asthana, "Effect of pressure on solidification of metallic materials," *International Journal of Cast Metals Research*, vol. 25, pp. 1-14, 2012/01/01 2012.
- [30] S. G. Shabestari and J. E. Gruzleski, "The Effect of Solidification Condition and Chemistry on the Formation and Morphology of Complex Intermetallic Compounds in Aluminium—Silicon Alloys," *Cast Metals*, vol. 6, pp. 217-224, 1994/01/01 1994.
- [31] S. Ji, W. Yang, F. Gao, D. Watson, and Z. Fan, "Effect of iron on the microstructure and mechanical property of Al–Mg–Si–Mn and Al–Mg–Si diecast alloys," *Materials Science and Engineering: A*, vol. 564, pp. 130-139, 2013/03/01/ 2013.

- [32] H. Z. Ye, "An overview of the development of Al-Si-alloy based material for engine applications," *Journal of Materials Engineering and Performance*, vol. 12, pp. 288-297, Jun 2003.
- [33] M. Javidani and D. Larouche, "Application of cast Al-Si alloys in internal combustion engine components," *International Materials Reviews*, vol. 59, pp. 132-158, 2014/04/01 2014.
- [34] J. Eiken, M. Apel, S. M. Liang, and R. Schmid-Fetzer, "Impact of P and Sr on solidification sequence and morphology of hypoeutectic Al-Si alloys: Combined thermodynamic computation and phase-field simulation," *Acta Materialia*, vol. 98, pp. 152-163, Oct 1 2015.
- [35] S. W. Choi, Y. M. Kim, K. M. Lee, H. S. Cho, S. K. Hong, Y. C. Kim, *et al.*, "The effects of cooling rate and heat treatment on mechanical and thermal characteristics of Al-Si-Cu-Mg foundry alloys," *Journal of Alloys and Compounds*, vol. 617, pp. 654-659, Dec 25 2014.
- [36] T. Liu, S. Morales, M. Karkkainen, L. Nastac, V. Arvikar, I. Levin, *et al.*, "The combined effects of Sr additions and heat treatment on the microstructure and mechanical properties of high pressure die cast A383 alloy," *Materials Science and Engineering: A*, 2019.
- [37] J. A. Taylor, "Iron-Containing Intermetallic Phases in Al-Si Based Casting Alloys," *Procedia Materials Science*, vol. 1, pp. 19-33, 2012/01/01/ 2012.
- [38] S. Ferraro and G. Timelli, "Influence of Sludge Particles on the Tensile Properties of Die-Cast Secondary Aluminum Alloys," *Metallurgical and Materials Transactions B*, vol. 46, pp. 1022-1034, 2015/04/01 2015.
- [39] M. Timpel, N. Wanderka, R. Grothausmann, and J. Banhart, "Distribution of Fe-rich phases in eutectic grains of Sr-modified Al-10wt.% Si-0.1wt.% Fe casting alloy," *Journal of Alloys and Compounds*, vol. 558, pp. 18-25, 2013/05/05/ 2013.
- [40] G. Timelli, A. Fabrizi, S. Capuzzi, F. Bonollo, and S. Ferraro, "The role of Cr additions and Fe-rich compounds on microstructural features and impact toughness of AlSi9Cu3(Fe) diecasting alloys," *Materials Science and Engineering: A*, vol. 603, pp. 58-68, 2014/05/06/ 2014.
- [41] S. Roy, L. Allard, A. Rodriguez, T. Watkins, and A. Shyam, "Comparative Evaluation of Cast Aluminum Alloys for Automotive Cylinder Heads: Part I-Microstructure Evolution," *Metallurgical and Materials Transactions a-Physical Metallurgy and Materials Science*, vol. 48a, pp. 2529-2542, May 2017.
- [42] F. Jiahong, "Uncertainty quantification on industrial high pressure die casting process," *Open Access Theses*, vol. 849, 2016.

- [43] J. A. Dantzig and M. Rappaz, *Solidification*, 1st ed ed.: EPFL Press ; London : Taylor & Francis [distributor], 2009.
- [44] E. Anglada, A. Meléndez, I. Vicario, E. Arratibel, and I. Aguillo, "Adjustment of a High Pressure Die Casting Simulation Model Against Experimental Data," *Procedia Engineering*, vol. 132, pp. 966-973, 2015/01/01/ 2015.
- [45] L. Zhang, L. Li, H. Ju, and B. Zhu, "Inverse identification of interfacial heat transfer coefficient between the casting and metal mold using neural network," *Energy Conversion and Management*, vol. 51, pp. 1898-1904, 2010/10/01/ 2010.
- [46] R. Helenius, O. Lohne, L. Arnberg, and H. I. Laukli, "The heat transfer during filling of a high-pressure die-casting shot sleeve," *Materials Science and Engineering a-Structural Materials Properties Microstructure and Processing*, vol. 413, pp. 52-55, Dec 15 2005.
- [47] Z. P. Guo, S. M. Xiong, B. C. Liu, L. Mei, and J. Allison, "Determination of the heat transfer coefficient at metal-die interface of high pressure die casting process of AM50 alloy," *International Journal of Heat and Mass Transfer*, vol. 51, pp. 6032-6038, Dec 2008.
- [48] Y. Cao, Z. Guo, and S. Xiong, "Determination of interfacial heat transfer coefficient and its application in high pressure die casting process," *China Foundry*, vol. 11, pp. 314-321, // 2014.
- [49] M. Xue, Y. Heichal, S. Chandra, and J. Mostaghimi, "Modeling the impact of a molten metal droplet on a solid surface using variable interfacial thermal contact resistance," *Journal of Materials Science*, vol. 42, pp. 9-18, 2007/01/01 2007.
- [50] C. Yuan, B. Duan, L. Li, B. Shang, and X. Luo, "An improved model for predicting thermal contact resistance at liquid–solid interface," *International Journal of Heat and Mass Transfer*, vol. 80, pp. 398-406, 2015/01/01/ 2015.
- [51] S. C. Somé, D. Delaunay, and V. Gaudefroy, "Comparison and validation of thermal contact resistance models at solid–liquid interface taking into account the wettability parameters," *Applied Thermal Engineering*, vol. 61, pp. 531-540, 2013/11/03/ 2013.
- [52] L. Davidson, "An introduction to turbulence models," 2015.
- [53] C. Argyropoulos and N. Markatos, "Recent advances on the numerical modelling of turbulent flows," *Applied Mathematical Modelling*, vol. 39, pp. 693-732, 2015.
- [54] A. Fluent, "17.1: User's guide. ANSYS," ed: Inc.
- [55] V. Gnielinski, "On heat transfer in tubes," *International Journal of Heat and Mass Transfer*, vol. 63, pp. 134-140, 2013.

- [56] B. Petukhov, "Heat transfer and friction in turbulent pipe flow with variable physical properties," in *Advances in heat transfer*. vol. 6, ed: Elsevier, 1970, pp. 503-564.
- [57] V. Gnielinski, "Turbulent Heat Transfer in Annular Spaces-A New Comprehensive Correlation," *Heat Transfer Engineering*, vol. 36, pp. 787-789, Jun 13 2015.
- [58] W. R. Van Zyl, J. Dirker, and J. P. Meyer, "Single-phase convective heat transfer and pressure drop coefficients in concentric annuli," *Heat Transfer Engineering*, vol. 34, pp. 1112-1123, 2013.
- [59] D. R. Poirier and G. Geiger, *Transport phenomena in materials processing*: Springer, 2016.
- [60] Y. Heichal and S. Chandra, "Predicting thermal contact resistance between molten metal droplets and a solid surface," *Journal of Heat Transfer-Transactions of the Asme*, vol. 127, pp. 1269-1275, Nov 2005.
- [61] M. G. Cooper, B. B. Mikic, and M. M. Yovanovich, "Thermal contact conductance," *International Journal of Heat and Mass Transfer*, vol. 12, pp. 279-300, 1969/03/01/ 1969.
- [62] R. S. Prasher, "Surface chemistry and characteristics based model for the thermal contact resistance of fluidic interstitial thermal interface materials," *Journal of Heat Transfer-Transactions of the Asme*, vol. 123, pp. 969-975, Oct 2001.
- [63] S.-H. Park, Y.-S. Um, C.-H. Kum, and B.-Y. Hur, "Thermophysical properties of Al and Mg alloys for metal foam fabrication," *Colloids and Surfaces A: Physicochemical and Engineering Aspects*, vol. 263, pp. 280-283, 2005/08/01/ 2005.
- [64] M. Gatzen, T. Radel, C. Thomy, and F. Vollertsen, "The Role of Zinc Layer During Wetting of Aluminium on Zinc-coated Steel in Laser Brazing and Welding," *Physics Procedia*, vol. 56, pp. 730-739, 2014/01/01/ 2014.
- [65] B. Wang, "Investigation of the adhesion behavior of aluminum on various PVD coatings applied to H13 tool steel to minimize or eliminate lubrication during high pressure die casting, An," Colorado School of Mines. Arthur Lakes Library, 2016.
- [66] Y. Tatekura, M. Watanabe, K. Kobayashi, and T. Sanada, "Pressure generated at the instant of impact between a liquid droplet and solid surface," *Royal Society open science*, vol. 5, p. 181101, 2018.
- [67] D. Wang and R. A. Overfelt, "Oscillating Cup Viscosity Measurements of Aluminum Alloys: A201, A319 and A356," *International Journal of Thermophysics*, vol. 23, pp. 1063-1076, 2002/07/01 2002.

- [68] P. Thakor, V. Patel, B. Thakore, P. Gajjar, and A. Jani, "Bulk modulus of some simple liquid metals," 2008.
- [69] S. J. Roach and H. Henein, "Physical Properties of AZ91D Measured Using the Draining Crucible Method: Effect of SF₆," *International Journal of Thermophysics*, vol. 33, pp. 484-494, 2012/03/01 2012.
- [70] J. Xiong, S. Koshizuka, and M. Sakai, "Numerical Analysis of Droplet Impingement Using the Moving Particle Semi-implicit Method," *Journal of Nuclear Science and Technology*, vol. 47, pp. 314-321, 2010/03/01 2010.
- [71] S. Ferraro, A. Fabrizi, and G. Timelli, "Evolution of sludge particles in secondary die-cast aluminum alloys as function of Fe, Mn and Cr contents," *Materials Chemistry and Physics*, vol. 153, pp. 168-179, 2015/03/01/ 2015.
- [72] L. Nastac and D. M. Stefanescu, "Computational modeling of NbC/laves formation in INCONEL 718 equiaxed castings," *Metallurgical and Materials Transactions A*, vol. 28, pp. 1582-1587, 1997/07/01 1997.
- [73] Z. Que, Y. Wang, and Z. Fan, "Formation of the Fe-Containing Intermetallic Compounds during Solidification of Al-5Mg-2Si-0.7Mn-1.1Fe Alloy," *Metallurgical and Materials Transactions A*, vol. 49, pp. 2173-2181, 2018/06/01 2018.
- [74] A. Redjaïmia, A. Prout, P. Donnadieu, and J. Morniroli, "Morphology, crystallography and defects of the intermetallic χ -phase precipitated in a duplex ($\delta + \gamma$) stainless steel," *Journal of materials science*, vol. 39, pp. 2371-2386, 2004.
- [75] N. Lee and J. Cahoon, "Interdiffusion of Copper and Iron in Liquid Aluminum," *Journal of Phase Equilibria and Diffusion*, vol. 32, pp. 226-234, 2011/06/01 2011.
- [76] T. Danilenko, "Method for the simulation and reconstruction of 3D particle size distributions in metal structures," in *MATEC Web of Conferences*, 2018, p. 01002.
- [77] V. R. Joseph, "Taguchi's approach to robust parameter design: A new perspective," *IIE Transactions*, vol. 39, pp. 805-810, 2007/05/28 2007.
- [78] P. K. H. Lin, L. P. Sullivan, and G. Taguchi, "Using Taguchi Methods in Quality Engineering," *Quality Progress*, vol. 23, pp. 55-59, Sep 1990.

APPENDIX A

;;; SCHEME FILE FOR CALCULATING INITIAL HTC for A380

;;; AUTHOR: Mikko Karkkainen

;;; Initialize variable for initial thickness and total thickness

(rp-var-define 'thickness 0 'real #f)

(rp-var-define 'total_thickness 0.002 'real #f)

;;; Initialize variable for air gap

(rp-var-define 'y_0 0 'real #f)

;;; Initialize fitting constant for evolution

(rp-var-define 'c 0.0000001 'real #f)

(rp-var-define 'k_res 1000 'real #f)

;;; Initialize material and processing parameters

(rp-var-define 'pi 3.14159265358979323846 'real #f)

(rp-var-define 'v 2.9 'real #f) ;; cast metal impact velocity

(rp-var-define 'wave_speed 3840.0 'real #f) ;; sonic wave speed in melt

(rp-var-define 'rho 2830.0 'real #f) ;; cast metal densit

```

(rp-var-define 'impact_angle 0.061 'real #f); // Impact angle in radians

(rp-var-define 'k_m 29.0 'real #f) ;; mould thermal conductivity

(rp-var-define 'k_c 109.0 'real #f) ;; cast metal thermal conductivity

(rp-var-define 'r_sm (* 128.7 (expt 10.0 -6.0)) 'real #f) ;; Mean peak spacing

(rp-var-define 'sigma (* 0.578 (expt 10.0 -6.0)) 'real #f) ;; Mean peak height deviation

(rp-var-define 'epsilon 1.5 'real #f) ;; numerical parameter

(rp-var-define 'p_0 101325 'real #f) ;; NTP pressure

(rp-var-define 't_1 860.0 'real #f) ;; impact temperature

(rp-var-define 't_0 300.0 'real #f) ;; NTP temperature

;;; ;; Initialize variable for the wall zone id and shadow wall id of the thin-wall

(rp-var-define 'wall_id 4 'real #f)

(rp-var-define 'shadow_wall_id 15 'real #f)

;;; Run DEFINE_ON_DEMAND(initial_htc) to calculate the value of wall thickness and assign
it in the variable 'thickness

(%udf-on-demand 'ihtc::libudf)

;;; Run the menu command to apply the initial wall thickness to the thin-wall

(ti-menu-load-string (string-append "def bc wall" " " (number->string (%rpgetvar 'wall_id)) " "
(number->string (%rpgetvar 'thickness)) " ,,,,,,"))

```

APPENDIX B

;;; SCHEME FILE FOR CALCULATING INITIAL HTC for AZ91D

;;; AUTHOR: Mikko Karkkainen

;;; Initialize variable for virtual wall thickness

(rp-var-define 'thickness 0 'real #f)

;;; Initialize variable for air gap

(rp-var-define 'y_0 0 'real #f)

;;; Initialize fitting constant for evolution

(rp-var-define 'c 0.0000001 'real #f)

(rp-var-define 'k_res 1000 'real #f)

;;; Initialize material and processing parameters

(rp-var-define 'pi 3.14159265358979323846 'real #f)

(rp-var-define 'v 5.7 'real #f) ;; cast metal impact velocity

(rp-var-define 'wave_speed 3357.0 'real #f) ;; sonic wave speed in melt

(rp-var-define 'rho 1810.0 'real #f) ;; cast metal density

```

(rp-var-define 'impact_angle 0.061 'real #f); // Impact angle in radians

(rp-var-define 'k_m 29.0 'real #f) ;; mould thermal conductivity

(rp-var-define 'k_c 70.0 'real #f) ;; melt thermal conductivity

(rp-var-define 'r_sm (* 128.7 (expt 10.0 -6.0)) 'real #f) ;; Mean peak spacing

(rp-var-define 'sigma (* 0.578 (expt 10.0 -6.0)) 'real #f) ;; Mean peak height deviation

(rp-var-define 'epsilon 1.5 'real #f) ;; numerical parameter

(rp-var-define 'p_0 101325 'real #f) ;; NTP pressure

(rp-var-define 't_1 880.0 'real #f) ;; impact temperature

(rp-var-define 't_0 300.0 'real #f) ;; NTP temperature

;;; ;; Initialize variable for the wall zone id and shadow wall id of the thin-wall

(rp-var-define 'wall_id 4 'real #f)

(rp-var-define 'shadow_wall_id 15 'real #f)

;;; Run DEFINE_ON_DEMAND(initial_htc) to calculate the value of wall thickness and assign
it in the variable 'thickness

(%udf-on-demand 'ihtc::libudf)

;;; Run the menu command to apply the initial wall thickness to the thin-wall

(ti-menu-load-string (string-append "def bc wall" " " (number->string (%rpgetvar 'wall_id)) " "
(number->string (%rpgetvar 'thickness)) " ,,,,,,")

```

APPENDIX C

```
DEFINE_ON_DEMAND(ihtc)
{
real PI = RP_Get_Real("pi");
real v = RP_Get_Real("v"); // cast metal impact velocity
real wave_speed = RP_Get_Real("wave_speed"); // sonic wave speed melt
real rho = RP_Get_Real("rho"); // cast metal density
real impact_angle = RP_Get_Real("impact_angle"); // Impact angle in degrees
real k_m = RP_Get_Real("k_m"); // mould thermal conductivity
real k_c = RP_Get_Real("k_c"); // cast metal thermal conductivity
real r_sm = RP_Get_Real("r_sm"); // Mean peak spacing
real sigma = RP_Get_Real("sigma"); // Mean peak height deviation
real epsilon = RP_Get_Real("epsilon"); // numerical parameter
real p_0 = RP_Get_Real("p_0"); // NTP pressure
real T_1 = RP_Get_Real("t_1"); // impact temperature
real T_0 = RP_Get_Real("t_0"); // NTP temperature

real y; // air gap thickness

real p_1; // water hammer pressure
```

```

real alpha; // helper variable

real lambda; // Effective thermal conductivity

real n; // mean of density of microcontact points

real a; // mean of contact point area

real h; // htc

real dx; // thickness of wall layer

FILE* fp;

Domain *d = Get_Domain(1); // Calculation domain

Thread *t1,*t0;

int zone_id = RP_Get_Real("wall_id"); // wall zone id (defined in
initial_htc.scm)

int shadow_zone_id = RP_Get_Real("shadow_wall_id"); // shadow wall zone id (defined in
initial_htc.scm)

t1 = Lookup_Thread(d,zone_id); // Determine face thread for wall

t0 = Lookup_Thread(d,shadow_zone_id); // Determine face thread for shadow wall

// Calculate wall thickness based on corrected Hamasaiid model

lambda = 2*k_m*k_c/(k_m+k_c);

p_1 = v*wave_speed*rho*sin(impact_angle);

y = pow(2.0,1.0/2.0)/pow(double(PI),1.0/6.0)*pow(double(p_0*T_1/(p_1*T_0)),1.0/3.0)*sigma;

alpha = y/(pow(2,1.0/2.0)*sigma);

n = 8*(1-erf(alpha))/(pow(PI,2)*epsilon*pow(r_sm,2));

```

```

a = 1.0/4.0*r_sm*(2*exp(-pow(double(alpha),2.0))+(pow(double(2*PI),1.0/2.0)*y*(-
1+erf(alpha))/sigma));
h = 2*lambda*a*n/pow(double(1-2*a/r_sm),3.0/2.0);
dx = RP_Get_Real("k_res")/h;
RP_Set_Real("y_0", y);
RP_Set_Real("thickness", dx);

// Print results in file output.txt
fp = fopen("output.txt","a");
fprintf(fp,"flow-time fs q h\n")
fprintf(fp,"%g %g %g %g\n", RP_Get_Real("flow-time"), 0, 0, h);
fclose(fp);
}

```

APPENDIX D

```
;;; SCHEME FILE FOR CALCULATING AND APPLYING HTC EVERY TIME STEP
```

```
;;; AUTHOR: Mikko Karkkainen
```

```
;;; Run DEFINE_ON_DEMAND(evolve_htc) to calculate the value of wall thickness and assign  
it in the variable 'thickness
```

```
(%udf-on-demand 'evolve_htc::libudf)
```

```
;;; Calculate volume average of solid fraction of fluid zone
```

```
(%fill-node-values 'liquid-fraction)
```

```
(rp-var-define 'fl (%volume-integrals 'volume-average '(5) "liquid fraction") 'real #f)
```

```
;;; Run the menu command to apply the initial wall thickness to the thin-wall (needs to be  
performed every time step)
```

```
(ti-menu-load-string (string-append "def bc wall" " " (number->string (%rpgetvar 'wall_id)) " "
```

```
(number->string (%rpgetvar 'thickness)) " ,,,,,,"))
```

APPENDIX E

```
DEFINE_ON_DEMAND(evolve_htc)
{

real PI = RP_Get_Real("pi");
real v = RP_Get_Real("v"); // cast metal impact velocity
real wave_speed = RP_Get_Real("wave_speed"); // sonic wave speed in H13 steel mould
real rho = RP_Get_Real("rho"); // cast metal density
real impact_angle = RP_Get_Real("impact_angle"); // Impact angle in degrees
real k_m = RP_Get_Real("k_m"); // mould thermal conductivity
real k_c = RP_Get_Real("k_c"); // cast metal thermal conductivity
real r_sm = RP_Get_Real("r_sm"); // Mean peak spacing
real sigma = RP_Get_Real("sigma"); // Mean peak height deviation
real epsilon = RP_Get_Real("epsilon"); // numerical parameter
real p_0 = RP_Get_Real("p_0"); // NTP pressure
real T_1 = RP_Get_Real("t_1"); // Melt impact temperature
real T_0 = RP_Get_Real("t_0"); // NTP temperature

real dx; // wall thickness value corresponding thermal resistance
```

```

real temp1;                // mean wall temperature via mean_temp function
real temp2;                // mean shadow wall temperature via mean_temp function
real f_s = 0;             // fraction of solid
FILE *fp;                 // output file variable

real p_1; // water hammer pressure
real alpha; // helper variable
real lambda; // Effective thermal conductivity
real n; // mean of density of microcontact points
real a; // mean of contact point area
real h; // htc

Domain *d = Get_Domain(1); // Calculation domain
int zone_id = RP_Get_Real("wall_id"); // wall zone id
int shadow_zone_id = RP_Get_Real("shadow_wall_id"); // shadow wall zone id
face_t f; // wall face
Thread *t1,*t2; // Wall thread, interior wall cell thread
t1 = Lookup_Thread(d,zone_id); // Determine face thread for wall
t2 = Lookup_Thread(d,shadow_zone_id); // Determine face thread for shadow wall
real q; // heat flux over area
real y = RP_Get_Real("y_0"); // air gap width
real c = RP_Get_Real("c"); // air gap evolution constant

```

```

dx = RP_Get_Real("thickness");
temp2 = mean_wall_temp(t1);
temp1 = mean_wall_temp(t2);
q= (temp1-temp2)/ dx;
f_s = 1-RP_Get_Real("fl"); //get updated fraction of solid
y += c*f_s;    // update air gap width

// Calculate new wall thickness based on updated air gap width using corrected Hamasaiid model
lambda = 2*k_m*k_c/(k_m+k_c);
alpha = y/(pow(2,1.0/2.0)*sigma);
n = 8*(1-erf(alpha))/(pow(PI,2)*epsilon*pow(r_sm,2));
a = 1.0/4.0*r_sm*(2*exp(-pow(double(alpha),2.0))+pow(double(2*PI),1.0/2.0)*y*(-
1+erf(alpha))/sigma));
h = 2*lambda*a*n/pow(double(1-2*a/r_sm),3.0/2.0);
dx = RP_Get_Real("k_res")/h;

RP_Set_Real("thickness", dx);

//write output to output.txt
fp = fopen("output.txt","a");
fprintf(fp,"%g %g %g %g\n", RP_Get_Real("flow-time"), f_s, q, h);
fclose(fp);
}

```

APPENDIX F

```
real mean_wall_temp(Thread* t) // Helper function for calculating mean wall temperature
{
face_t f;

real A[ND_ND], Amag, mean;

real sumt, suma;

sumt = suma = 0.0;

begin_f_loop(f,t)
{
F_AREA(A,f,t);

Amag = NV_MAG(A);

sumt += F_T(f,t) * Amag;

suma += Amag;

}

end_f_loop(f,t);

mean = sumt/suma;

return mean;
```